

National Technical University of Athens
MSc in Analysis and Design of Earthquake Resistant Structures

Study on the effect of FE Simulation on Fragility Analysis of RC Structures

MSc Thesis

Siormpa Vasiliki

Supervisors
Prof. Manolis Papadrakakis
Lect. Nikos Lagaros

National Technical University of Athens
MSc in Analysis and Design of Earthquake Resistant Structures

Study on the effect of FE Simulation on Fragility Analysis of RC Structures

MSc Thesis

Siormpa Vasiliki

Supervisors

Prof. Manolis Papadrakakis

Lect. Nikos Lagaros

Institute of Structural Analysis and Seismic Research

Department of Civil Engineering, NTUA

Athens 2012

Abstract

In the current study two specimens were numerically examined. In the first test case a two-dimensional two story frame structure was simulated with both Beam-Column and non-linear 3D solid FE methods and then subjected into non-linear static pushover analysis. In the second case both of the above simulation methods were used in the non-linear static pushover analysis of a 3-dimensional two-story frame structure.

The aim of the study is to determine the effect of FE simulation methods in fragility analysis and risk assessment.

Contents

Abstract	2
Contents	3
1. Introduction	5
2. Non linear static analysis.....	6
2.1 Performance Based Design	6
2.2 Static pushover methods for seismic design.....	8
2.2.1 The displacement coefficient method (ASCE-41)	8
2.2.2 The capacity spectrum method (ATC-40)	9
2.2.3 The N2 method (EC8).....	9
References	11
3. Simulation – Beam-Column Finite Elements	15
3.1 Introduction.....	15
3.2 Formulation of Beam-Column Element.....	15
3.2.1 Introduction.....	15
3.2.2 Definition of Generalized Forces and Deformations.....	17
3.2.3 Beam-Column Element Formulation.....	19
3.2.4 State Determination	22
3.2.5 Summary of Nonlinear Solution Algorithm.....	31
3.3 Constitutive law for fibre beam-column elements	37
3.3.1 Concrete Stress-Strain Relation	37
3.3.2 Reinforcement Stress-Strain Laws.....	40
References	41
4. Simulation – Three-Dimensional Solid Finite Element Modeling with Embedded Reinforcement	45
4.1 Introduction.....	45
4.2 Formulation.....	47
4.3 Origination/ Termination Point of Reinforcement Segment	47
4.4 Intersection of Reinforcement Segment with Boundaries of Concrete Elements.....	48
4.5 Reinforced Concrete Element Stiffness.....	49
4.6 Constitutive law for 3D solid elements.....	50
4.6.1 Fracture-Plastic Constitutive Model	50
4.6.2 Tension stiffening effect.....	62

4.6.3 Localization Limiters	62
4.6.4 Crack spacing.....	63
4.6.5 Two Models of Smeared Cracks	64
4.7 Reinforcement Stress-Strain Laws	65
4.7.1 Introduction.....	65
4.7.2 Multi-line Law	66
References	66
5.Fragility analysis and Risk assessment.....	68
5.1 Introduction.....	68
5.2 Risk Definition	69
5.3 Risk assessment.....	71
5.4 Calculation of fragility curves	74
5.4.1 Hazus software	74
5.4.2 Calculation method of fragility curves.....	76
5.4.3 Calculation of Damage-State Probability	88
References	90
6.Numerical investigation	93
6.1 Introduction.....	93
6.2 Methodology	93
6.2.1 Definition of the structure.....	93
6.2.2 Simulation	93
6.2.3 Pushover analysis.....	94
6.2.4 Fragility curves.....	94
6.2.5 Risk assessment.....	96
6.3 Fragility analysis results	97
6.3.1 Two-dimensional frame structures.....	97
6.3.2 Three-dimensional frame structures.....	97
6.3.3 Risk analysis results.....	98
7. Conclusions	99

1. Introduction

In the current diploma thesis two types of RC structures are analyzed (two-dimensional and three-dimensional two-story frames) using 3D non-linear FE and column-beam FE simulation in order to determine the effect of both simulation methods on fragility analysis of such structures.

Fragility curves can be used in various ways as part of a seismic vulnerability analysis for many a wide range of types of structures. The fragility analysis methodology consists of the following steps:

- Simulation of the structure
- Non-linear static pushover
- Capacity curves
- Formation of Acceleration Displacement Response Spectrum (ADRS)
- Capacity spectrum method / Estimation of performance point
- Calculation of log-normal cumulative probability density equation
- Formation of fragility curves for four damage limit states

Chapter 2 represents Performance Based Design (PBD) and analyzes Static pushover methods such as the Displacement Coefficient method (ASCE-41), the Capacity Spectrum method (ATC-40) together with the N2 method (EC8).

The 3rd and the 4th Chapters refer to the beam-column and three-dimensional FE simulation methods respectively, describing the formulation of the Finite Elements and the constitutive laws that governs them. The FE methods and stress-strain laws concern both structural concrete and reinforcement.

Chapter 5 introduces Fragility Analysis by analyzing the calculation of fragility curves using the methodology proposed by FEMA/NIBS earthquake loss estimation methodology, commonly known as HAZUS.

Chapter 6 contains the description of the numerical investigation performed. The analysis of two types of structures executed using both FE simulation methods in order to determine their effect on the fragility analysis of RC structures.

Finally, Chapter 7 summarizes the results taken by the analyses.

2. Non linear static analysis

2.1 Performance Based Design

In the past, the requirements and provisions of the seismic design codes for buildings have been based on the experience and they were periodically revised after disastrous earthquakes. Most of the current seismic design codes define a single design earthquake that it is used for assessing the structural performance against earthquake hazard. These codes though have many inherent assumptions built in the design procedure regarding the behaviour of the structure against earthquake loading. Severe damages caused by recent earthquakes made the engineering community to question the effectiveness of the current seismic design codes [1-3]. Given that the primary goal of contemporary seismic design is the protection of human life it is evident that additional performance targets and earthquake intensities should be considered in order to assess the structural performance in many hazard levels. In the last decade the concept of Performance-Based Design (PBD) for structures subjected to seismic loading conditions was introduced [4-6]. In PBD more accurate but time consuming analysis procedures are employed based on nonlinear structural response. The progress that took place in the last two decades in the fields of computational mechanics as well as in hardware technology, made possible to use performance-based seismic design procedures.

Most of the current seismic design codes belong to the category of the prescriptive design procedures (or limit state design procedures), where if a number of checks, expressed in terms of forces, are satisfied the structure is considered safe and that it will not collapse. A typical limit state based design can be viewed as one (i.e. ultimate strength) or two limit state approach (i.e. serviceability and ultimate strength). All modern seismic design procedures are based on the principal that a structure will avoid collapse if it is designed to absorb and dissipate the kinetic energy that is imparted in it during the seismic excitation. Most of the modern seismic codes express the ability of the structure to absorb energy through inelastic deformation using the reduction or behaviour factor q . The capacity of a structure to resist seismic actions in the nonlinear range generally permits their design for seismic loads smaller than those corresponding to a linear elastic response. The seismic loads are reduced using the behaviour factor q . The numerical confirmation of the behavior factor became a subject of research work during the past decade [7,8] in order to check the validity of design theory assumptions and to make structural performance more predictable from engineering point of view.

ATC-40 [4] and FEMA-273 [5] were the first guidelines for Performance-Based seismic rehabilitation of existing buildings while in the report Vision 2000 [6] these ideas were extended to the design process of new buildings. The main objective of this kind of design procedures is to achieve more predictable and reliable levels of safety and operability against natural hazards. According to PBD procedures, the structures should be able to resist earthquakes in a quantifiable manner and to present target performance levels of possible damages. PBD procedures are multi-level design approaches where various levels of structural performance are considered. For example FEMA-356 [9] suggests the following performance levels: operational level, immediate occupancy, life safety and collapse prevention. For assessing the structural performance the guidelines suggest the use of various types of analysis methods: linear static, nonlinear static, linear dynamic and nonlinear dynamic. The most commonly used approach is the nonlinear static analysis also called as pushover analysis method. Pushover analysis allows for the direct evaluation of the performance of the structure at each limit state as opposed to the prescriptive design procedures, such as that of Eurocode 3 [10] where the structure is designed for the ultimate strength limit state.

The European seismic design code (Eurocode 8) [11] and EC3 [10] that are used as a basis for the parametric study performed in this work have the following features: (i) the seismic load is imposed using a 10% in 50 years (475 years return period) elastic response spectrum reduced by a behaviour factor $q=4.0$, (ii) the nominal material strength is reduced by a factor $\gamma_s=1.15$ for steel reinforcement and by a factor $\gamma_c=1.50$ for concrete and (iii) the analysis procedure employed is either the simplified modal or the multi-modal response spectrum analysis.

The majority of the seismic design codes belong to the category of the prescriptive building design codes, which include: site selection and development of conceptual, preliminary and final design stages. According to a prescriptive design code the strength of the structure is evaluated at one limit state between life-safety and near collapse using a response spectrum corresponding to one design earthquake [11]. In addition, serviceability limit state is usually checked in order to ensure that the structure will not deflect or vibrate excessively during its functioning. On the other hand, PBD is a different approach for the seismic design which includes, apart from the site selection and the development of the design stages, the construction and maintenance of the building in order to ensure reliable and predictable seismic performance over its life.

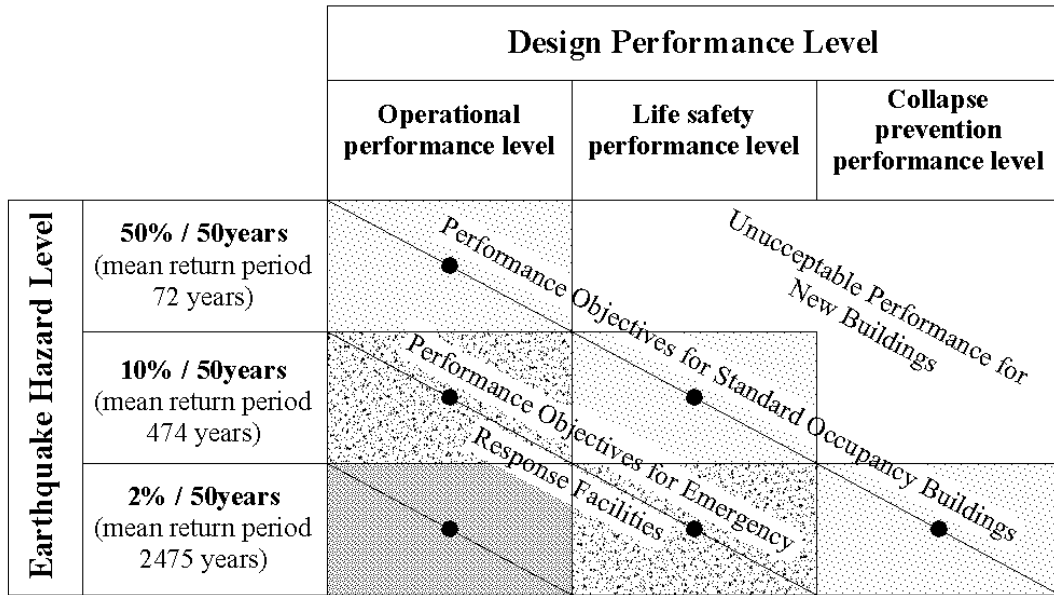


Fig. 2.1 The Design Performances

2.2 Static pushover methods for seismic design

The purpose of the nonlinear static procedure is to assess structural performance in terms of strength and deformation capacity globally as well as at the element level. The structural model is “pushed” according to a predefined lateral load pattern. In order to determine the target displacement in multiple hazard levels required by the performance-based design framework, typically one of the following methods is adopted: the Capacity Spectrum method of ATC-40 (1996), the Coefficient method of ASCE-41 (2006) and the N2 method of EC8 (2004). According to ASCE-41, apart from a first-mode based lateral load pattern the use of a uniform pattern is also suggested. In the numerical results that follow only the first-mode pattern was taken into consideration. For 3D structures the properties of the lateral load pattern have to be extracted from the mode that refers to the direction under consideration.

2.2.1 The displacement coefficient method (ASCE-41)

When pushover analysis, or adopting the ASCE-41 terminology, the nonlinear static procedure (NSP) is implemented, the target displacement, which is the displacement during a given seismic event of a characteristic node on the top of a structure, typically in the roof, is defined with the aid of the formula:

$$d_t = C_0 C_1 C_2 C_3 S_a \frac{T_e^2}{4\pi^2} g \tag{2.1}$$

where C_0 , C_1 , C_2 and C_3 are modification factors, discussed in the FEMA-440 (2005) guidelines and T_e is the effective fundamental period of the building.

2.2.2 The capacity spectrum method (ATC-40)

The Capacity Spectrum Method (CSM) was initially proposed by Freeman (1998). The method compares the capacity of a structure to resist lateral forces to the demand given by a response spectrum. The response spectrum represents the demand while the pushover curve (or the 'capacity curve') represents the available capacity. The steps of the method are briefly summarized as follows: (i) Perform pushover analysis and determine the capacity curve in base shear (V_b) versus roof displacement of the building (D). This diagram is then converted to acceleration-displacement terms (AD) using an equivalent single degree of system (ESDOF). The conversion is performed using the first mode participation factor C_0 ($D^*=D/C_0$) and the modal mass ($A=V_b/M$). (ii) Plot the capacity diagram on the same graph with the 5%-damped elastic response spectrum that is also in AD format. (iii) Select a trial peak deformation demand d_i^* and determine the corresponding pseudo-acceleration A from the capacity diagram, initially assuming $\zeta=5\%$. (iv) Compute ductility $\mu=D^*/u_y$ and calculate the hysteretic damping ζ_h as $\zeta_h=2(\mu-1)/\pi\mu$. The equivalent damping ratio is evaluated from a relationship of the form: $\zeta_{eq}=\zeta_{el}+\kappa\zeta_h$, where κ is a damping modification factor that depends on the hysteretic behavior of the system. Update the estimate of d_i^* using the elastic demand diagram for ζ_{eq} . (v) Check for convergence the displacement d_i^* . When convergence has been achieved the target displacement of the MDOF system is equal to $d_i = C_0 d_i^*$.

2.2.3 The N2 method (EC8)

The N2 method was initially proposed by Fajfar (Fajfar and Fischinger (1988), Fajfar and Gaspersic (1996)) and was later expressed in a displacement-acceleration format (Fajfar (1999)). Recently, the method has been included in the Eurocode 8 (2004). Conceptually the method is a variation of Capacity Spectrum Method that instead of highly damped spectra uses an $R-\mu-T$ relationship. The method, as implemented in EC8, consists of the following steps: (i) Perform pushover analysis and obtain the capacity curve in V_b-D terms, (ii) Convert the pushover curve of the MDOF system to the capacity diagram of an ESDOF system and approximate the capacity curve with an idealized elasto-perfectly plastic relationship to get the period T_e of the ESDOF, (iii) The target displacement is then calculated as:

$$d_{et}^* = S_a(T_e) \left[\frac{T_e}{2\pi} \right]^2 \quad (2.2)$$

where $S_a(T_e)$ is the elastic acceleration response spectrum at the period T_e . To determine the target displacement d_i^* , different expressions are suggested for the short and the medium to long-period ranges:

$T^* < T_c$ (short period range): If $F_y^*/m^* \geq S_a(T_e)$, the response is elastic and thus $d_t^* = d_{et}^*$ and $d_t = C_0 d_t^*$. Otherwise the response is nonlinear and the ESDOF maximum displacement is calculated as:

$$d_t^* = \frac{d_{et}^*}{q_u} \left(1 + (q_u - 1) \frac{T_c}{T_e} \right) \geq d_{et}^* \quad (2.3)$$

where q_u is the ratio between the acceleration in the structure with unlimited elastic behavior $S_e(T^*)$ times the modal mass m^* over its yield force, or simply:

$$q_u = S_a(T_e) m^* / F_y^* .$$

$T^* \geq T_c$ (medium and long period range): The target displacement of the inelastic system is equal to that of an elastic structure, thus $d_t^* = d_{et}^*$. The displacement of the MDOF system is always calculated as $d_t = C_0 d_t^*$.

Table 2.1 Characteristics of the 20 records

Record & Station	R1 (km)	EpiD ² (km)	Duration (sec)	PGA _{long} ³ (g)	PGA _{tran} ⁴ (g)	Soil ⁴	Fault rupt ⁵
Superstition Hills 1987 (B) (M=6.7)							
1. El Centro Imp. Co Cent	18.5	35.83	40.00	0.36	0.26	A	SS
2. Wildlife Liquefaction Array	24.1	29.41	44.00	0.18	0.21	A	SS
Imperial Valley 1979, (M=6.5)							
3. Chihuahua	8.4	18.88	40.00	0.27	0.25	A	SS
4. Compuertas	15.3	24.43	36.00	0.19	0.15	A	SS
5. Plaster City	31.1	54.26	18.75	0.04	0.06	A	SS
6. El Centro Array #12			39.00	0.14	0.12	A	SS
7. El Centro Array #13	18.85	31.99	39.50	0.12	0.14	A	SS
	22.83	35.95					
San Fernando 1971 (M=6.6)							
8. LA, Hollywood Stor. Lot	25.9	39.49	28.00	0.21	0.17	A	RN
Northridge 1994 (M=6.7)							
9. Leona Valley #2	37.2	51.88	32.00	0.09	0.06	A	RN
10. LA, Baldwin Hills	29.9	28.20	40.00	0.24	0.17	C	RN
11. Lake Hughes #1	89.67	93.22	32.00	0.09	0.08	A	RN
12. LA, Hollywood Stor FF	114.62	118.26	40.00	0.23	0.36	A	RN
13. LA, Centinela St.	31.53	32.72	30.00	0.46	0.32	A	RN

Loma Prieta 1989 (M=6.9)							
14. Hollister Diff Array	24.8	45.10	39.64	0.27	0.28	A	RO
15. WAHO	17.5	12.56	24.96	0.37	0.64	C	RO
16. Halls Valley	30.5	36.31	39.95	0.13	0.10	B	RO
17. Agnews State Hospital	24.6	40.12	40.00	0.17	0.16	A	RO
18. Anderson Dam (Downstream)	4.4	16.67	39.61	0.24	0.24	B	RO
19. Coyote Lake Dam (Downstream)	20.8	30.89	39.95	0.16	0.18	B	RO
20. Hollister - South & Pine	27.93	48.24	60.00	0.37	0.18	A	RO

¹Campbell's R Distance

²Distance from the recording site to epicentre

³Long: longitudinal direction

⁴Trans: transverse direction

⁵Campbell's site classification: A (Form Soil), B (Very Firm Soil), C (Soft Rock)

⁶Fault rupture mechanism: SS (Strike Slip), RN (Reverse-Normal), RO (Reverse-Oblique)

References

- [1] Zhai C, Xie L. State-of-art applications of strength reduction factors in seismic design codes, *Earthquake Engineering and Engineering Vibration* 2006; 26(2): 1-7.
- [2] Lagaros ND, Fotis AD, Krikos SA. Assessment of seismic design procedures based on the total cost, *Earthquake Engineering Structural Dynamics* 2006; 35(11): 1381-1401.
- [3] Sullivan, TJ, Calvi, GM, Priestley, MJN, Kowalsky, MJ. *The limitations and performances of different displacement based design methods*, *Journal of Earthquake Engineering*, 2003; 7(1): 201-241.
- [4] Applied Technology Council (ATC), *Methodology for evaluation and upgrade of reinforced concrete buildings*, Report N. ATC-40, California Seismic Safety Commission, Sacramento, California, 1996.
- [5] FEMA 273. *NEHRP Guidelines for seismic rehabilitation of buildings*. Federal Emergency Management Agency, Washington, DC, 1997.
- [6] SEAOC, *Vision 2000 - A framework for performance-based seismic engineering*, Structural Engineers Association of California, Sacramento, California, 1995.
- [7] Fajfar, P. Towards nonlinear methods for the future seismic codes, In *Seismic design practice into the next century*, Booth (Ed.), Balkema, 1998.
- [8] Mazzolani, FM, Piluso, V. *The theory and design of seismic resistant steel frames*, E & FN Spon, 1996.
- [9] FEMA-356: *Prestandard and commentary for the seismic rehabilitation of buildings*. Federal Emergency Management Agency, Washington DC, SAC Joint Venture, 2000.

- [10] FEMA 350: *Recommended Seismic Design Criteria for New Steel Moment-Frame Buildings*. Federal Emergency Management Agency, Washington DC, 2000.
- [11] ENV 1998-1-1. Eurocode 8: Design of Structures for Earthquake Resistance. Part 1: General Rules, Seismic Actions and Rules for Buildings. Commission of the European Communities, European Committee for Standardization, October 2003.
- [12] ENV 1993-1-1. Eurocode 3: Design of steel structures, Part 1-1: General rules; Part 1-5: Strength and stability of planar plated structures without transverse loading. Commission of the European Communities, European Committee for Standardization, December 2003.
- [13] FEMA-National Institute of Building Sciences. HAZUS-MH MR1, *Multi-hazard Loss Estimation Methodology Earthquake Model*, Washington, DC, 2003.
- [14] ASCE/SEI Standard 41-06, 2006. Seismic Rehabilitation of Existing Buildings, prepublication edition, Structural Engineering Institute, American Society of Civil Engineers.
- [15] ATC-13. *Earthquake Damage Evaluation Data for California*. Applied Technology Council: Redwood City, CA, 1985.
- [16] ATC-40, *Seismic evaluation and retrofit of concrete buildings*, Applied Technology Council, Redwood City, 1996.
- [17] Bosco, M., Ghersi, A., Marino, E.M. (2009). On the evaluation of seismic response of structures by nonlinear static methods, *Earthquake Engineering and Structural Dynamics*, 38(13): 1465-1482.
- [18] Cardone, D. (2007). Nonlinear Static Methods vs. Experimental Shaking Table Test Results, *Journal of Earthquake Engineering*, 11 (6): 847-875.
- [19] Chopra, A.K., Goel, R.K. (2000), "Evaluation of NSP to estimate seismic deformation: SDF systems", *Journal of structural engineering New York, N.Y.*, 126(4): 482-490.
- [20] EC0. *Eurocode 0. Basis of Structural Design: Annex A1*. European Committee for Standardisation: Brussels, Belgium, The European Standard EN 1990: 2005.
- [21] EC2. *Eurocode 2. Design of Concrete Structures—Part 1: General Rules and Rules for Buildings*. European Committee for Standardisation: Brussels, Belgium, The European Standard EN 1992-1-1: 2004.
- [22] EC8. *Eurocode 8: Design of Structures for Earthquake Resistance*. European Committee for Standardisation: Brussels, Belgium, The European Standard EN 1998-1: 2004.
- [23] Ellingwood, B.R., Wen, Y.-K. (2005) Risk-benefit-based design decisions for low-probability/high consequence earthquake events in mid-America. *Progress in Structural Engineering and Materials*; 7(2):56-70.
- [24] Fajfar, P. and Fischinger, M. (1988). N2-a method for non-linear seismic analysis of regular buildings, *Proc. 9th World Conf. Earthquake Engng.*, Maruzen, Tokyo (1989), Kyoto, 111-116.
- [25] Fajfar, P. and Gaspersic, P. (1996). The N2 method for the seismic damage analysis for RC buildings, *Earthquake Engng. Struct. Dyn.*, 25: 23-67.
- [26] Fajfar, P., (1999) Capacity spectrum method based on inelastic demand spectra, *Earthquake Engineering & Structural Dynamics*; 28(9): 979-999.

- [27] FEMA 227. A Benefit–Cost Model for the Seismic Rehabilitation of Buildings. Federal Emergency Management Agency, Building Seismic Safety Council: Washington, DC, 1992.
- [28] FEMA 273. NEHRP Guidelines for the Seismic Rehabilitation of Buildings, Building Seismic Safety Council for the Federal Emergency Management Agency, Washington, DC, 1997.
- [29] FEMA-350: Recommended Seismic Design Criteria for New Steel Moment-Frame Buildings. Federal Emergency Management Agency, Washington DC, 2000.
- [30] FEMA-440: *Improvement of Nonlinear Static Seismic Analysis Procedures*. Federal Emergency Management Agency: Washington, DC, 2005.
- [31] Fragiadakis, M., Lagaros, N.D. and Papadrakakis, M. (2006) Performance-based multiobjective optimum design of steel structures considering life-cycle cost, *Structural and Multidisciplinary Optimization*, 32(1).
- [32] Fragiadakis, M., Papadrakakis, M. (2008) Modeling, analysis and reliability of seismically excited structures: Computational issues. *International Journal of Computational Methods*; 5(4): 483-511.
- [33] Freeman, S. A. 1998. Development and use of capacity spectrum method. *Proc.6 US National Conference on Earthquake Engineering*.
- [34] Ghobarah A. On drift limits associated with different damage levels. International Workshop on Performance- Based Seismic Design, June 28 - July 1, 2004.
- [35] Jalayer F. Direct probabilistic seismic analysis: implementing nonlinear dynamic assessments. *Ph.D. Thesis*, Department of Civil and Environmental Engineering, Stanford University, CA, 2003.
- [36] Kang Y-J, Wen YK. Minimum life-cycle cost structural design against natural hazards, Structural Research Series No. 629. Department of Civil and Environmental Engineering, University of Illinois at Urbana-Champaign, Urbana, IL, 2000.
- [37] Kent, D.C., Park, R. (1971). Flexural members with confined concrete. *Journal of Structural Division*; 97(7): 1969-1990.
- [38] Krawinkler, H. and Miranda, E. (2004). Performance-base earthquake engineering, *In: Earthquake Engineering: From Engineering Seismology to Performance-based Earthquake Engineering* (Y. Bozorgnia and Vitelmo V. Bertero(Eds), CRC Press.
- [39] Lagaros, N.D., Papadrakakis, M. (2007) Seismic design of RC structures: a critical assessment in the framework of multi-objective optimization, *Earthquake Engineering and Structural Dynamics*, 36(12): 1623-1639.
- [40] Lagaros, N.D. (2007) Life-cycle cost analysis of construction practices, *Bulletin of Earthquake Engineering*; 5: 425-442.
- [41] Lagaros, N.D., Fragiadakis, M., Papadrakakis, M. (2004). Optimum design of shell structures with stiffening beams. *AIAA Journal*; 42(1): 175-184.
- [42] Lagaros, N.D., Fragiadakis, Evaluation of ASCE-41, ATC-40 and N2 static pushover methods based on optimally designed building structures
- [43] Lin, Y.-Y., Chang, K.-C., Wang, Y.-L. (2004) Comparison of displacement coefficient method and capacity spectrum method with experimental results of RC columns, *Earthquake Engineering and Structural Dynamics*, 33: 35-48.

- [44] McKenna F, Fenves GL. *The OpenSees Command Language Manual* (1.2. edn). PEER, 2001.
- [45] Menegotto, M., Pinto, P.E. (1973) Method of analysis for cyclically loaded reinforced concrete plane frames including changes in geometry and non-elastic behavior of elements under combined normal force and bending. *Proceedings, IABSE Symposium on Resistance and Ultimate Deformability of Structures Acted on by Well Defined Repeated Loads*: 15-22.
- [46] Mitropoulou, Ch.Ch., Lagaros, N.D., Papadrakakis, M. (2010) Economic building design based on energy dissipation: a critical assessment, *Bulletin of Earthquake Engineering*, (to appear).
- [47] Pinho, R., Monteiro, R., Casarotti, C., Delgado, R. (2009) Assessment of Continuous Span bridges through nonlinear static procedures, *Earthquake Spectra*, 25(1): 143-159.
- [48] Rackwitz R. (2006) The effect of discounting, different mortality reduction schemes and predictive cohort life tables on risk acceptability criteria, *Reliability Engineering and System Safety*; 91(4): 469-484.
- [49] Sahely, H.R., Kennedy, C.A., Adams, B.J. (2005) Developing sustainability criteria for urban infrastructure systems. *Canadian Journal of Civil Engineering*; 32(1): 72-85.
- [50] Scott, B.D., Park, R., Priestley, M.J.N. (1982) Stress-strain behavior of concrete confined by overlapping hoops at low and high strain rates. *ACI Journal*; 79: 13-27.
- [51] Vamvatsikos D., Cornell CA. (2002) Incremental dynamic analysis. *Earthquake Engineering and Structural Dynamics*; 31(3): 491-514.
- [52] Wen, Y.K., Kang, Y.J. (2001a) Minimum building life-cycle cost design criteria. I: Methodology. *Journal of Structural Engineering*, 127(3): 330-337.
- [53] Wen, Y.K., Kang, Y.J. (2001b) Minimum building life-cycle cost design criteria. II: Applications. *Journal of Structural Engineering*, 127(3): 338-346.

3. Simulation – Beam-Column Finite Elements

3.1 Introduction

In beam-column FE simulation each member is modelled with a single force-based, fibre beam-column element. This element provides a good balance between accuracy and computational cost. The modified Kent-Park model, where the monotonic envelope of concrete in compression follows the model of Kent and Park (1971) as extended by Scott *et al.* (1982), is employed for the simulation of the concrete fibres. This model was chosen because it allows for an accurate prediction of the demand for flexure-dominated RC members despite its relatively simple formulation. The transient behaviour of the reinforcing bars was simulated with the Menegotto-Pinto model (1973), while the effects of shear and bond-slip are neglected. The effect of gravity loads and second-order effects are considered using the complete geometric stiffness matrix.

3.2 Formulation of Beam-Column Element

3.2.1 Introduction

This paragraph the general formulation of a beam-column finite element based on the flexibility method is presented. The presentation is cast in the more general form of a mixed method for two reasons: (i) this approach illustrates better the state-determination process used in the nonlinear analysis algorithm, and, (ii) it yields in a direct way the flexibility dependent deformation shape functions of the element that reduce the general mixed method formulation to the flexibility method used in this study. In addition, the generality of the mixed method allows the exploration of alternative deformation shape functions in future studies.

In order to consider the inelastic behaviour either the plastic-hinge or the fibre approach can be adopted. Given that the plastic hinge approach has limitations in terms of accuracy fibre beam-column elements are preferable (Fragiadakis and Papadrakakis, 2008). According to the fibre approach each structural element is discretized into a number of integration sections, and each section is divided into a number of fibres (Fig. 3.1) with specific material properties (A_{fib} , E_{fib}), which are restrained to beam kinematics. Each fibre in the section can be assigned concrete, structural steel, or reinforcing bar material properties. The sections are located either at the centre of the structural element or at its Gaussian integration points.

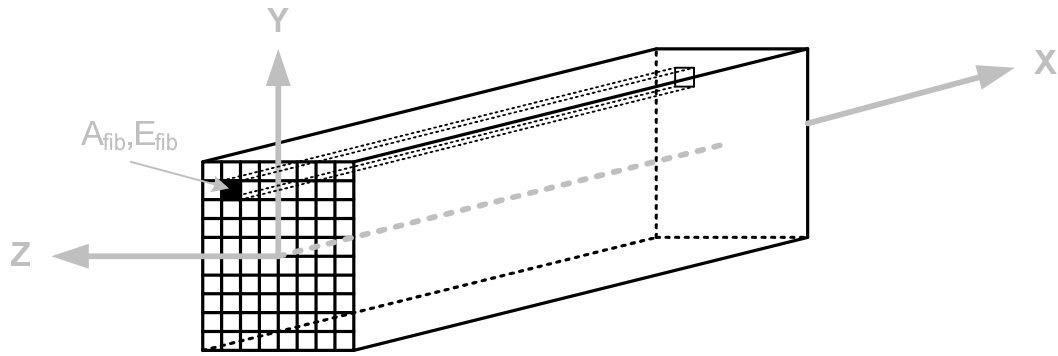


Fig. 3.1 Modelling of the inelastic behaviour-the fibre approach

The main advantage of the fibre approach is that every fibre has a simple uniaxial material model allowing an easy and efficient implementation of the inelastic behaviour. This approach is considered to be suitable for inelastic beam-column elements under dynamic loading and provides a reliable solution compared to other formulations. However, it results to higher computational demands in terms of memory storage and CPU time. When a displacement-based formulation is adopted the discretization should be adaptive with a dense mesh at the joints and a single elastic element for the remaining part of the member. On the other hand, force-based fibre elements allow modelling a member with a single beam-column element. Therefore, in this work each structural member is modelled with a single force-based, fibre beam-column element.

In keeping with the generality of the presentation the force-deformation relation is not specialized at the section level. This is deferred to the following chapter where the section force-deformation relation is derived from a fiber discretization of the cross section. A different approach which uses the theory of classical plasticity to derive a hysteretic model of the section force-deformation relation is presented by Spacone et al. (1992).

The proposed beam-column element is based on the assumption that deformations are small and that plane sections remain plane during the loading history. The formulation of the element is based on the mixed method: the description of the force distribution within the element by interpolation functions that satisfy equilibrium is the starting point of the formulation. Based on the concepts of the mixed method it is shown that the selection of flexibility dependent shape functions for the deformation field of the element results in considerable simplification of the final equations. With this particular selection of deformation shape functions the general mixed method reduces to the special case of the flexibility method. The mixed

method formalism is, nonetheless, very useful in understanding the proposed procedure for the element state determination.

The proposed formulation offers several advantages over previous models:

- Equilibrium and compatibility are always satisfied along the element: equilibrium is satisfied by the selection of force interpolation functions and compatibility is satisfied by integrating the section deformations to obtain the corresponding element deformations and end displacements. An iterative solution is then used to satisfy the nonlinear section force-deformation relation within the specified tolerance.
- The softening response of reinforced concrete members, which are either poorly reinforced or are subjected to high axial forces, can be described without computational difficulties.

3.2.2 Definition of Generalized Forces and Deformations

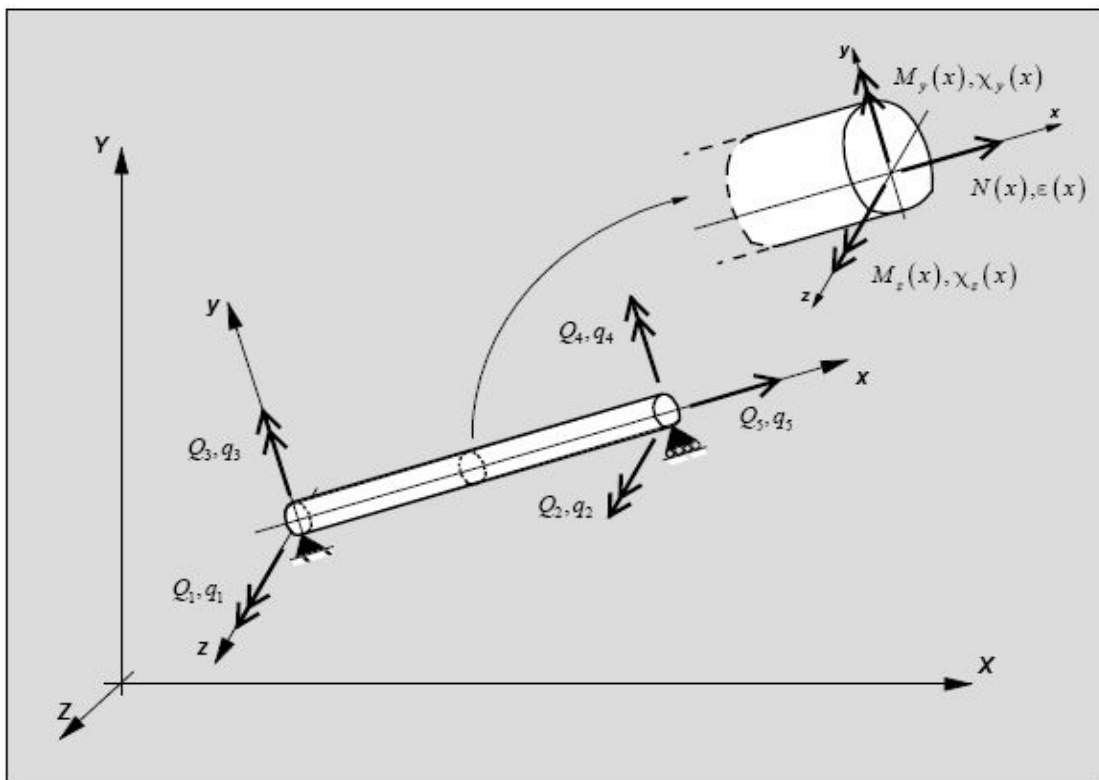


Fig. 3.2 Generalized forces and deformations at the element and section level.

The beam-column finite element is schematically shown in Fig. 3.2. The reference frame for the element is the local coordinate system x, y, z , while X, Y, Z denotes the global reference system. The longitudinal axis x is the union of geometric centroids of each section.

The following convention is followed for the notation of forces, displacements and deformations: forces are represented by uppercase letters and corresponding deformations or displacements are denoted by the same letter in lowercase. Normal letters denote scalar quantities, while boldface letters denote vectors and matrices.

Fig. 3.2 shows the element forces with the corresponding deformations. Rigid body modes are not included in Fig. 3.2. Since the present formulation is based on linear geometry, rigid body modes can be incorporated with a simple geometric transformation. The element has 5 degrees of freedom: one axial extension, q_5 , and two rotations relative to the chord at each end node, (q_1, q_3) and (q_2, q_4) , respectively. For the sake of clarity these are called element generalized deformations or simply element deformations in the following discussion. Q_1 through Q_5 indicate the corresponding generalized forces: one axial force, Q_5 , and two bending moments at each end node Q_1, Q_3 and Q_2, Q_4 , respectively. The end rotations and corresponding moments refer to two arbitrary, orthogonal axes \mathbf{y} and \mathbf{z} . The element generalized forces and deformations are grouped in the following vectors:

$$\text{Element force vector: } \mathbf{Q} = \begin{Bmatrix} Q_1 \\ Q_2 \\ Q_3 \\ Q_4 \\ Q_5 \end{Bmatrix} \quad (3.1)$$

$$\text{Element deformation vector: } \mathbf{q} = \begin{Bmatrix} q_1 \\ q_2 \\ q_3 \\ q_4 \\ q_5 \end{Bmatrix} \quad (3.2)$$

Fig. 3.2 also shows the generalized forces and deformations at a section of the element. Section deformations are represented by three strain resultants: the axial strain $\epsilon(x)$ along the longitudinal axis and two curvatures $x_z(x)$ and $x_y(x)$ about two arbitrary, orthogonal axes \mathbf{z} and \mathbf{y} , respectively. The corresponding force resultants are the axial force $N(x)$ and two bending moments $M_z(x)$ and $M_y(x)$. The section generalized forces and deformations are grouped in the following vectors:

$$\text{Section force vector: } \mathbf{D}(x) = \begin{Bmatrix} M_z(x) \\ M_y(x) \\ N(x) \end{Bmatrix} = \begin{Bmatrix} D_1(x) \\ D_2(x) \\ D_3(x) \end{Bmatrix} \quad (3.3)$$

$$\text{Section deformation vector: } \mathbf{D}(x) = \begin{Bmatrix} x_z(x) \\ x_y(x) \\ \varepsilon(x) \end{Bmatrix} = \begin{Bmatrix} d_1(x) \\ d_2(x) \\ d_3(x) \end{Bmatrix} \quad (3.4)$$

The element formulation can be readily extended to include the torsional degrees of freedom, as long as these are uncoupled from the present degrees of freedom and are governed by linear elastic behavior. The focus of the present study is the element in Fig. 3.2, which describes the nonlinear behavior of frame members under arbitrary cyclic load histories of biaxial bending and axial load.

3.2.3 Beam-Column Element Formulation

In the following the mixed finite element method is used to formulate the beam-column element. At this stage no reference is made to specific interpolation functions. It is shown, however, that, if flexibility dependent deformation shape functions are selected, then the mixed method simplifies to the flexibility method. The nonlinear section force-deformation relation is also kept general.

The derivation follows the two-field mixed method which uses the integral form of equilibrium and section force-deformation relations to derive the matrix relation between element generalized forces and corresponding deformations. In order to arrive at a linear relation, the section force-deformation relation is linearized about the present state. An iterative algorithm is, then, used to satisfy the nonlinear section force-deformation relation within the required tolerance.

In the two-field mixed method (Zienkiewicz and Taylor 1989) independent shape functions are used for approximating the force and deformation fields along the element. Denoting with Δ increments of the corresponding quantities, the two fields are written

$$\Delta \mathbf{d}^i(x) = \mathbf{a}(x) \Delta \mathbf{q}^i \quad (3.5)$$

$$\mathbf{D}^i(x) = \mathbf{b}(x) \mathbf{Q}^i \quad \text{and} \quad \Delta \mathbf{D}^i(x) = \mathbf{a}(x) \Delta \mathbf{Q}^i \quad (3.6)$$

where matrices $\mathbf{a}(x)$ and $\mathbf{b}(x)$ are the deformation and force interpolation matrices, respectively. Superscript i indicates the i -th iteration of the Newton-Raphson (N-R) iteration loop, which is performed at the structure degrees of freedom until equilibrium between applied loads and internal resisting forces is satisfied (Zienkiewicz and Taylor 1989). The use of the superscript in the element formulation becomes necessary because of the special form of the deformation interpolation functions, which are flexibility dependent.

In the mixed method formulation the integral forms of equilibrium and section force deformation relations are expressed first. These are then combined to obtain the relation between element force and deformation increments.

The weighted integral form of the linearized section force-deformation relation is

$$\int_0^L \delta \mathbf{D}^T(x) \cdot [\Delta \mathbf{d}^i(x) - \mathbf{f}^{i-1}(x) \cdot \Delta \mathbf{D}^i(x)] dx = 0 \quad (3.7)$$

The section force-deformation relation appears in the flexibility form

$$\Delta \mathbf{d}^i(x) = \mathbf{f}^{i-1}(x) \cdot \Delta \mathbf{D}^i(x) \quad (3.8)$$

so that the resulting element flexibility matrix is symmetric, as discussed by Zienkiewicz and Taylor (1989). The superscript $i-1$ indicates that at the i -th Newton-Raphson iteration the section flexibility at the end of the previous iteration is used. Substituting Eqs. (3.5) and (3.6) in Eq. (3.7) results in

$$\delta \mathbf{Q}^T \int_0^L \mathbf{b}^T(x) \cdot [\mathbf{a}(x) \Delta \mathbf{q}^i(x) - \mathbf{f}^{i-1}(x) \cdot \mathbf{b}(x) \Delta \mathbf{Q}^i] dx = 0 \quad (3.9)$$

Since Eq. (3.9) must hold for any $\delta \mathbf{Q}^T$, it follows that

$$\left[\int_0^L \mathbf{b}^T(x) \cdot \mathbf{a}(x) \cdot dx \right] \Delta \mathbf{q}^i - \left[\int_0^L \mathbf{b}^T(x) \cdot \mathbf{f}^{i-1}(x) \cdot \mathbf{b}(x) \cdot dx \right] \cdot \Delta \mathbf{Q}^i = 0 \quad (3.10)$$

The expressions in square brackets represent the following matrices:

$$\mathbf{F}^{i-1} = \left[\int_0^L \mathbf{b}^T(x) \cdot \mathbf{f}^{i-1}(x) \cdot \mathbf{b}(x) \cdot dx \right] \quad (3.11)$$

$$\mathbf{T} = \left[\int_0^L \mathbf{b}^T(x) \cdot \mathbf{a}(x) \cdot dx \right] \quad (3.12)$$

where \mathbf{F} is the element flexibility matrix and \mathbf{T} is a matrix that only depends on the interpolation function matrices. Using Eqs. (3.11) and (3.12) Eq. (3.10) can be written in the form

$$\mathbf{T} \Delta \mathbf{q}^i - \mathbf{F}^{i-1} \cdot \Delta \mathbf{Q}^i = 0 \quad (3.13)$$

or equivalently

$$\mathbf{T} \Delta \mathbf{q}^i = \mathbf{F}^{i-1} \cdot \Delta \mathbf{Q}^i \quad (3.14)$$

This is the matrix expression of the integral form of the linearized section force-deformation relation.

In the next step the equilibrium of the beam element is satisfied. In the classical two-field mixed method the integral form of the equilibrium equation is derived from the virtual displacement principle

$$\int_0^L \delta \mathbf{d}^T(x) \cdot [\mathbf{D}^{i-1}(x) + \Delta \mathbf{D}^i(x)] dx = \delta \mathbf{q}^T \cdot \mathbf{P}^i \quad (3.15)$$

where \mathbf{P}^i is the vector of applied loads that are in equilibrium with the internal forces $\mathbf{D}^{i-1}(x) + \Delta \mathbf{D}^i(x)$. Eqs. (3.5) and (3.6) are substituted in Eq. (3.15) to yield

$$\delta \mathbf{q}^T \int_0^L \mathbf{a}^T(x) \cdot [\mathbf{b}(x) \mathbf{Q}^{i-1} + \mathbf{b}(x) \Delta \mathbf{Q}^i] dx = \delta \mathbf{q}^T \cdot \mathbf{P}^i \quad (3.16)$$

Observing that Eq. (3.16) must hold for arbitrary $\delta \mathbf{q}^T$, it follows that

$$\left[\int_0^L \mathbf{b}^T(x) \cdot \mathbf{a}(x) \cdot dx \right] \cdot \mathbf{Q}^{i-1} + \left[\int_0^L \mathbf{b}^T(x) \cdot \mathbf{a}(x) \cdot dx \right] \cdot \Delta \mathbf{Q}^i = \mathbf{P}^i \quad (3.17)$$

If the notation introduced in Eq. (3.12) is used, Eq. (3.17) can be written in matrix form

$$\mathbf{T}^T \cdot \mathbf{Q}^{i-1} + \mathbf{T}^T \cdot \Delta \mathbf{Q}^i = \mathbf{P}^i \quad (3.18)$$

This is the matrix expression of the integral form of the element equilibrium equations. The rearrangement and combination of Eqs. (3.13) and (3.18) results in

$$\begin{bmatrix} -\mathbf{F}^{i-1} & \mathbf{T} \\ \mathbf{T}^T & \mathbf{0} \end{bmatrix} \cdot \begin{Bmatrix} \Delta \mathbf{Q}^i \\ \Delta \mathbf{q}^i \end{Bmatrix} = \begin{Bmatrix} \mathbf{0} \\ \mathbf{P}^i - \mathbf{T}^T \cdot \mathbf{Q}^{i-1} \end{Bmatrix} \quad (3.19)$$

If the first equation in Eq. (3.19) is solved for $\Delta \mathbf{Q}^i$ and the result is substituted in the second equation, the following expression results

$$\mathbf{T}^T \cdot [\mathbf{F}^{i-1}]^{-1} \cdot \mathbf{T} \cdot \Delta \mathbf{q}^i = \mathbf{P}^i - \mathbf{T}^T \cdot \mathbf{Q}^{i-1} \quad (3.20)$$

So far, the specific selection of force and deformation interpolation functions $\mathbf{b}(x)$ and $\mathbf{a}(x)$, respectively, has not been addressed. In keeping with the generality of the formulation the selection of the force interpolation functions $\mathbf{b}(x)$ is deferred to the following chapter. Even

though in a mixed finite element method the deformation interpolation functions $\mathbf{a}(x)$, are completely independent of $\mathbf{b}(x)$, Eq. (3.12) reveals that a special choice of the deformation shape functions $\mathbf{a}(x)$, results in considerable simplification. With this simplification in mind $\mathbf{a}(x)$, are selected as flexibility dependent shape functions according to the following expression

$$\mathbf{a}(x) = \mathbf{f}^{i-1}(x) \cdot \mathbf{b}(x) \cdot [\mathbf{F}^{i-1}]^{-1} \quad (3.21)$$

These interpolation functions, thus, relate the section deformations with the corresponding element deformations according to

$$\Delta \mathbf{d}^i(x) = \mathbf{f}^{i-1}(x) \cdot \mathbf{b}(x) \cdot [\mathbf{F}^{i-1}]^{-1} \cdot \Delta \mathbf{q}^i \quad (3.22)$$

\mathbf{F}^{i-1} is the tangent element flexibility matrix at the end of the previous Newton-Raphson iteration. This special selection of the deformation shape functions reduces matrix \mathbf{T} in Eq. (3.12) to a 3x3 identity matrix \mathbf{I} . This can be readily proven by substituting Eq. (3.21) in Eq. (3.12):

$$\mathbf{T} = \left[\int_0^L \mathbf{b}^T(x) \cdot \mathbf{a}(x) \cdot dx \right] = \left[\int_0^L \mathbf{b}^T(x) \cdot \mathbf{f}^{i-1}(x) \cdot \mathbf{b}(x) \cdot dx \right] \cdot [\mathbf{F}^{i-1}]^{-1} = \mathbf{I} \quad (3.23)$$

With this choice of the deformation shape functions $\mathbf{a}(x)$ Eq. (3.20) becomes

$$[\mathbf{F}^{i-1}]^{-1} \cdot \Delta \mathbf{q}^i = \mathbf{P} - \mathbf{Q}^{i-1} \quad (3.24)$$

At the same time this choice of functions $\mathbf{a}(x)$ reduces the general mixed method to the flexibility method. The final matrix equation, Eq. (3.24), expresses the linearized relation between the applied unbalanced forces $\mathbf{P} - \mathbf{Q}^{i-1}$ and the corresponding deformation increments $\Delta \mathbf{q}^i$ at the element level. The element stiffness matrix is written in the form $[\mathbf{F}]^{-1}$ to indicate that it is obtained by inverting the element flexibility matrix. The linear equation system in Eq. (3.24) is different from that obtained by the classical stiffness method in two respects: (a) the element stiffness matrix is obtained by inverting the element flexibility matrix, as in the flexibility method, and, (b) the state determination phase of the nonlinear analysis is different, as will be described in detail in the following section.

Even though the classical flexibility method yields the same system of linearized equations in Eq. (3.24), the above derivation was based on the two-field mixed method for the following reasons: (a) the mixed method formulation yields directly the expression for the flexibility dependent deformation shape functions $\mathbf{a}(x)$ in Eq. (3.21), (b) it reveals the consistent implementation of the state determination process, and, (c) it is more general in scope allowing alternative deformation shape functions to be explored in future studies.

Since $\mathbf{a}(x)$ is not independent of $\mathbf{b}(x)$ and changes during the iterative solution process, as is apparent from Eq. (3.21), the proposed method corresponds to the classical flexibility method. Moreover, this procedure reduces to the stiffness method for the case that the section constitutive relation is perfectly linear. In other words, the independence between the two fields is not intrinsic in the definition of the shape functions, but derives from the material nonlinearity of the section force-deformation relation.

3.2.4 State Determination

Most studies to date concerned with the analysis of reinforced concrete frame structures are based on finite element models that are derived with the stiffness method. Recent studies have focused on the advantages of flexibility based models (Zeris and Mahin 1988), but have failed to give a clear and consistent method of calculating the resisting forces from the given element deformations. This problem arises when the formulation of a finite element is based on the application of the virtual force principle. While the element is flexibility-dependent, the computer

program into which it is inserted is based on the direct stiffness method of analysis. In this case the solution of the global equilibrium equations yields the displacements of the structural degrees of freedom. During the phase of state determination the resisting forces of all elements in the structure need to be determined. Since in a flexibility based element there are no deformation shape functions to relate the deformation field inside the element to the end displacements (or element deformations) this process is not straightforward and is not well developed in flexibility based models proposed to date. This fact has led to some confusion in the numerical implementation of previous models. The description of the consistent state determination process in this study benefits from the derivation of the governing equations by the two-field mixed method.

In a nonlinear structural analysis program each load step corresponds to the application of an external load increment to the structure. The corresponding structural displacement increments are determined and the element deformations are extracted for each element. The process of finding the resisting forces that correspond to the given element deformations is known as state determination. The state determination process is made up of two nested phases: a) *the element state determination*, when the element resisting forces are determined for the given end deformations, and b) *the structure state determination*, when the element resisting forces are assembled to the structure resisting force vector. The resisting forces are then compared with the total applied loads and the difference, if any, yields the unbalanced forces which are then applied to the structure in an iterative solution process until external loads and internal resisting forces agree within a specified tolerance.

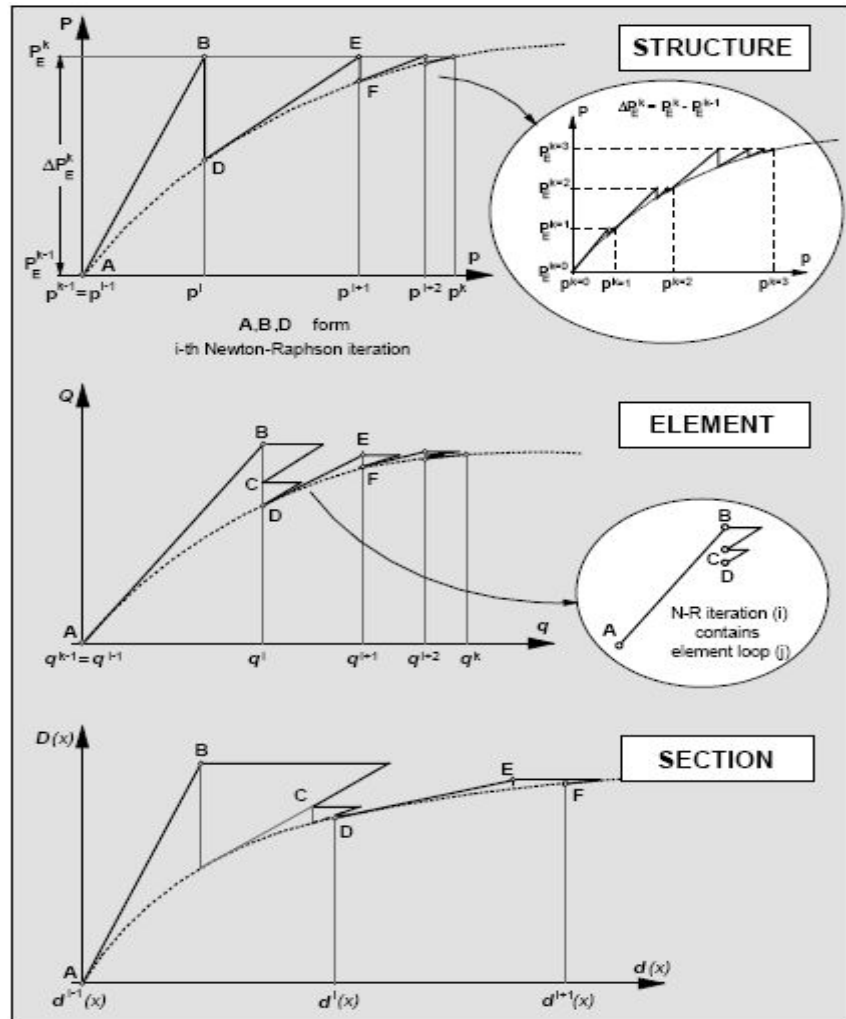


Fig. 3.3 Schematic illustration of state determination at the structure, element and section level: k denotes the load step, i the structure Newton-Raphson iteration and j the iteration for the element state determination.

In the present study the nonlinear algorithm consists of three distinct nested processes, which are illustrated in Fig. 3.3. The two outermost processes denoted by indices k and i involve structural degrees of freedom and correspond to classical nonlinear analysis procedures. The innermost process denoted by index j is applied within each element and corresponds to the element state determination. Fig. 3.3 shows the evolution of the structure, element and section states during one load increment ΔP_E^k that requires several Newton-Raphson iterations i .

In summary, the superscripts of the nested iterations are defined as follows:

k : denotes the applied load step. The external load is imposed in a sequence of load increments P_E^k . At load step k the total external load is equal to $P_E^k = P_E^{k-1} + \Delta P_E^k$ with $k=1, \dots, nstep$ and $P_E^0=0$;

i : denotes the Newton-Raphson iteration scheme at the structure level, i.e. the structure state determination process. This iteration loop yields the structural displacements \mathbf{p}^k that correspond to applied loads \mathbf{P}_E^k ;

j : denotes the iteration scheme at the element level, i.e. the element state determination process. This iteration loop is necessary for the determination of the element resisting forces that correspond to element deformations \mathbf{q}^i during the i -th Newton-Raphson iteration.

The processes denoted by indices k and i are common in nonlinear analysis programs and will not be discussed further. The iteration process denoted by the index j , on the other hand, is special to the beam-column element formulation developed in this study and will be described in detail. It should be pointed out that any suitable nonlinear solution algorithm can be used for the iteration process denoted by index i . In this study the Newton-Raphson method is used. The selection of this method for iteration loop i does not affect the strategy for iteration loop j , which has as its goal the determination of the element resisting forces for the given element deformations.

In a finite element that is based on the stiffness method of analysis the section deformations are obtained directly from the element end deformations by deformation interpolation functions. The corresponding section resisting forces are determined subsequently from the section force-deformation relation. The weighted integral of the *section resisting forces* over the element length yields the *element resisting forces* and completes the process of element state determination.

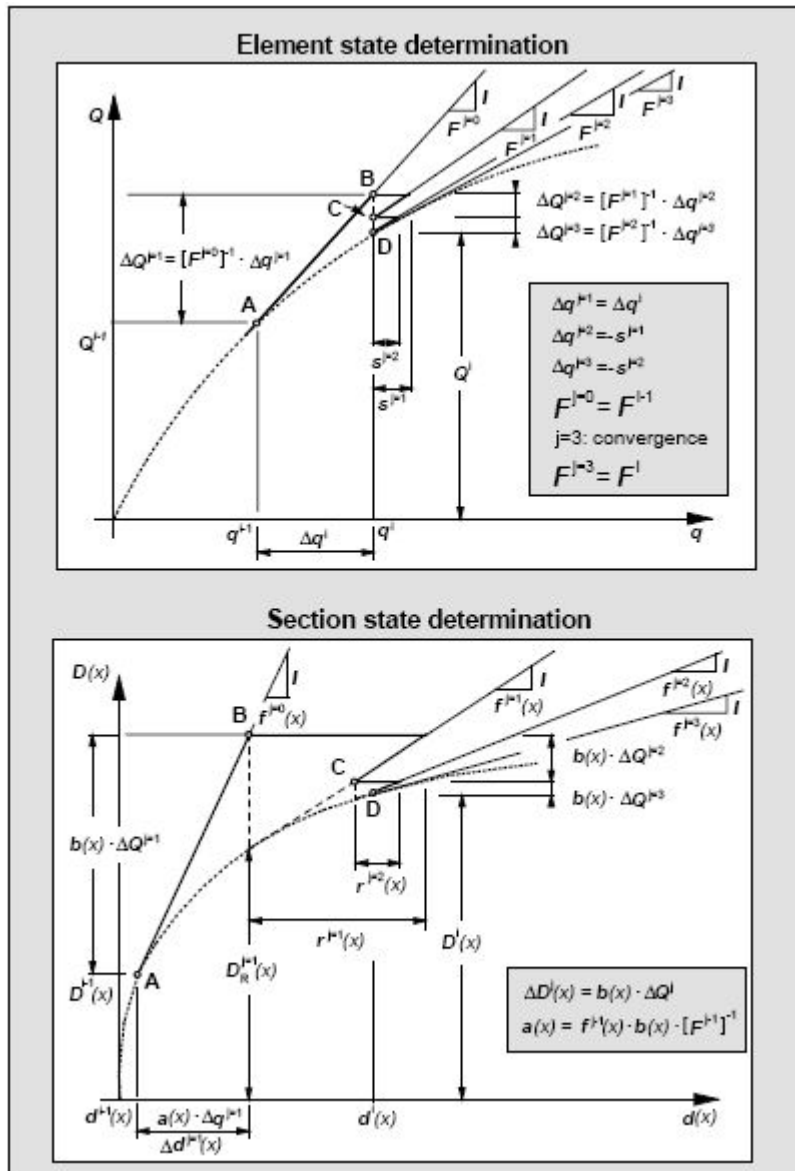


Fig. 3.4 Element and section state determination for flexibility-based element: computation of element resisting forces Q^i corresponding to the element deformations q^i .

In a flexibility-based finite element the first step is the determination of the element forces from the current element deformations using the stiffness matrix at the end of the last iteration. The force interpolation functions yield the forces along the element. The first problem is, then, the determination of the section deformations from the given section forces, since the nonlinear section force-deformation relation is commonly expressed as an explicit function of section deformations. The second problem arises from the fact that changes in the section stiffness produce a new element stiffness matrix which, in turn, changes the element forces for the given deformations.

These problems are solved in the present study by a special nonlinear solution method. In this method residual element deformations are determined at each iteration. Deformation compatibility at the structural level requires that these residual deformations be corrected. This is accomplished at the element level by applying corrective element forces based on the current stiffness matrix. The corresponding section forces are determined from the force interpolation functions so that equilibrium is always satisfied along the element. These section forces cannot change during the section state determination in order to maintain equilibrium along the element. Consequently, the linear approximation of the section force-deformation relation about the present state results in residual section deformations. These are then integrated along the element to obtain new residual element deformations and the whole process is repeated until convergence occurs. It is important to stress that *compatibility of element deformations and equilibrium along the element are always satisfied in this process.*

The nonlinear solution procedure for the element state determination is schematically illustrated in Fig. 3.4 for one Newton-Raphson iteration i . In Fig. 3.4 convergence in loop j is reached in three iterations. The consistent notation between Figs. 3.3 and 3.4 highlights the relation between the corresponding states of the structure, the element and the section, which are denoted by uppercase Roman letters.

At the i -th Newton-Raphson iteration it is necessary to determine the element resisting forces for the current element deformations

$$\mathbf{q}^i = \mathbf{q}^{i-1} + \Delta \mathbf{q}^i \quad (3.25)$$

To this end an iterative process denoted by index j is introduced inside the i -th Newton-Raphson iteration. The first iteration corresponds to $j=1$. The initial state of the element, represented by point **A** and $j=0$ in Fig. 3.4, corresponds to the state at the end of the last iteration of loop j for the $(i-1)$ Newton-Raphson iteration. With the initial element tangent stiffness matrix

$$[\mathbf{F}^{j=0}]^{-1} = [\mathbf{F}^{i-1}]^{-1}$$

and the given element deformation increments

$$\Delta \mathbf{q}^{j=1} = \Delta \mathbf{q}^i$$

the corresponding element force increments are:

$$\Delta \mathbf{Q}^{j=1} = [\mathbf{F}^{j=0}]^{-1} \cdot \Delta \mathbf{q}^{j=1}$$

The section force increments can now be determined from the force interpolation functions:

$$\Delta \mathbf{D}^{j=1}(x) = \mathbf{b}(x) \cdot \Delta \mathbf{Q}^{j=1}$$

With the section flexibility matrix at the end of the previous Newton-Raphson iteration

$$\mathbf{f}^{j=0}(x) = \mathbf{f}^{i-1}(x)$$

the linearization of the section force-deformation relation yields the section deformation increments $\Delta \mathbf{d}^{j=1}(x)$:

$$\Delta \mathbf{d}^{j=1}(x) = \mathbf{f}^{j=0}(x) \cdot \Delta \mathbf{D}^{j=1}(x)$$

The section deformations are updated to the state that corresponds to point **B** in Fig. 3.4:

$$\mathbf{d}^{j=1}(x) = \mathbf{d}^{j=0}(x) + \Delta \mathbf{d}^{j=1}(x)$$

According to the section force-deformation relation, which is here assumed to be explicitly known for simplicity's sake, section deformations $\mathbf{d}^{j=1}(x)$ correspond to resisting forces $\mathbf{D}_R^{j=1}(x)$ and a new tangent flexibility matrix $\mathbf{f}^{j=1}(x)$ (Fig. 3.4). In a finite element based on the stiffness method the section resisting forces $\mathbf{D}_R^{j=1}(x)$ would be directly transformed to element resisting forces $\mathbf{Q}^{j=1}$ thus violating the equilibrium along the element in a strict sense. Since this is undesirable, a new nonlinear solution method is proposed in this study. In this approach the section unbalanced forces are first determined

$$\mathbf{D}_U^{j=1}(x) = \Delta \mathbf{D}^{j=1}(x) - \mathbf{D}_R^{j=1}(x)$$

and are then transformed to residual section deformations $\mathbf{r}^{j=1}(x)$

$$\mathbf{r}^{j=1}(x) = \mathbf{f}^{j=1}(x) \cdot \mathbf{D}_U^{j=1}(x)$$

The residual section deformations are thus the linear approximation to the deformation error made in the linearization of the section force-deformation relation (Fig. 3.4). While any suitable flexibility matrix can be used in calculating the residual deformations, the tangent flexibility matrix used in this study offers the fastest convergence rate.

The residual section deformations are integrated along the element based on the virtual force principle to obtain the residual element deformations:

$$\mathbf{s}^{j=1} = \int_0^L \mathbf{b}^T(x) \cdot \mathbf{r}^{j=1}(x) \cdot dx$$

At this point the first iteration $j=1$ of the corresponding iteration loop is complete. The final element and section states for $j=1$ correspond to point **B** in Fig. 3.4. The residual

section deformations $\mathbf{r}^{j=1}(x)$ and the residual element deformations $\mathbf{s}^{j=1}$ are determined in the first iteration, but the corresponding deformation vectors are not updated. Instead, they are the starting point of the remaining steps within iteration loop j . The presence of residual element deformations $\mathbf{s}^{j=1}$ violates compatibility, since elements sharing a common node would now have different end displacements. In order to restore the inter-element compatibility corrective forces equal to $-\mathbf{[F}^{j=1}]^{-1} \cdot \mathbf{s}^{j=1}$ must be applied at the ends of the element, where $\mathbf{F}^{j=1}$ is the updated element tangent flexibility matrix determined by integration of the section flexibility matrices according to Eq. (3.11). A corresponding force increment

$-\mathbf{b}(x) \cdot \mathbf{[F}^{j=1}]^{-1} \cdot \mathbf{s}^{j=1}$ is applied at all control sections inducing a deformation increment $-\mathbf{f}^{j=1}(x) \cdot \mathbf{b}(x) \cdot \mathbf{[F}^{j=1}]^{-1} \cdot \mathbf{s}^{j=1}$. Thus, in the second iteration $j=2$ the state of the element and of the sections within the element change as follows: the element forces are updated to the value

$$\mathbf{Q}^{j=2} = \mathbf{Q}^{j=1} + \Delta \mathbf{Q}^{j=2}$$

$$\text{where } \Delta \mathbf{Q}^{j=2} = -\mathbf{[F}^{j=1}]^{-1} \cdot \mathbf{s}^{j=1}$$

and the section forces and deformations are updated to the values

$$\mathbf{D}^{j=2}(x) = \mathbf{D}^{j=1}(x) + \Delta \mathbf{D}^{j=2}(x)$$

$$\text{and } \mathbf{d}^{j=2}(x) = \mathbf{d}^{j=1}(x) + \Delta \mathbf{d}^{j=2}(x)$$

$$\text{where } \Delta \mathbf{D}^{j=2}(x) = -\mathbf{b}(x) \cdot \mathbf{[F}^{j=1}]^{-1} \cdot \mathbf{s}^{j=1}$$

$$\Delta \mathbf{d}^{j=2}(x) = \mathbf{r}^{j=1}(x) - \mathbf{f}^{j=1}(x) \cdot \mathbf{b}(x) \cdot \mathbf{[F}^{j=1}]^{-1} \cdot \mathbf{s}^{j=1}$$

The state of the element and the sections within the element at the end of the second iteration $j=2$ corresponds to point **C** in Fig. 3.4. The new tangent flexibility matrices $\mathbf{f}^{j=2}(x)$ and the new residual section deformations

$$\mathbf{r}^{j=2}(x) = \mathbf{f}^{j=2}(x) \cdot \mathbf{D}_U^{j=2}(x)$$

are computed for all sections. The residual section deformations are then integrated to obtain the residual element deformations $\mathbf{s}^{j=2}$ and the new element tangent flexibility matrix $\mathbf{F}^{j=2}$ is determined by integration of the section flexibility matrices $\mathbf{f}^{j=2}(x)$ according to Eq. (3.11). This completes the second iteration within loop j .

The third and subsequent iterations follow exactly the same scheme. Convergence is achieved when the selected convergence criterion is satisfied. With the conclusion of iteration loop j the element resisting forces for the given deformations \mathbf{q}^i are established, as represented by point **D** in Figs. 3.3 and 3.4. The Newton-Raphson iteration process can now proceed with step $i+1$.

It is important to point out that during iteration loop j the element deformations \mathbf{q}^i do not change except in the first iteration $j=1$, when increments $\Delta\mathbf{q}^{j=1} = \Delta\mathbf{q}^i$ are added to the element deformations \mathbf{q}^{i-1} at the end of the previous Newton-Raphson iteration. These deformation increments result from the application of corrective loads $\Delta\mathbf{P}_E^i$ at the structural degrees of freedom during the Newton-Raphson iteration process. For $j>1$ only the element forces change until the nonlinear solution procedure converges to the element resisting forces \mathbf{Q}^i which correspond to element deformations \mathbf{q}^i . This is illustrated at the top of Fig. 3.4 where points **B**, **C** and **D**, which represent the state of the element at the end of subsequent iterations in loop j , lie on the same vertical line, while the corresponding points at the control sections of the element do not, as shown in the bottom of Fig. 3.4. This feature of the proposed nonlinear solution procedure ensures displacement compatibility at the element ends.

The proposed nonlinear analysis method offers several advantages. Equilibrium along the element is always strictly satisfied, since section forces are derived from element forces by the force interpolation functions according to Eq. (3.6). Compatibility is also satisfied, not only at the element ends, but also along the element. In fact, in the expression for the section deformation corrections

$$\Delta\mathbf{d}^j(x) = \mathbf{r}^{j-1}(x) - \mathbf{f}^{j-1}(x) \cdot \mathbf{b}(x) \cdot [\mathbf{F}^{j-1}]^{-1} \cdot \mathbf{s}^{j-1}$$

the second term satisfies Eqs. (3.21) and (3.22), which express the relation between section and element deformations by means of shape functions $\mathbf{a}(x)$. The residual section deformations $\mathbf{r}^{j-1}(x)$, however, do not strictly satisfy this compatibility condition. It is possible to satisfy this requirement by integrating the residual deformations $\mathbf{r}^{j-1}(x)$ to obtain \mathbf{s}^{j-1} and then using the deformation shape functions $\mathbf{a}(x)$ to calculate the section deformation increments as $\mathbf{a}(x) \cdot \mathbf{s}^{j-1}$. Since this is, however, rather inefficient from a computational standpoint, the small compatibility error in the calculation of residual section deformations $\mathbf{r}^{j-1}(x)$ is neglected in this study.

While equilibrium and compatibility are satisfied along the element during each iteration of loop j , the section force-deformation relation and, consequently, the element force-deformation relation is only satisfied within a specified tolerance when convergence is achieved at point **D** in Fig. 3.4. In other words, during subsequent iterations the element forces approach the value that corresponds to the imposed element deformations, while maintaining equilibrium and compatibility along the element at all times. This approximation of the force-deformation relation in the proposed nonlinear analysis method is preferable to the approximation of either the equilibrium or the compatibility conditions of the element, particularly when

considering the uncertainty in the definition of constitutive relations for reinforced concrete structures.

3.2.5 Summary of Nonlinear Solution Algorithm

After the description of the element state determination process in the previous section a step-by-step summary of the computations is presented below. The summary focuses on a single iteration i at the structural degrees of freedom, because the innovative aspect of the present study is the process of element state determination. The rest of the nonlinear solution algorithm follows well established methods, such as the Newton-Raphson method selected in this study. Alternative solution strategies can be implemented without additional effort, since these are independent of the element state determination. The relation of the Newton-Raphson iteration to the nonlinear solution of the entire structure is illustrated at the top of Fig. 3.3, which also shows the relation between the overall solution strategy and the element state determination process with corresponding states denoted by uppercase Roman letters. Fig. 3.4 shows in detail the evolution of the state determination process for an element and corresponds to steps **(4)** through **(13)** in the following summary. The flow chart of computations for the entire solution algorithm is shown in Fig. 3.5, while the flow chart of computations for the element state determination is shown in Fig. 3.6.

The i -th Newton-Raphson iteration is organized as follows:

(1) Solve the global system of equations and update the structural displacements. At the i -th Newton-Raphson iteration the structure stiffness matrix \mathbf{K}_s^{i-1} at the end of the previous iteration $i-1$ is used to compute the displacement increments $\Delta \mathbf{p}^i$ for the given load increments $\Delta \mathbf{P}_E^i$ which represent the unbalanced forces from the previous iteration.

$$\mathbf{K}_s^{i-1} \cdot \Delta \mathbf{p}^i = \Delta \mathbf{P}_E^i \quad (3.26)$$

$$\mathbf{p}^i = \mathbf{p}^{i-1} + \Delta \mathbf{p}^i \quad (3.27)$$

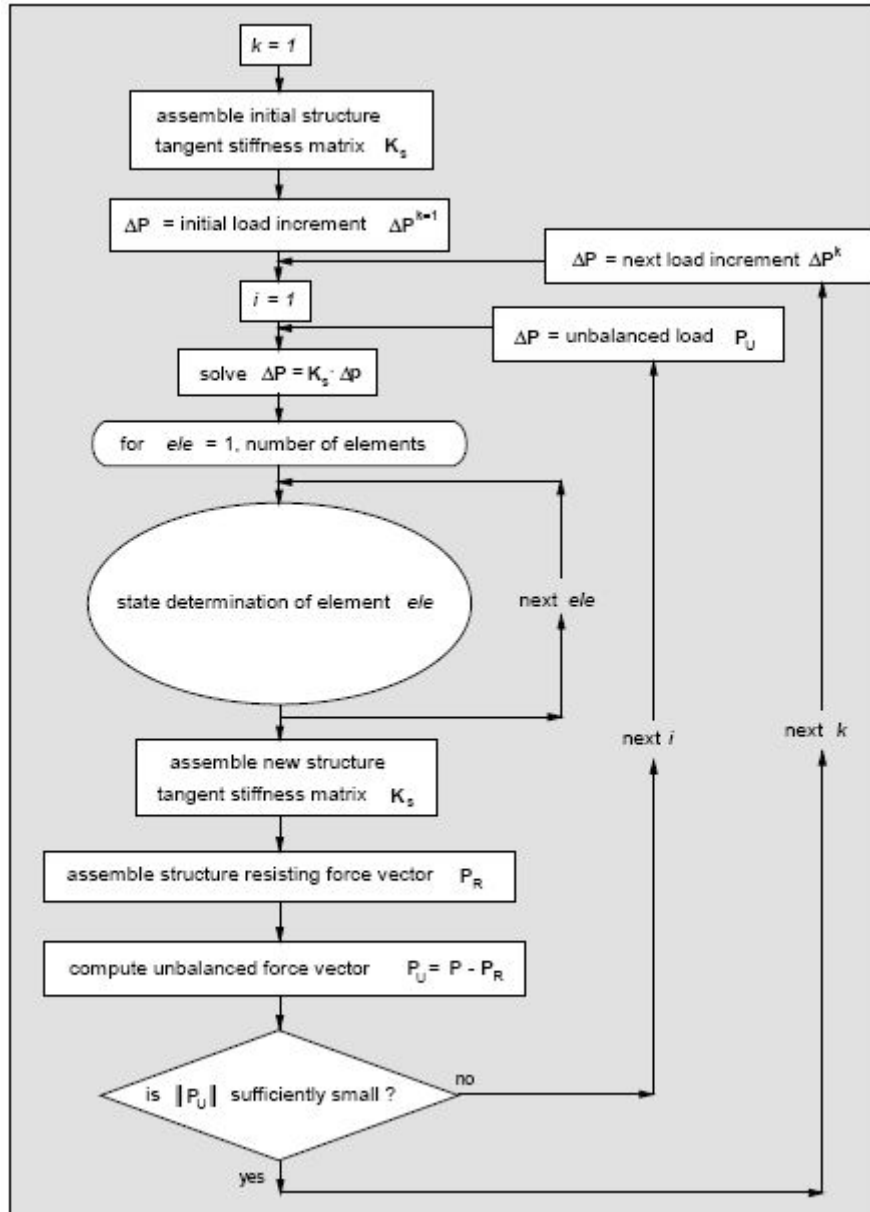


Fig. 3.5 Flow chart of structure state determination.

(2) Calculate the element deformation increments and update the element deformations. Using matrix L_{ele} , which relates structural displacements with element deformations, the element deformation increments Δq^i are determined:

$$\Delta q^i = L_{ele} \cdot \Delta p^i \quad (3.28)$$

$$q^i = q^{i-1} + \Delta q^i \quad (3.29)$$

Note that matrix L_{ele} is the combination of two transformations: in the first transformation the element displacements in the global reference system \mathbf{p} are transformed to the displacements $\bar{\mathbf{q}}$ in the element local reference system. In the

second transformation the element displacements $\bar{\mathbf{q}}$ are transformed to element deformations \mathbf{q} by elimination of the rigid-body modes.

As discussed in Section 2.2.4, the new element deformations \mathbf{q}^i do not change until the following $(i+1)$ Newton-Raphson iteration. The remaining operations of the nonlinear solution algorithm make up the element state determination process which establishes the element resisting forces for the given element deformations \mathbf{q}^i .

(3) *Start the element state determination. Loop over all elements in the structure. The state determination of each element is performed in loop j . The index of the first iteration is $j=1$.*

(4) *Determine the element force increments. The element force increments $\Delta\mathbf{Q}^j$ are determined with the element stiffness matrix \mathbf{K}^{j-1} at the end of the previous iteration in loop j*

$$\Delta\mathbf{Q}^j = \mathbf{K}^{j-1} \cdot \Delta\mathbf{q}^j \quad (3.30)$$

When $j=1$, $\mathbf{K}^0 = \mathbf{K}^{i-1}$ and $\Delta\mathbf{q}^1 = \Delta\mathbf{q}^i$ where $i-1$ corresponds to the state of the element at the end of the last Newton-Raphson iteration. When $j>1$ $\Delta\mathbf{q}^j$ is equal to the residual element deformations of the previous iteration, as determined in Step (13).

(5) *Update the element forces.*

$$\mathbf{Q}^j = \mathbf{Q}^{j-1} + \Delta\mathbf{Q}^j \quad (3.31)$$

When $j=1$, $\mathbf{Q}^0 = \mathbf{Q}^{i-1}$ where $i-1$ corresponds to the state at the end of the last Newton-Raphson iteration.

(6) *Determine the section force increments. Steps (6) through (11) are performed for all control sections (integration points) of the element.*

The section force increments $\Delta\mathbf{D}^j(x)$ are determined from the force interpolation functions $\mathbf{b}(x)$. Subsequently, the section forces $\mathbf{D}(x)$ are updated.

$$\Delta\mathbf{D}^j(x) = \mathbf{b}(x) \cdot \Delta\mathbf{Q}^j \quad (3.32)$$

$$\mathbf{D}^j(x) = \mathbf{D}^{j-1}(x) + \Delta\mathbf{D}^j(x) \quad (3.33)$$

(7) *Determine the section deformation increments.*

The section deformation increments $\Delta\mathbf{d}^j(x)$ are determined by adding the residual section deformations from the previous iteration $\mathbf{r}^{j-1}(x)$ to the deformation increments caused by the section force increments $\Delta\mathbf{D}^j(x)$. The latter are determined with the section flexibility matrix $\mathbf{f}^{j-1}(x)$ at the end of the previous iteration in loop j .

$$\Delta\mathbf{d}^j(x) = \mathbf{r}^{j-1}(x) + \mathbf{f}^{j-1}(x)\Delta\mathbf{D}^j(x) \quad (3.34)$$

$$\mathbf{d}^j(x) = \mathbf{d}^{j-1}(x) + \Delta \mathbf{d}^j(x) \quad (3.35)$$

when $j=1$, $\mathbf{r}^0(x) = 0$

(8) Determine the tangent stiffness and flexibility matrices of the section.

Assuming for simplicity that the section force-deformation relation is known explicitly, the tangent stiffness matrix $\mathbf{k}^j(x)$ is updated for the new section deformations $\mathbf{d}^j(x)$.

This stiffness matrix $\mathbf{k}^j(x)$ is then inverted to obtain the new tangent flexibility matrix $\mathbf{f}^j(x)$ of the section.

$$\mathbf{f}^j(x) = [\mathbf{k}^j(x)]^{-1} \quad (3.36)$$

(9) Determine the section resisting forces.

The resisting forces $\mathbf{D}_R^j(x)$ are determined for the current deformations $\mathbf{d}^j(x)$ from the section force-deformation relation.

(10) Determine the unbalanced forces at the section.

The section unbalanced forces $\mathbf{D}_U^j(x)$ are the difference between the applied forces $\mathbf{D}^j(x)$ and the resisting forces $\mathbf{D}_R^j(x)$.

$$\mathbf{D}_U^j(x) = \mathbf{D}^j(x) - \mathbf{D}_R^j(x) \quad (3.37)$$

(11) Determine the residual section deformations.

The section unbalanced forces and the new section flexibility yield the residual section deformations $\mathbf{r}^j(x)$

$$\mathbf{r}^j(x) = \mathbf{f}^j(x) \mathbf{D}_U^j(x) \quad (3.38)$$

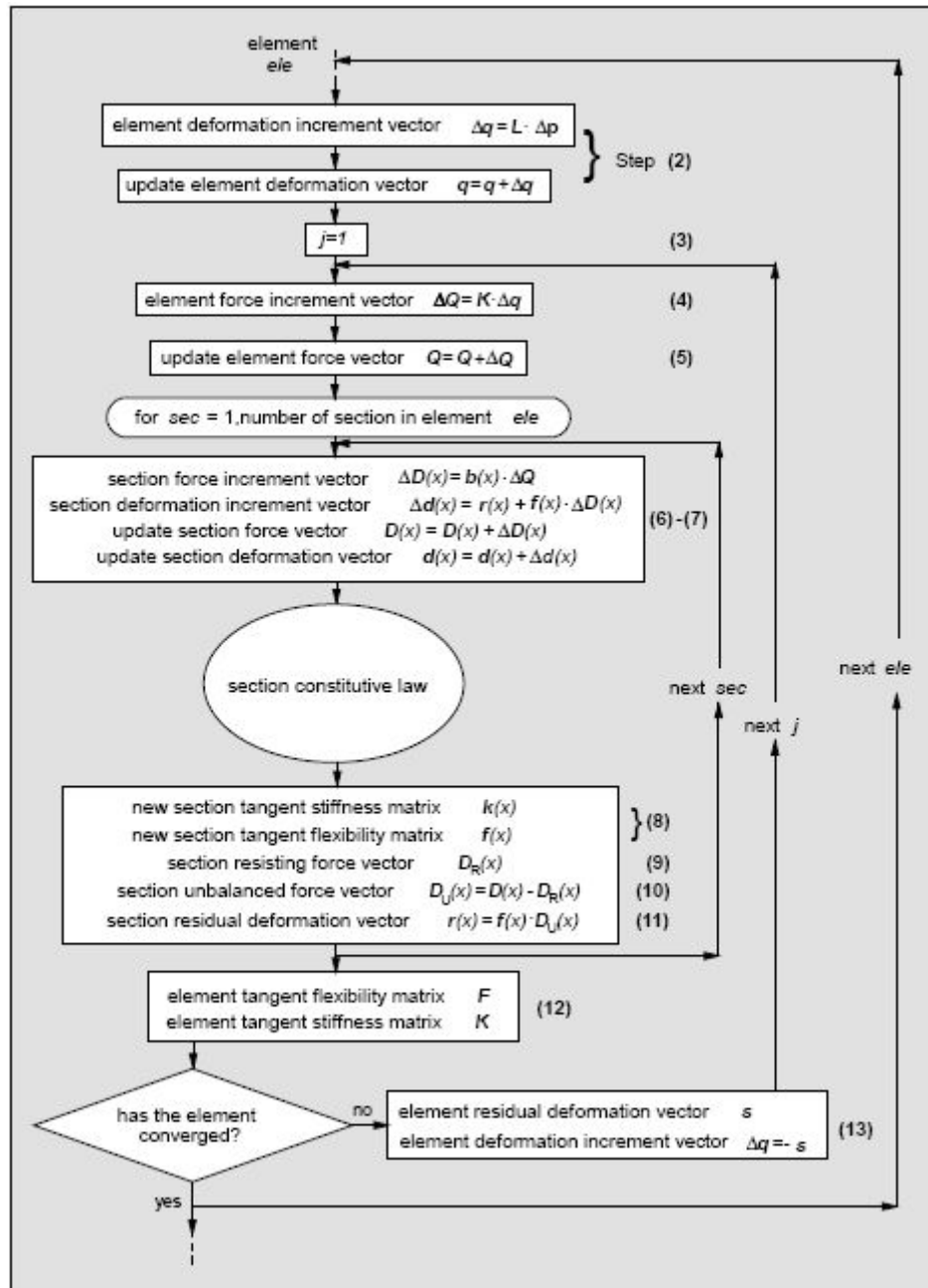


Fig. 3.6 Flow chart of structure state determination: the section.

(12) Determine the element flexibility and stiffness matrices.

The element flexibility matrix F^j is formed by integration of the section flexibility matrices $f^j(x)$. This matrix is then inverted to obtain the element tangent stiffness matrix K^j .

$$F^j = \left[\int_0^L \mathbf{b}^T(x) \cdot \mathbf{f}^j(x) \cdot \mathbf{b}(x) \cdot dx \right] \quad (3.39)$$

$$K^j = [F^j]^{-1} \quad (3.40)$$

(13) Check for element convergence.

a) If the unbalanced forces at all element sections are sufficiently small, the element is considered to have converged. After setting $\mathbf{Q}^i = \mathbf{Q}^j$ and $\mathbf{K}^i = \mathbf{K}^j$ the process continues with step **(14)**.

b) If some sections have not converged, the residual element deformations \mathbf{s}^j are determined by integration of the residual section deformations $\mathbf{r}^j(x)$.

$$\mathbf{s}^j = \left[\int_0^L \mathbf{b}^T(x) \cdot \mathbf{r}^j(x) \cdot dx \right] \quad (3.41)$$

At this point j is incremented to $j+1$ and a new iteration begins in loop j . In this case

$\Delta \mathbf{q}^j$ in Eq. (3.30) is replaced with $\Delta \mathbf{q}^{j+1}$ which is set equal to $-\mathbf{s}^j$

$$\Delta \mathbf{q}^{j+1} = -\mathbf{s}^j \quad (3.42)$$

and steps **(4)** through **(13)** are repeated until convergence is achieved at all sections of the element.

(14) Determine the resisting forces and the new stiffness matrix of the entire structure.

When all elements have converged, the i -th step of the Newton-Raphson iteration is complete. The element force vectors are assembled to form the updated structure resisting forces

$$\mathbf{P}_R^i = \sum_{ele=1}^n \mathbf{L}_{ele}^T \cdot (\mathbf{Q}^i)_{ele} \quad (3.43)$$

where n is the total number of beam-column elements in the structure and the subscript ele is added as a summation index. The new structure stiffness matrix is formed by assembling the current element stiffness matrices

$$\mathbf{K}_S^i = \sum_{ele=1}^n \mathbf{L}_{ele}^T \cdot (\mathbf{K}^i)_{ele} \cdot \mathbf{L}_{ele} \quad (3.44)$$

At this point the structure resisting forces \mathbf{P}_R^i are compared with the total applied loads. If the difference \mathbf{P}_U^i , which is the structure unbalanced force vector, is not within the specified tolerance, i is incremented to $i+1$ and the next Newton-Raphson iteration begins. Steps **(1)** through **(14)** are repeated after replacing $\Delta \mathbf{P}_E^i$ with $\Delta \mathbf{P}_E^{i+1} = \Delta \mathbf{P}_U^i$ until convergence takes place at the structure degrees of freedom.

A graphical overview of the entire nonlinear analysis procedure is presented in Figs. 3.5 and 3.6. Fig. 3.5 provides an overview of the entire process with the nesting of the individual iteration loops and does not differ from conventional nonlinear analysis schemes. The new features of the algorithm are introduced in the element state determination phase, which is singled out for presentation in Fig. 3.6. Since all integrations along the element in Eqs. (3.39) and (3.41) need to be performed

numerically, an additional iteration loop over all control sections of the element is introduced in this diagram.

3.3 Constitutive law for fibre beam-column elements

In the numerical test examples, all analyses have been performed using the OpenSEES (McKenna and Fenves, 2001) platform. A bilinear material model with pure kinematic hardening is adopted for the steel fibres, while geometric nonlinearity is explicitly taken into consideration. For the simulation of the concrete fibres the modified Kent-Park model, where the monotonic envelope of concrete in compression follows the model of Kent and Park (1971) as extended by Scott et al. (1982), is employed for the simulation of the concrete fibres. This model was chosen because it allows for an accurate prediction of the demand for flexure-dominated RC members despite its relatively simple formulation. The transient behaviour of the reinforcing bars was simulated with the Menegotto-Pinto model 1973, while the effects of shear and bond-slip are neglected. The effect of gravity loads and second-order effects are considered using the geometric stiffness matrix.

3.3.1 Concrete Stress-Strain Relation

In order to compute the concrete stress in each layer, a material law describing the concrete stress-strain relation under arbitrary cyclic strain histories is needed. There is some uncertainty as to the influence of the concrete model on the overall behaviour of RC members subjected to bending and small values of axial force. Some investigators have concluded that a crude concrete model suffices to accurately predict experimental results. This might be true in the case of monotonic loading and cyclic loading that is restricted to small excitations. It is not true, however, in the case of severe cyclic loading. The results of the study by Scott et al. (1982) indicated that the strength deterioration of RC members under large cyclic excitations depends largely on the capacity of confined concrete to sustain stresses in the strain range beyond the maximum strength. This requires the use of a refined concrete model.

The monotonic envelope curve of concrete in compression follows the model of Kent and Park (1971) that was later extended by Scott et al. (1982). Even though more accurate and complete models have been published, the modified Kent and Park model offers a good balance between simplicity and accuracy. In the modified Kent and Park model the monotonic concrete stress-strain relation in compression is described by three regions:

$$\sigma_c = Kf'_c \left[\frac{2\varepsilon_c}{\varepsilon_0} - \left(\frac{\varepsilon_c}{\varepsilon_0} \right)^2 \right] \text{ for } \varepsilon_c \leq \varepsilon_0 \quad (3.45a)$$

$$\sigma_c = Kf'_c [1 - Z(\epsilon_c - \epsilon_0)] \geq 0.2Kf'_c \text{ for } \epsilon_0 \leq \epsilon_c \leq \epsilon_u \quad (3.45b)$$

$$\sigma_c = 0.2Kf'_c \text{ for } \epsilon_c \geq \epsilon_u \quad (3.45c)$$

where $\epsilon_0 = 0.002K$ while

$$K = 1 + \frac{\rho_s f_{yh}}{f'_c}$$

and

$$Z = \frac{0.5}{\frac{3 + 0.29f'_c}{145f'_c - 1000} + 0.75\rho_s \sqrt{\frac{h'}{s_h}} - 0.002K} \quad (3.46)$$

where ϵ_0 is the concrete strain at maximum stress, K is a factor which accounts for the strength increase due to confinement, Z is the strain softening slope, f'_c is the concrete compressive cylinder strength in MPa, f_{yh} is the yield strength of stirrups in MPa, ρ_s is the ratio of the volume of hoop reinforcement to the volume of concrete core measured to outside of stirrups, h' is the width of concrete core measured to outside of stirrups, and s_h is the center to center spacing of stirrups or hoop sets.

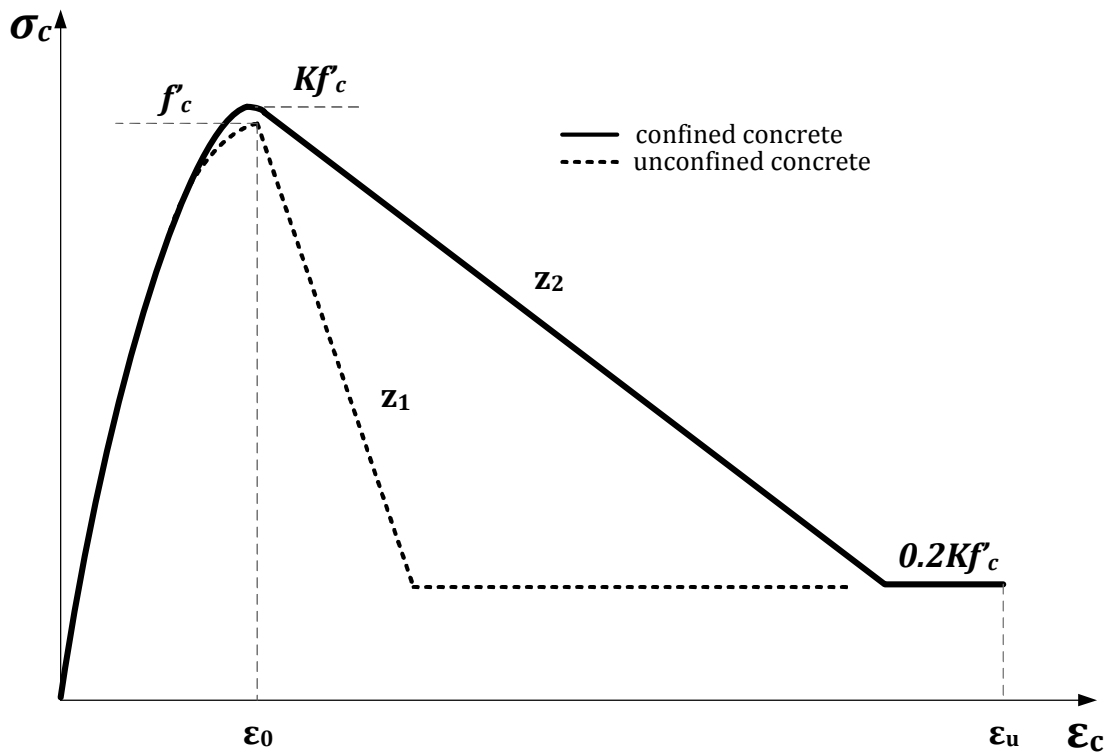


Fig. 3.7 Modified Kent-Park model, stress-strain relation for confined and unconfined concrete

In the case of *concrete confined by stirrup-ties*, Scott et al. (1982) suggest that ϵ_u is determined from the following expression:

$$\varepsilon_u = 0.004 + 0.9\rho_s \frac{f_{yh}}{300} \quad (3.47)$$

To account for crushing of the concrete cover the strength in the cover layer is reduced to $0.2f'_c$ once the compressive strain exceeds the value of ε_u , which in this study is set equal to 0.005. The following rules govern the hysteretic behaviour of the concrete stress-strain relation (Fig. 3.7):

1. Unloading from a point on the envelope curve takes place along a straight line connecting the point ε_r at which unloading starts to a point ε_p on the strain axis given by the expressions

$$\varepsilon_u = 0.145 \left(\frac{\varepsilon_r}{\varepsilon_0} \right)^2 + 0.13 \left(\frac{\varepsilon_r}{\varepsilon_0} \right), \text{ for } \frac{\varepsilon_r}{\varepsilon_0} < 2.0 \quad (3.48a)$$

$$\varepsilon_u = 0.707 \left(\frac{\varepsilon_r}{\varepsilon_0} - 2.0 \right) + 0.834, \text{ for } \frac{\varepsilon_r}{\varepsilon_0} \geq 2.0 \quad (3.48b)$$

where ε_0 is the strain level corresponding to the maximum stress in compression.

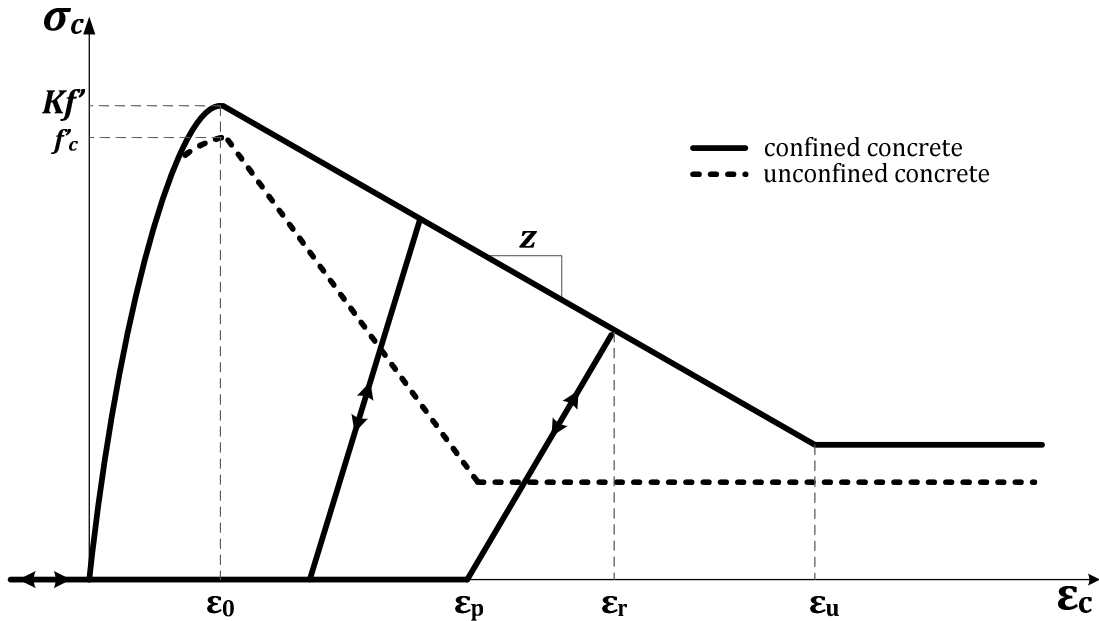


Fig. 3.8 Hysteretic concrete stress-strain relation

The first part of the expression (Eq. (3.48a)) was proposed by Karsan and Jirsa (1969) and relates the normalized strain on the envelope with the strains at the completion of unloading through a quadratic formula. Eq. (3.48b) was added

to the model since Eq. (3.48a) exhibits unreasonable behaviour under high compressive strain conditions.

2. The concrete stress is equal to zero for strains smaller than the strain at complete unloading since the tensile resistance is neglected.
3. On reloading in compression the stress is zero as long as the strain is smaller than the strain at complete unloading. Once the concrete strain becomes larger than that value, reloading continues along the previous unloading path (Fig. 3.8).

3.3.2 Reinforcement Stress-Strain Laws

The steel reinforcement was modelled using a bilinear constitutive law. In a bilinear material model (Fig. 3.9) the elastic behaviour of the material is determined by the Hooke law, having the initial modulus of elasticity equal to E and yield point, determined by the yield stress σ_y . The behaviour of the material after the yield point is determined by a second inclined line whose slope is determined by the tangent modulus of elasticity E_T . The tangent modulus of elasticity E_T is determined by means of the initial modulus of elasticity through the hardening coefficient b by the relationship:

$$E_T = b \cdot E \quad (3.49)$$

For a perfectly plastic material the hardening coefficient b is equal to zero. Apart from the coefficient b , the hardening parameter H is often used, which connects the stress σ with the plastic strain ϵ_{pl} through the relation:

$$\sigma = H \cdot \epsilon_{pl} \quad (3.50)$$

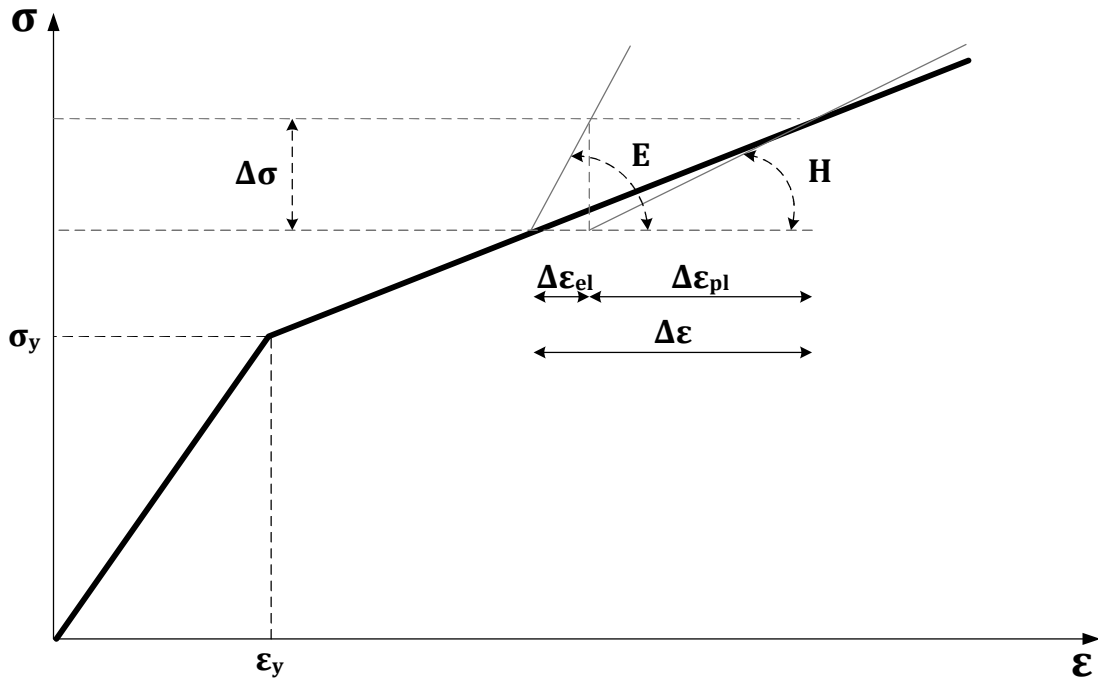


Fig. 3.9 The multi-linear stress-strain law for reinforcement

The hardening parameter H , the tangent modulus of elasticity E_T and the hardening coefficient b are related through the following expression:

$$H = \frac{E_T}{1 - b}$$

or

$$E_T = E \cdot \left(1 - \frac{E}{E - H} \right)$$

(3.51)

In the case of steel structures, where the yield strength in tension exceeds the yield stress in compression, the yield strength at the next load loop will be different. This phenomenon is known as the Bauschinger. The Bauschinger effect refers to a material property, where the characteristics of stress - strain of the material changed as a result of microscopic stress distribution in the material.

References

- [1] Abdel-Halim, M.A.H., Abu-Lebdeh. T.M., Analytical Study for Concrete Confinement in Tied Columns, J. Structural Engineering Div., ASCE, No.11, 115(1989) 2810-2828.
- [2] ASCE Task Committee on Finite Element Analysis of Reinforced Concrete Structures. (1982). State-of-the-Art Report on Finite Element Analysis of Reinforced Concrete, ASCE Special Publications.

- [3] Balakrishnan S. Murray D.W. (1988), Concrete Constitutive model for NLFE analysis of structures, J. Structural Engineering Div., ASCE, 114(7) 1449-1466.
- [4] Bazant, Z.P, Oh, B.H (1983) Crack Band Theory for Fracture of Concrete, Materials and Structures, RILEM, Vol. 16, 155-177.
- [5] Bhatt, P., M.S. Barj, G.F. Elnounu and M. Memon, Non-linear finite element analysis of shear wall-floor slab junction. In: D.R. Owen, E. Hinton and E. Oñate, Editors, Proc Second Int. Conf. on Computational Plasticity, Pineridge Press, Swansea, Wales (1989), pp. 1319–1330.
- [6] Calvi GM, Via G, Vintzileou E. Reinforced concrete infilled frames, In: RC frames under earth-quake loading, CEB Bulletin 231, Thomas Telford, 1996, 231-284.
- [7] Červenka V, Jendele L, Červenka J, ATENA Theory Manual. Cervenka Consulting; 2009.
- [8] Cervera M., Oliver J., Manzoli O. A rate-dependent isotropic damage model for the seismic analysis of concrete dams. Earthquake Engineering and Structural Dynamics 25 (1996), pp. 987–1010.
- [9] de Borst, R. (1986), Non-linear analysis of frictional materials, Ph.D. Thesis, Delft University of Technology, 1986.
- [10] Dolšek M, Fajfar P. Simplified non-linear seismic analysis of infilled reinforced concrete frames. Earthquake Engineering and Structural Dynamics 2005; 34: 49-66.
- [11] Dolšek M, Fajfar P. Soft storey effects in uniformly infilled reinforced concrete frames. Journal of Earthquake Engineering 2001; 5(1): 1-12.
- [12] Dolšek M, Fajfar, P. Mathematical modelling of an infilled RC frame structure based on the results of pseudo-dynamic tests, Earthquake Engineering Structural Dynamics 2002; 31: 1215-1230.
- [13] EC8. Eurocode 8: Design of Structures for Earthquake Resistance. European Committee for Standardisation: Brussels, Belgium, The European Standard EN 1998-1: 2004.
- [14] El-Mezaini, N., and Citipitioglu, E. (1991). Finite element analysis of prestressed and reinforced concrete structures. Journal of Structural Engineering, 117(10), 2851–2864.
- [15] Elwi, A.E., Hrudey, T.M., Finite element model for curved embedded reinforcement. J. Eng. Mech. Div. 115 4 (1989), pp. 740–745.
- [16] Etse, G., Theoretische und numerische Untersuchung zum diffusen und lokalisierten Versagen in Beton, Ph.D. Thesis, University of Karlsruhe 1992.
- [17] Feenstra, P.H., Computational Aspects of Bi-axial Stress in Plain and Reinforced Concrete. Ph.D. Thesis, Delft University of Technology, 1993.
- [18] Feenstra, P.H., Rots, J.G., Amesen, A., Teigen, J.G., Hoiseth, K.V., A 3D Constitutive Model for Concrete Based on Co-rotational concept. Proc. EURO-C 1998, 1, pp. 13-22.

- [19] Fragiadakis, M., Papadrakakis, M. Modelling, analysis and reliability of seismically excited structures: Computational issues. *International Journal of Computational Methods*, 5(4): 483–511, 2008.
- [20] Ghobarah A, Saatcioglu M, Nistor I. The impact of the 26 December 2004 earthquake and tsunami on structures and infrastructure. *Engineering Structures* 2006; 28(2): 312-326.
- [21] González Vidosa, F., Kotsovos, M.D. Pavlović, M.N. Three-dimensional finite element analysis of structural concrete. In: N. Bicanic and H. Mang, Editors, *Computer Aided Analysis and Design of Concrete Structures Vol. 2*, Pineridge Press, Swansea (1990), pp. 1029–1040.
- [22] Isenberg J, Levine HS. Analysis of reinforced concrete under shock loading. *Finite Element Analysis of Reinforced Concrete Structures*, ASCE Task Committee on Concrete and Masonry Structures, ASCE, 1985. pp. 444–464.
- [23] Kakaletsis DJ, Karayannis CG. Influence of masonry strength and openings on infilled RC frames under cycling loading. *Journal of Earthquake Engineering* 2008; 12(2): 197-221.
- [24] Kent, D.C., Park, R. Flexural members with confined concrete. *Journal of Structural Division*; 97(7): 1969-1990, 1971.
- [25] Lagaros ND. Life-cycle cost analysis of construction practices, *Bulletin of Earthquake Engineering* 2007; 5: 425-442.
- [26] Madan, A., Reinhorn, A.M., Mander, J.B., Valles, R.E., Modelling of masonry infill panels for structural analysis. *Journal of Structural Engineering* 1997; 123(10): 1295-1302.
- [27] Marini A, Spacone E. Analysis of reinforced concrete elements including shear effects. *ACI Structural Journal* 2006; 103(5): 645-655.
- [28] McKenna F, Fenves GL. *The OpenSees Command Language Manual* (1.2. edn). PEER, 2001
- [29] Menegotto, M., Pinto, P.E. Method of analysis for cyclically loaded reinforced concrete plane frames including changes in geometry and non-elastic behaviour of elements under combined normal force and bending. *Proceedings, IABSE Symposium on Resistance and Ultimate De-formability of Structures Acted on by Well Defined Repeated Loads*: 15-22, 1973.
- [30] Menetrey, Ph., Walther, R., Zimmerman, Th., Willam, K.J., Regan, P.E. Simulation of punching failure in reinforced concrete structures. *Journal of Structural Engineering*, 1997, 123(5), pp 652-659.
- [31] Mitchell D, DeVall RH, Kobayashi K, Tinawi R, Tso WK. Damage to concrete structures due to the January 17, 1995, Hyogo-ken Nanbu (Kobe) earthquake, *Canadian Journal of Civil Engineering* 1996; 23(3): 757-770.

- [32] Owen, J.M., Figueiras, J.A., Damjanic, F., Finite Element Analysis of Reinforced and Pre-stressed concrete structures including thermal loading, *Comp. Meth. Appl. Mech. Eng.*, 1983, 41, pp 323-366.
- [33] Park, R., and Paulay, T., 1975, *Reinforced Concrete Structures*, John Wiley & Sons, Inc., 1975, 800 pp.
- [34] Perera, R., Gomez, S., Alarcon E., Experimental and analytical study of masonry infill reinforced concrete frames retrofitted with steel braces. *Journal of Structural Engineering* 2004; 130(12): 2032-2039.
- [35] Phillips, D.V., Zienkiewicz, O.C. (1976) *Finite Element Analysis of Concrete Structures*, Proc. Instn. Civ. Eng., Part 2, 61, 59-88.
- [36] Pramono, E, Willam, K.J., *Fracture Energy-Based Plasticity Formulation of Plain Concrete*, ASCE-JEM, 1989, 115, pp 1183-1204.
- [37] Rashid, Y.R. (1968), *Ultimate Strength Analysis of Pre-stressed Concrete Pressure Vessels*, Nuclear Engineering and Design, 1968, 7, pp 334-344.
- [38] Repapis C, Zeris C, Vintzileou E. Evaluation of the seismic performance of existing RC buildings: I. Suggested methodology, *Journal of Earthquake Engineering* 2006; 10(2): 265-287.
- [39] Rots, J.G., Blaauwendraad, J., Crack models for concrete: discrete or smeared? Fixed, multi-directional or rotating? *HERON* 1989, 34 (1).
- [40] Saneinejad A, Hobbs B. Inelastic design of infilled frames. *Journal of Structural Engineering* 1995; 121(4): 634-650.
- [41] Scott, B.D., Park, R., Priestley, M.J.N. Stress-strain behaviour of concrete confined by overlap-ping hoops at low and high strain rates. *ACI Journal*; 79: 13-27, 1982.
- [42] Simo, J.C., Ju, J.W., Strain and Stress-based Continuum Damage Models-I. Formulations, II Computational Aspects, *Int. J. Solids Structures*, 1987, 23(7), pp 821-869.
- [43] Sullivan TJ, Priestley MJN, Calvi GM. Development of an innovative seismic design procedure for frame-wall structures. *Journal of Earthquake Engineering* 2005; 9(2): 279-307.
- [44] Watanabe F. Behaviour of reinforced concrete buildings during the Hyougoken-Nanbu earth-quake. *Cement and Concrete Composites* 1997; 19(3): 203-211.
- [45] Wilkins, M.L., *Calculation of Elastic-Plastic Flow*, *Methods of Computational Physics*, 3, Academic Press, New York, 1964.
- [46] Zienkiewicz, O.C., Owen, D.R.J., Phillips, D.V., Nayak, G.C., *Finite element methods in the analysis of reactor vessels*. *Nuclear Engineering Design* 20 (1972), pp. 507-541.

4. Simulation – Three-Dimensional Solid Finite Element Modeling with Embedded Reinforcement

4.1 Introduction

In three-dimensional (3D) nonlinear finite-element (FE) analysis of reinforced concrete (RC) structures three methods available for the simulation of reinforcement are smeared, discrete, and embedded (ASCE 1982). The smeared formulation is more suitable to surface-type structures, where the distributed-reinforcing mesh permits modeling each layer of reinforcement with a membrane layer of equal cross-sectional area. For sparsely located (nonuniformly spaced) reinforcing bars, either the discrete or embedded formulation is more appropriate. In the discrete formulation, the rebars are often modeled with axial elements located at the boundaries of concrete elements. An obvious restriction is then imposed by having to use a concrete element mesh based on the rebar locations, rather than the need to simulate the flow of stresses. Especially in 3D applications, this can lead to prohibitive computational costs due to the use of many unnecessarily small elements and/or inaccuracies caused by elements with undesirable-aspect ratios. To alleviate these problems, some investigators have altered the actual arrangement of reinforcement during FE modeling (Abdel-Halim and Abu-Lebdeh 1989; Gonzalez Vidosa et al 1990).

In order to remedy such shortcomings, embedded formulation is preferable. This method, however, has mainly been used in two-dimensional (2D) FE analyses. The original formulation by Phillips and Zienkiewicz (1976) was modified by Chang et al. (1987) to allow for a straight-rebar segment to be placed at any angle with respect to the local axes of isoparametric- concrete elements. Balakrishnan and Murray (1986) introduced an embedded formulation with bond-slip capability between reinforcement and concrete. Further improvements by Elwi and Hruday (1989) allowed for a more general embedded curved reinforcement formulation. El-Mezaini and Citipitioglu (1991) introduced isoparametric elements with movable nodes to arrive at more efficient formulation when bond-slip is modeled.

The inherent requirement in the current embedded formulations is that the global coordinates of the intersection points of individual reinforcement and concrete elements should be provided by the analyst. While such data input in 2D models may be manageable, the task of identifying such points, their correspondence with each concrete element, and the manual input of coordinates for many such points in 3D applications is formidable Fig. 4-1. These problems, and difficulties associated with calculation of stiffness for arbitrary location of bar elements embedded in 3D meshes,

have led to some restrictions, simplifications, and approximations in 3D FE analyses; Isenberg and Levine (1985) restricted the embedded bars to pass through the centers of hexahedral concrete elements, Cervera (1986) smeared a group of bars at a given location and used them as embedded layers inside the concrete-solid elements, and Zienkiewicz et al. (1972) and Bhatt et al. (1989) restricted the embedded bars to being parallel to the local-isoparametric coordinates.

A systematic approach is presented to facilitate the use of embedded formulation in 3D FE analysis of concrete structures. With this procedure for each straight segment of reinforcement, only the end point coordinates in the global axes need to be provided by the analyst, which are then used to automatically map the entire reinforcement cage in a mesh of solid isoparametric concrete elements. By applying the principle of virtual work, the stiffness of each segment of reinforcement can be computed and added to the corresponding concrete element stiffness.

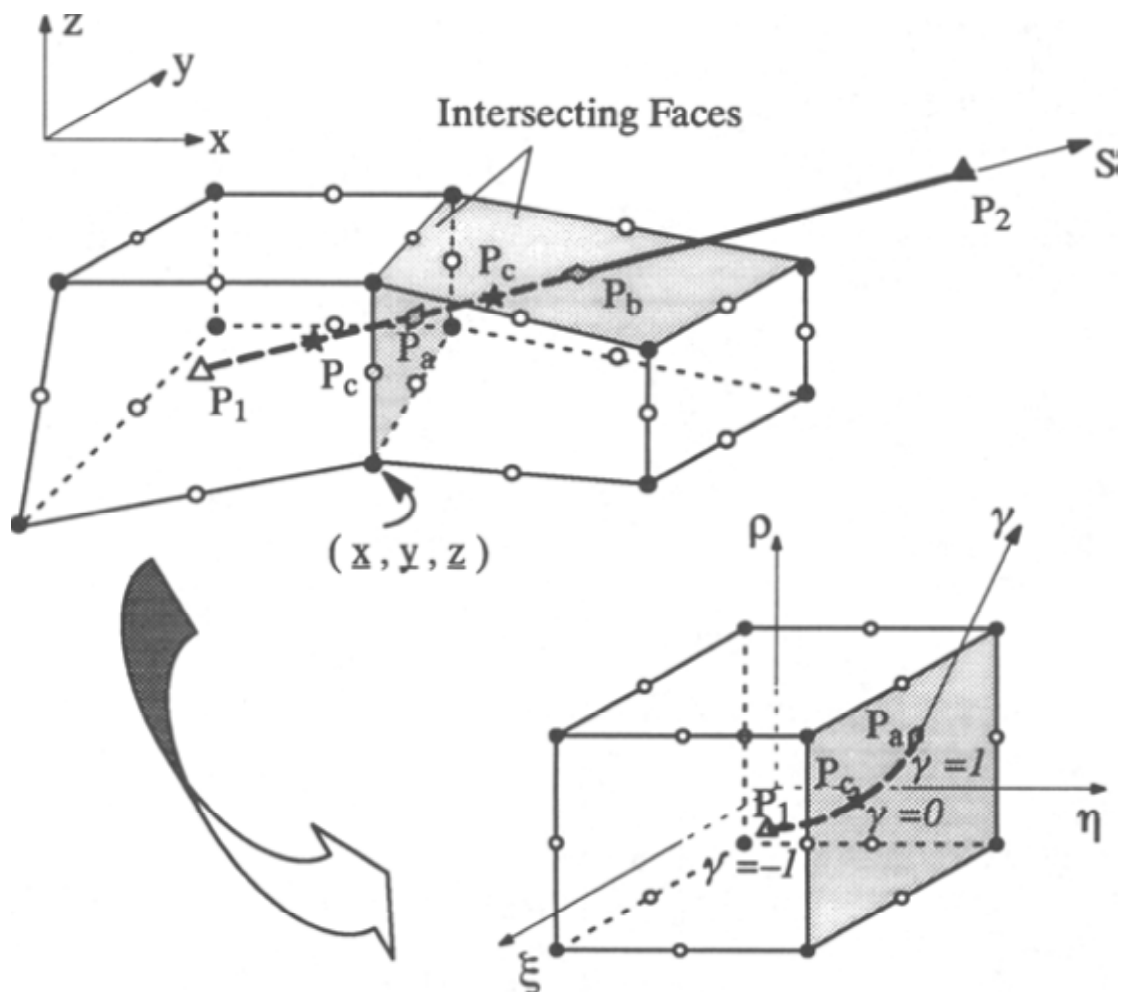


Fig. 4.1 Embedded reinforcement in 3D Mesh of Concrete Elements

4.2 Formulation

A procedure is presented to map a straight segment of reinforcement, P_1P_2 Fig. 4.1, into a given mesh of solid elements, and to incorporate the stiffness of each embedded portion such as P_1P_a , in the surrounding concrete element stiffness. It is assumed that the concrete element connectivity data – nodal incidences and coordinates – are available.

4.3 Origination/ Termination Point of Reinforcement Segment

Consider the coordinates (x , y , and z) of points P_1 and P_2 , defining a straight portion of reinforcement, are given Fig. 4.1. It is required to identify the concrete elements containing these points. A point such as P_1 is contained in a given concrete element if its coordinates, ξ_{P_1} , η_{P_1} and ρ_{P_1} , in the element local axes satisfy

$$-1 \leq \xi_{P_1}, \quad \eta_{P_1}, \quad \rho_{P_1} \leq 1 \quad (4.1)$$

Starting from the first element, the global coordinates $(x, y, z)_{P_1}$ of P_1 are mapped back into the current element local coordinate system in order to examine (4.1). The inverse mapping procedure, which is a 3D extension of the method proposed by Elwi and Hrudehy (1989), is used for this purpose. In the isoparametric formulation the global coordinates (x , y , and z) of a generic point within a solid element are expressed as

$$\begin{Bmatrix} x \\ y \\ z \end{Bmatrix} = \begin{bmatrix} \langle \varphi \rangle & 0 & 0 \\ 0 & \langle \varphi \rangle & 0 \\ 0 & 0 & \langle \varphi \rangle \end{bmatrix} \begin{Bmatrix} \{x\} \\ \{y\} \\ \{z\} \end{Bmatrix} \quad (4.2)$$

where $\{x\}$, $\{y\}$, and $\{z\}$ = vectors of element nodal coordinates, and

$$[\varphi] = [\varphi(\xi, \eta, \rho)] = \{\varphi\}^T = [\varphi_1(\xi, \eta, \rho), \varphi_2(\xi, \eta, \rho), \varphi_3(\xi, \eta, \rho)] \quad (4.3)$$

represents the row vector of displacement-shape functions. It follows that

$$\begin{Bmatrix} dx \\ dy \\ dz \end{Bmatrix} = [J]^T \begin{Bmatrix} d\xi \\ d\eta \\ d\rho \end{Bmatrix} \quad (4.4)$$

or

$$\begin{Bmatrix} d\xi \\ d\eta \\ d\rho \end{Bmatrix} = [J]^{-1} \begin{Bmatrix} dx \\ dy \\ dz \end{Bmatrix} \quad (4.5)$$

where $[J]$ = the Jacobian matrix expressed as

$$[J] = \begin{Bmatrix} \frac{\partial \langle \varphi \rangle}{\partial \xi} \\ \frac{\partial \langle \varphi \rangle}{\partial \eta} \\ \frac{\partial \langle \varphi \rangle}{\partial \rho} \end{Bmatrix} [\{x\}, \{y\}, \{z\}] \quad (4.6)$$

From (4.2), the coordinates $(\xi, \eta, \rho)_{P_1}$ are the roots of the following set of equations:

$$\begin{Bmatrix} x \\ y \\ z \end{Bmatrix}_{P_1} - \begin{bmatrix} \langle \varphi \rangle & 0 & 0 \\ 0 & \langle \varphi \rangle & 0 \\ 0 & 0 & \langle \varphi \rangle \end{bmatrix} \begin{Bmatrix} \{x\} \\ \{y\} \\ \{z\} \end{Bmatrix} = \{0\} \quad (4.7)$$

A Newton-Raphson iterative procedure has been used for solution. With an initial estimate of

$$\begin{Bmatrix} \xi \\ \eta \\ \rho \end{Bmatrix}_{P_1}^0 = \{0\} \quad (4.8)$$

the solution after $n + 1$ iterations is determined as

$$\begin{Bmatrix} \xi \\ \eta \\ \rho \end{Bmatrix}_{P_1}^{n+1} = \begin{Bmatrix} \xi \\ \eta \\ \rho \end{Bmatrix}_{P_1}^n + \begin{Bmatrix} \Delta \xi \\ \Delta \eta \\ \Delta \rho \end{Bmatrix}_{P_1}^{n+1} \quad (4.9)$$

where

$$\begin{Bmatrix} \Delta \xi \\ \Delta \eta \\ \Delta \rho \end{Bmatrix}_{P_1}^{n+1} = [J^n]^{T-1} \left[\begin{Bmatrix} x \\ y \\ z \end{Bmatrix}_{P_1} - \begin{bmatrix} \langle \varphi^n \rangle & 0 & 0 \\ 0 & \langle \varphi^n \rangle & 0 \\ 0 & 0 & \langle \varphi^n \rangle \end{bmatrix} \begin{Bmatrix} \{x\} \\ \{y\} \\ \{z\} \end{Bmatrix} \right] \quad (4.10a)$$

$$[J^n] = [J(\xi^n, \eta^n, \rho^n)] \quad (4.10b)$$

$$[\varphi^n] = [\varphi(\xi^n, \eta^n, \rho^n)] \quad (4.10c)$$

The preceding solution scheme has been found to converge rapidly. For the current element if the converged values do not satisfy (4.1), the procedure is repeated using the nodal coordinates of the next element until the element containing P_1 is identified.

4.4 Intersection of Reinforcement Segment with Boundaries of Concrete Elements

Upon identification of the element containing an origination point P_1 of a straight reinforcement segment P_1P_2 (Fig. 4.1), the intersection points of P_1P_2 (P_a , e.g.) with the face(s) of concrete-solid elements should be determined. For this purpose the equation of line P_1P_2 is written in a parametric form as

$$\begin{Bmatrix} x(S) \\ y(S) \\ z(S) \end{Bmatrix} = \begin{Bmatrix} x \\ y \\ z \end{Bmatrix}_{P_1} + S \left[\begin{Bmatrix} x \\ y \\ z \end{Bmatrix}_{P_2} - \begin{Bmatrix} x \\ y \\ z \end{Bmatrix}_{P_1} \right] \quad 0 \leq S \leq 1 \quad (4.11)$$

For locating the intersection point of the preceding line with a face of the current element, all six faces should be considered. The equation of a typical face of the element may be written as

$$\mathbf{P}_o \mathbf{P} \cdot \mathbf{N} = 0 \quad (4.12)$$

where \mathbf{P}_o = a corner node; \mathbf{P} = a generic point on the surface; and \mathbf{N} = normal to this face. Eq. (4.12) defines a planar surface. Therefore, the procedure will be exact for 8-noded linear solid isoparametric elements while introducing some approximation for higher-order elements with curved surfaces.

The coordinates of the intersection point, P_a , is determined from (4.11), with S determined as

$$S = \frac{\mathbf{P}_1 \mathbf{P}_o \cdot \mathbf{N}}{\mathbf{P}_1 \mathbf{P}_2 \cdot \mathbf{N}} \quad (4.13)$$

At this stage the length of the reinforcement segment contained in the current element and the face number where the segment leaves the element are available. The algorithm proceeds by shortening the line segment $P_1 P_2$ by an amount $P_1 P_a$ and shifting P_1 to P_a , (Fig. 4.1). Now the next element to be examined for intersection with the remaining line segment is identified as the one that shares the face of the element from which the line segment exited; this is accomplished by scanning through the nodal incidences of the faces of all the remaining elements and picking the match.

Following the foregoing procedure, each reinforcement line is divided into segments contained in concrete elements. A concrete element may contain one or more embedded-rebar segments with arbitrary orientations. In a special case where a rebar segment lies on a face shared by adjacent elements, the very first element identified to contain a point on the segment is registered to contain the entire segment. Also, when a rebar segment passes through the element edges, then the intersection point could belong to any of the adjoining elements; in such cases the length of the segment is slightly decreased in order to identify a single element containing that point.

4.5 Reinforced Concrete Element Stiffness

Depending on the order of displacement field for concrete elements, additional nodes (e.g., P_c in Fig. 4.1) may be introduced between the end nodes of each bar segment to satisfy compatibility in case of perfect bond assumption. The stiffness of each reinforced concrete element may then be computed using numerical integration in the element natural (ξ, η, ρ) coordinate system. The integration points of each bar segment in its local axis (γ Fig. 4.1) are first located in the global (x, y, z) system using the standard isoparametric transformations similar to (4.2). These points are then mapped back to the corresponding-parent-element coordinates using the aforementioned inverse mapping procedure.

4.6 Constitutive law for 3D solid elements

4.6.1 Fracture-Plastic Constitutive Model

4.6.1.1 Introduction

Fracture-plastic model combines constitutive models for tensile (fracturing) and compressive (plastic) behavior. The fracture model is based on the classical orthotropic smeared crack formulation and crack band model. It employs Rankine failure criterion, exponential softening, and it can be used as rotated or fixed crack model. The hardening/softening plasticity model is based on Menetrey-Willam failure surface. The model uses return mapping algorithm for the integration of constitutive equations. Special attention is given to the development of an algorithm for the combination of the two models. The combined algorithm is based on a recursive substitution, and it allows for the two models to be developed and formulated separately. The algorithm can handle cases when failure surfaces of both models are active, but also when physical changes such as crack closure occur. The model can be used to simulate concrete cracking, crushing under high confinement, and crack closure due to crushing in other material directions.

Although many papers have been published on plasticity models for concrete (for instance PRAMONO, WILLAM 1989, MENETREY et al 1997, FEENSTRA 1993, 1998 ETSE 1992) or smeared crack models (RASHID 1968, CERVENKA and GERSTLE 1971, BAZANT and OH 1983, DE BORST 1986, ROTS 1989), there are not many descriptions of their successful combination in the literature. OWEN et al. (1983) presented a combination of cracking and visco-plasticity.

Comprehensive treatise of the problem was provided also by de BORST (1986), and recently several works have been published on the combination of damage and plasticity (SIMO and JU 1987, MESCHKE et al. (1998). The presented model differs from the above formulations by ability to handle also physical changes like for instance crack closure, and it is not restricted to any particular shape of hardening/softening laws. Also within the proposed approach it is possible to formulate the two models (i.e. plastic and fracture) entirely separately, and their combination can be provided in a different algorithm or model. From programming point of view such approach is well suited for object oriented programming.

The method of strain decomposition, as introduced by DE BORST (1986), is used to combine fracture and plasticity models together. Both models are developed within the framework of return mapping algorithm by WILKINS (1964). This approach guarantees the solution for all magnitudes of strain increment. From an algorithmic

point of view the problem is then transformed into finding an optimal return point on the failure surface.

The combined algorithm must determine the separation of strains into plastic and fracturing components, while it must preserve the stress equivalence in both models. The proposed algorithm is based on a recursive iterative scheme. It can be shown that such a recursive algorithm cannot reach convergence in certain cases such as, for instance, softening and dilating materials. For this reason the recursive algorithm is extended by a variation of the relaxation method to stabilize convergence.

4.6.1.2 Material Model Formulation

The material model formulation is based on the strain decomposition into elastic ε_{ij}^e , plastic ε_{ij}^p and fracturing ε_{ij}^f components (DE BORST 1986).

$$\varepsilon_{ij} = \varepsilon_{ij}^e + \varepsilon_{ij}^p + \varepsilon_{ij}^f \quad (4.14)$$

The new stress state is then computed by the formula:

$$\sigma_{ij}^n = \sigma_{ij}^{n-1} + E_{ijkl}(\Delta\varepsilon_{kl} - \Delta\varepsilon_{kl}^p - \Delta\varepsilon_{kl}^f) \quad (4.15)$$

where the increments of plastic strain $\Delta\varepsilon_{kl}^p$ and fracturing strain $\Delta\varepsilon_{kl}^f$ must be evaluated based on the used material models.

4.6.1.3 Rankine-Fracturing Model for Concrete Cracking

Rankine criterion is used for concrete cracking:

$$F_i^f = \sigma_{ii}^{t'} - f_{ti}' \leq 0 \quad (4.16)$$

It is assumed that strains and stresses are converted into the material directions, which in case of rotated crack model correspond to the principal directions, and in case of fixed crack model, are given by the principal directions at the onset of cracking. Therefore, $\sigma_{ii}^{t'}$ identifies the trial stress and f_{ti}' tensile strength in the material direction i . Prime symbol denotes quantities in the material direction. The trial stress state is computed by the elastic predictor.

$$\sigma_{ij}^{t'} = \sigma_{ij}^{n-1} + E_{ijkl}\Delta\varepsilon_{kl}' \quad (4.17)$$

If the trial stress does not satisfy (4.16), the increment of fracturing strain in direction i can be computed using the assumption that the final stress state must satisfy (4.17).

$$F_i^f = \sigma_{ii}^{t'} - f_{ti}' = \sigma_{ii}^{t'} - E_{ijkl}\Delta\varepsilon_{kl}' - f_{ti}' = 0 \quad (4.18)$$

This equation can be further simplified under the assumption that the increment of fracturing strain is normal to the failure surface, and that always only one failure

surface is being checked. For failure surface k , the fracturing strain increment has the following form.

$$\Delta \varepsilon_{ij}^{f'} = \Delta \lambda \partial F_k^f / \partial \sigma_{ij} = \Delta \lambda \delta_{ik} \quad (4.19)$$

After substitution into (4.18) a formula for the increment of the fracturing multiplier λ is recovered.

$$\Delta \lambda = (\sigma_{kk}^{t'} - f_{tk}') / E_{kkkk} \text{ and } w_k^{max} = L_t (\varepsilon_{kk}^{f'} + \Delta \lambda) \quad (4.20)$$

This equation must be solved by iterations since for softening materials the value of current tensile strength $f_t'(w_k^{max})$ is a function of the crack opening w , and is based on Hordijk's formula:

Exponential Crack Opening Law.

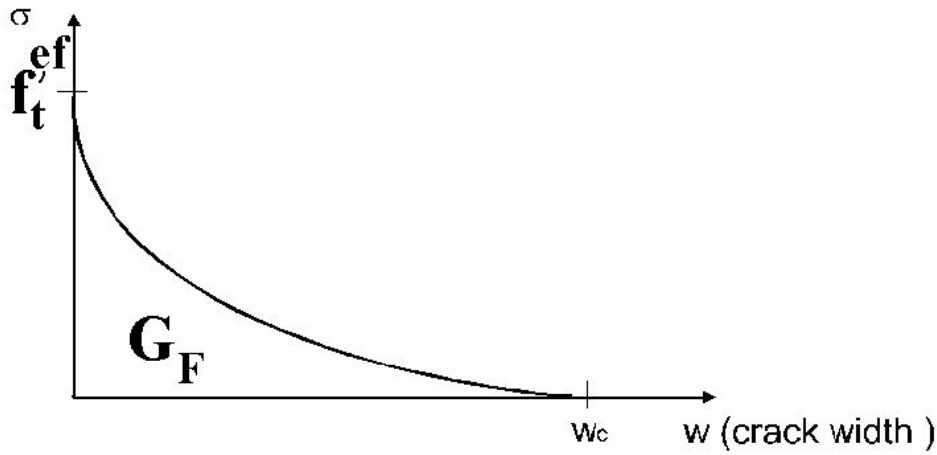


Fig. 4.2 Exponential crack opening law

This function of crack opening was derived experimentally by HORDIJK (1991).

$$\frac{\sigma}{f_t^{ef}} = \left\{ 1 + \left(c_1 \frac{w}{w_c} \right)^3 \right\} \exp \left(-c_2 \frac{w}{w_c} \right) - \frac{w}{w_c} (1 + c_1^3) \exp(-c_2)$$

$$w_c = 5.14 \frac{G_f}{f_t^{ef}}$$

where w is the crack opening, w_c is the crack opening at the complete release of stress, σ is the normal stress in the crack (crack cohesion). Values of the constants are, $c_1=3$, $c_2=6.93$. G_F is the fracture energy needed to create a unit area of stress-free crack, f_t^{ef} is the effective tensile strength derived from a failure function.

The crack opening w is computed from the total value of fracturing strain $\varepsilon_{kk}^{f'}$ in direction k , plus the current increment of fracturing strain $\Delta \lambda$, and this sum is multiplied by the characteristic length L_t . The characteristic length as a crack band size was introduced by BAZANT and OH. Various methods were proposed for the crack band

size calculation in the framework of finite element method. FEENSTRA (1993) suggested a method based on integration point volume, which is not well suited for distorted elements. A consistent and rather complex approach was proposed by OLIVIER. In the presented work the crack band size L_t is calculated as a size of the element projected into the crack direction, Fig. 4.3. CERVENKA V. et al. (1995) showed that this approach is satisfactory for low order linear elements, which are used throughout this study. They also proposed a modification, which accounts for cracks that are not aligned with element edges.

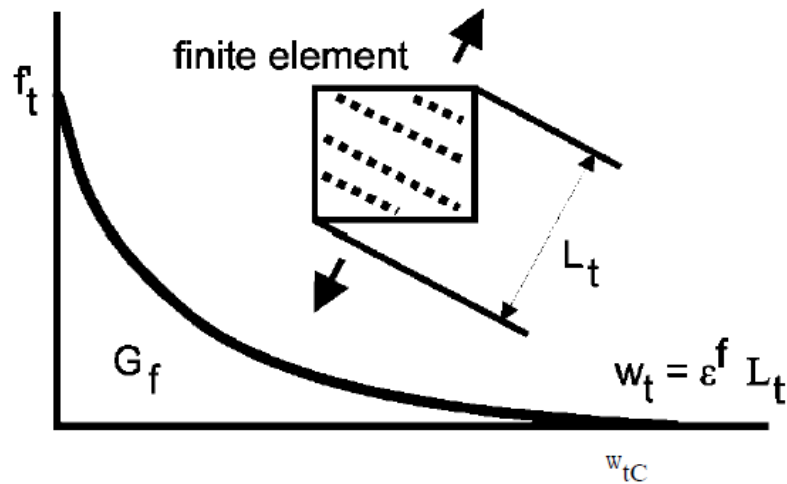


Fig. 4.3 Tensile softening and characteristic length

Equation (4.20) can be solved by recursive substitutions. It is possible to show by expanding $f_t'(w_k^{max})$ into a Taylor series that this iteration scheme converges as long as:

$$|-(\partial f_t'(w_k^{max})/\partial w)| < (E_{kkkk}/L_t) \quad (4.21)$$

Equation (4.21) is violated for softening materials only when snap back is observed in the stress-strain relationship, which can occur if large finite elements are used. In the standard displacement based finite element method, the strain increment is given, therefore, a snap back on the constitutive level cannot be captured. This means that the critical region, with snap back on the softening curve, will be skipped in a real calculation, which physically means, that the energy dissipated by the system will be over estimated. This is of course undesirable, and finite elements smaller than $L < E_{kkkk}/|\partial f_t'(0)/\partial w|$ should be used, where $\partial f_t'(0)/\partial w$ denotes the initial slope of the crack softening curve.

It is important to distinguish between total fracturing strain ϵ_{ij}^f , which corresponds to the maximal fracturing strain reached during the loading process, and current fracturing strain ϵ_{ij}^f ,

which can be smaller due to crack closure, and is computed using (4.22) derived by ROTS and BLAUWENDRAAD.

$$\varepsilon_{kl}^{\prime f} = (E_{ijkl} + E_{ijkl}^{\prime cr})^{-1} E_{klmn} \varepsilon_{mn}^{\prime} \text{ and } E_{ijkl}^{\prime cr} \text{ is defined by } \sigma_{ij}^{\prime} = E_{ijkl}^{\prime cr} \varepsilon_{kl}^{\prime f} \quad (4.22)$$

The fourth order crack tensor $E_{ijkl}^{\prime cr}$ represents the cracking stiffness in the local material directions.

In the current formulation, it is assumed, that there is no interaction between normal and shear components. Thus, the crack tensor is given by the following formulas.

$$E_{ijkl}^{\prime cr} = 0 \text{ for } i \neq k \text{ and } j \neq l \quad (4.23)$$

Mode I crack stiffness equals

$$E_{ijkl}^{\prime cr} = \frac{f_t^{\prime}(w_k^{\max})}{\varepsilon_{ij}^{\prime f}} \quad (4.24)$$

and mode II and III crack stiffness is assumed as:

$$E_{ijij}^{\prime cr} = s_F \min(E_{iiii}^{\prime cr}, E_{jjjj}^{\prime cr}), \text{ (no summation of indices)} \quad (4.25)$$

where $i \neq j$, and s_F is a shear factor coefficient that defines a relationship between the normal and shear crack stiffness. The default value of s_F is 20.

Shear strength of a cracked concrete is calculated using the Modified Compression Field Theory of VECHIO and COLLINS (1986).

$$\sigma_{ij} \leq 0.18 \sqrt{f_c^{\prime}} / (0.31 + 24w / (a_g + 16)), \quad i \neq j \quad (4.26)$$

Where f_c^{\prime} is the compressive strength in MPa, a_g is the maximum aggregate size in mm and w is the maximum crack width in mm at the given location. This model is activated by specifying the maximum aggregate size a_g otherwise the default behavior is used where the shear stress on a crack surface cannot the tensile strength.

The secant constitutive matrix in the material direction was formulated by ROTS and BLAUWENDRAAD in the matrix format.

$$\mathbf{E}^s = \mathbf{E} - \mathbf{E}(\mathbf{E}^{\prime cr} + \mathbf{E})^{-1} \mathbf{E} \quad (4.27)$$

Strain vector transformation matrix \mathbf{T}^{ε} (i.e. global to local strain transformation matrix) can be used to transform the local secant stiffness matrix to the global coordinate system.

$$\mathbf{E}^s = \mathbf{T}^{\varepsilon T} \mathbf{E}^s \mathbf{T}^{\varepsilon} \quad (4.28)$$

It is necessary to handle the special cases before the onset of cracking, when the crack stiffness approaches infinity. Large penalty numbers are used for crack stiffness

in these cases.

4.6.1.4 Plasticity Model for Concrete Crushing

New stress state in the plastic model is computed using the predictor-corrector formula.

$$\sigma_{ij}^n = \sigma_{ij}^{n-1} + E_{ijkl}(\Delta\varepsilon_{kl} - \Delta\varepsilon_{kl}^p) = \sigma_{ij}^t - E_{ijkl}\Delta\varepsilon_{kl}^p = \sigma_{ij}^t - \sigma_{ij}^p \quad (4.29)$$

The plastic corrector σ_{ij}^p is computed directly from the yield function by return mapping algorithm.

$$F^P(\sigma_{ij}^t - \sigma_{ij}^p) = F^P(\sigma_{ij}^t - \Delta\lambda l_{ij}) = 0 \quad (4.30)$$

The crucial aspect is the definition of the return direction l_{ij} , which can be defined as

$$l_{ij} = E_{ijkl}(\partial G^P(\sigma_{kl}^t)/\partial\sigma_{kl}) \text{ then } \Delta\varepsilon_{kl}^p = \Delta\lambda(\partial G^P(\sigma_{kl}^t)/\partial\sigma_{kl}) \quad (4.31)$$

Where (σ_{kl}) is the plastic potential function, whose derivative is evaluated at the predictor stress state σ_{kl}^t to determine the return direction.

The failure surface of MENETREY, WILLAM is used in the current version of the material model.

$$F_{3P}^p = [\sqrt{1.5} \rho / f_c']^2 + m[(\rho / \sqrt{6} f_c')r(\theta, e) + \xi / \sqrt{3} f_c'] - c = 0 \quad (4.32)$$

Where

$$m = 3((f_c'^2 - f_t'^2)/f_c' f_t')(e/(e + 1))$$

$$r(\theta, e) = \frac{4(1-e^2)\cos^2\theta + (2e-1)^2}{2(1-e^2)\cos\theta + (2e-1)[4(1-e^2)\cos^2\theta + 5e^2 - 4e]^{1/2}}$$

In the above equations (ξ, ρ, θ) are Heigh-Vestergaard coordinates, f_c' and f_t' is compressive strength and tensile strength respectively. Parameter $e \in (0.5, 1.0)$ defines the roundness of the failure surface. The failure surface has sharp corners if $e = 0.5$, and is fully circular around the hydrostatic axis if $e = 1.0$.

The position of failure surfaces is not fixed but it can move depending on the value of strain hardening/softening parameter. The strain hardening is based on the equivalent plastic strain, which is calculated according to the following formula.

$$\Delta\varepsilon_{eq}^p = \min(\Delta\varepsilon_{ij}^p) \quad (4.33)$$

For Menetrey-Willam surface the hardening/softening is controlled by the parameter $c \in (0,1)$, which evolves during the yielding/crushing process by the following relationship:

$$c = (f'_c(\varepsilon_{eq}^p)/f'_c)^2 \quad (4.34)$$

In the above two formulas the expression $f'_c(\varepsilon_{eq}^p)$ indicates the hardening/softening law, which is based on the uniaxial compressive test. The law is shown in Fig. 4.4, where the softening curve is linear and the elliptical ascending part is given by the following formula:

$$\sigma = f_{co} + (f_c - f_{co})\sqrt{1 - (\varepsilon_c - \varepsilon_{eq}^p/\varepsilon_c)^2} \quad (4.35)$$

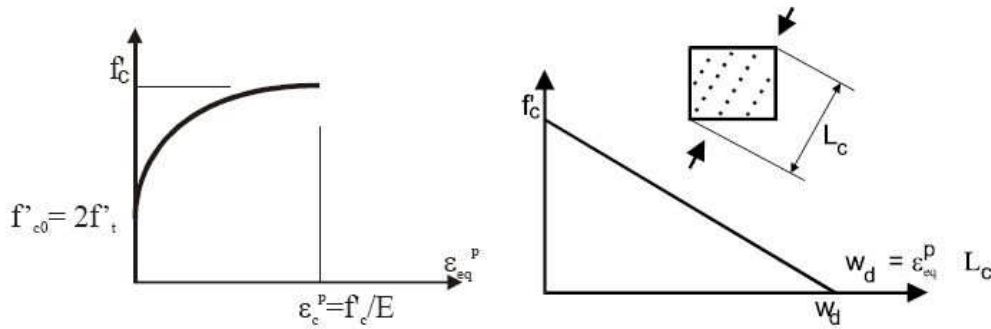


Fig. 4.4 Compressive hardening/softening and compressive characteristic length – based on experimental observations by VAN MIER

The law on the ascending branch is based on strains, while the descending branch is based on displacements to introduce mesh objectivity into the finite element solution, and its shape is based on the work of VAN MIER. The onset of nonlinear behavior f'_{co} is an input parameter as well as the value of plastic strain at compressive strength ε_c^p . The Fig. 4.3 shows typical values of these parameters. Especially the choice of the parameter f'_{co} should be selected with care, since it is important to ensure that the fracture and plastic surfaces intersect each other in all material stages. On the descending curve the equivalent plastic strain is transformed into displacements through the length scale parameter L_c . This parameter is defined by analogy to the crack band parameter in the fracture model in Sec. 4.1.1.3, and it corresponds to the projection of element size into the direction of minimal principal stresses. The square in (4.34) is due to the quadratic nature of the Menetry-Willam surface.

Return direction is given by the following plastic potential

$$G^p(\sigma_{ij}) = \beta(1/\sqrt{3}) I_1 + \sqrt{2J_2} \quad (4.36)$$

where β determines the return direction. If $\beta < 0$ material is being compacted during crushing, if $\beta = 0$ material volume is preserved, and if $\beta > 0$ material is dilating. In general the plastic model is non-associated, since the plastic flow is not perpendicular to the failure surface.

The return mapping algorithm for the plastic model is based on predictor-corrector approach as is shown in Fig. 4.5. During the corrector phase of the algorithm the failure surface moves along the hydrostatic axis to simulate hardening and softening. The final failure surface has the apex located at the origin of the Haigh-Vestergaard coordinate system. Secant method based Algorithm 1 is used to determine the stress on the surface, which satisfies the yield condition and also the hardening/softening law.

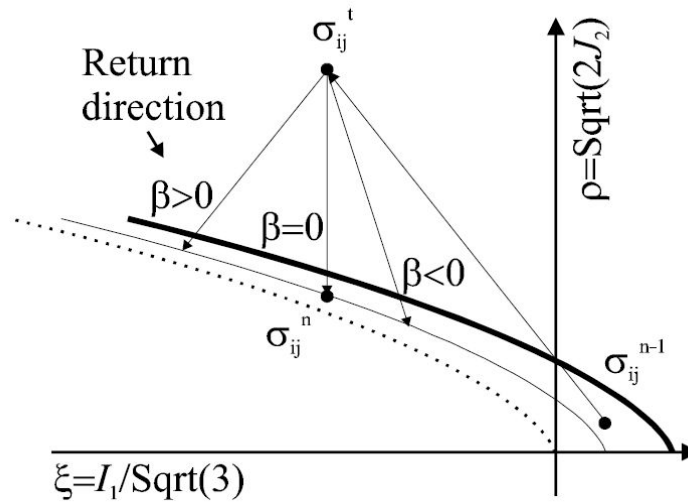


Fig. 4.5 Plastic predictor-corrector algorithm

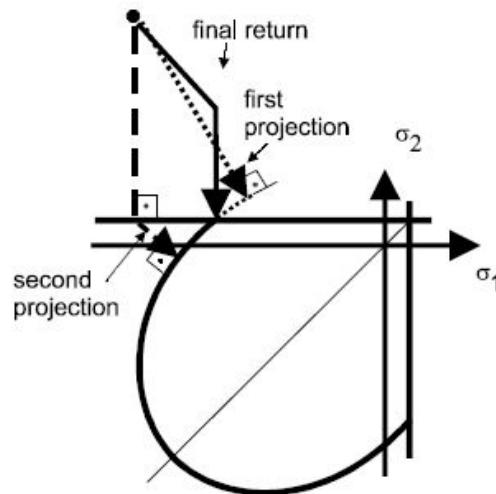


Fig. 4.6 Schematic description of the iterative process (4.38) – for clarity shown in two dimensions

Algorithm 1: (Input is $\sigma_{ij}^{n-1}, \varepsilon_{ij}^{p, n-1}, \Delta\varepsilon_{ij}^n$)

Elastic predictor:

$$\sigma_{ij}^t = \sigma_{ij}^{n-1} + E_{ijkl} \Delta \varepsilon_{kl}^n \quad (4.37)$$

Evaluate failure criterion:

$$f_A^p = F^p(\sigma_{ij}^t, \varepsilon_{ij}^{p n-1}), \quad \Delta \lambda_A = 0 \quad (4.38)$$

If failure criterion is violated i.e. $f_A^p > 0$

Evaluate return direction:

$$m_{ij} = \partial G^p(\sigma_{ij}^t) / \partial \sigma_{ij} \quad (4.39)$$

Return mapping:

$$F^p(\sigma_{ij}^t - \Delta \lambda_B E m_{ij}, \varepsilon_{ij}^{p n-1}) = 0 \Rightarrow \Delta \lambda_B \quad (4.40)$$

Evaluate failure criterion:

$$f_B^p = F^p(\sigma_{ij}^t - \Delta \lambda_B E m_{ij}, \varepsilon_{ij}^{p n-1} + \Delta \lambda_B m_{ij}) \quad (4.41)$$

Secant iterations (i) as long as:

$$|\Delta \lambda_A - \Delta \lambda_B| > e \quad (4.42)$$

New plastic multiplier increment:

$$\Delta \lambda = \Delta \lambda_A - f_A^p (\Delta \lambda_A - \Delta \lambda_B) / (f_B^p - f_A^p) \quad (4.43)$$

New return direction:

$$m_{ij}^{(i)} = (\partial G^p(\sigma_{ij}^t - \Delta \lambda_B E m_{ij}^{(i-1)})) / \partial \sigma_{ij} \quad (4.44)$$

Evaluate failure criterion:

$$f^p = F^p(\sigma_{ij}^t - \Delta \lambda_B E m_{ij}^{(i)}, \varepsilon_{ij}^{p n-1} + \Delta \lambda_B m_{ij}^{(i)}) \quad (4.45)$$

New initial values for secant iterations:

$$f_B^p < 0 \Rightarrow f_B^p = f^p, \Delta \lambda_B = \Delta \lambda \quad (4.46)$$

$$f_B^p \geq 0 \Rightarrow f_A^p = f^p, \Delta \lambda_A = \Delta \lambda_B, f_B^p = f^p, \Delta \lambda_B = \Delta \lambda \quad (4.47)$$

End of secant iteration loop

End of algorithm update stress and plastic strains.

$$\varepsilon_{ij}^{pn} = \varepsilon_{ij}^{p^{n-1}} + \Delta\lambda_B m_{ij}^{(i)}, \quad \sigma_{ij}^n = \sigma_{ij}^t - \Delta\lambda_B E m_{ij}^{(i)} \quad (4.48)$$

4.6.1.5 Combination of Plasticity and Fracture model

The objective is to combine the above models into a single model such that plasticity is used for concrete crushing and the Rankine fracture model for cracking. This problem can be generally stated as a simultaneous solution of the two following inequalities.

$$F^p(\sigma_{ij}^{n-1} + E_{ijkl}(\Delta\varepsilon_{kl} - \Delta\varepsilon_{kl}^f - \Delta\varepsilon_{kl}^p)) \leq 0 \text{ solve for } \Delta\varepsilon_{kl}^p \quad (4.49)$$

$$F^f(\sigma_{ij}^{n-1} + E_{ijkl}(\Delta\varepsilon_{kl} - \Delta\varepsilon_{kl}^p - \Delta\varepsilon_{kl}^f)) \leq 0 \text{ solve for } \Delta\varepsilon_{kl}^f \quad (4.50)$$

Each inequality depends on the output from the other one, therefore the following iterative scheme is developed.

Algorithm 2:

$$\text{Step 1: } F^p(\sigma_{ij}^{n-1} + E_{ijkl}(\Delta\varepsilon_{kl} - \Delta\varepsilon_{kl}^{f(i-1)} + b\Delta\varepsilon_{kl}^{cor(i-1)} - \Delta\varepsilon_{kl}^{p(i)})) \leq 0 \text{ solve for } \Delta\varepsilon_{kl}^{p(i)}$$

$$\text{Step 2: } F^f(\sigma_{ij}^{n-1} + E_{ijkl}(\Delta\varepsilon_{kl} - \Delta\varepsilon_{kl}^{p(i)} - \Delta\varepsilon_{kl}^{f(i)})) \leq 0 \text{ solve for } \Delta\varepsilon_{kl}^{f(i)}$$

Step 3:

$$\Delta\varepsilon_{ij}^{cor(i)} = \Delta\varepsilon_{ij}^{f(i)} - \Delta\varepsilon_{ij}^{f(i-1)} \quad (4.51)$$

Iterative correction of the strain norm between two subsequent iterations can be expressed as

$$\|\Delta\varepsilon_{ij}^{cor(i)}\| = (1 - b)a^f a^p \|\Delta\varepsilon_{ij}^{cor(i-1)}\| \quad (4.52)$$

Where

$$a^f = \|\Delta\varepsilon_{ij}^{f(i)} - \Delta\varepsilon_{ij}^{f(i-1)}\| / \|\Delta\varepsilon_{ij}^{p(i)} - \Delta\varepsilon_{ij}^{p(i-1)}\|$$

$$a^p = \|\Delta\varepsilon_{ij}^{p(i)} - \Delta\varepsilon_{ij}^{p(i-1)}\| / \|\Delta\varepsilon_{ij}^{cor}\|$$

and b is an iteration correction or relaxation factor, which is introduced in order to guarantee convergence. It is to be determined based on the run-time analysis of a^f and a^p , such that the convergence of the iterative scheme can be assured. The parameters a^f and a^p characterize the mapping properties of each model (i.e. plastic and fracture). It is possible to consider each model as an operator, which maps strain increment on the input into a fracture or plastic strain increment on the output. The

product of the two mappings must be contractive in order to obtain a convergence. The necessary condition for the convergence is:

$$|(1 - b)a^f a^p| < 1 \quad (4.53)$$

If b equals 0, an iterative algorithm based on recursive substitution is obtained. The convergence can be guaranteed only in two cases:

One of the models is not activated (i.e. implies a^f or $a^p = 0$).

There is no softening in either of the two models and dilating material is not used in the plastic part, which for the plastic potential in this work means $\beta \leq 0$, (4.46). This is a sufficient but not necessary condition to ensure that a^f and $a^p < 1$.

It can be shown that the values of a^f and a^p are directly proportional to the softening rate in each model. Since the softening model remains usually constant for a material model and finite element, their values do not change significantly between iterations. It is possible to select the scalar b such that the inequality (4.53) is satisfied always at the end of each iteration based on the current values of a^f and a^p . There are three possible scenarios, which must be handled, for the appropriate calculation of b :

$|a^f a^p| \leq x$, where x is related to the requested convergence rate. For linear rate it can be set to $x = 1/2$. In this case the convergence is satisfactory and $b = 0$.

$x < |a^f a^p| < 1$, then the convergence would be too slow. In this case b can be estimated as $b = 1 - |a^f a^p|/x$, in order to increase the convergence rate.

$1 \leq |a^f a^p|$, then the algorithm is diverging. In this case b should be calculated as

$b = 1 - x/|a^f a^p|$ to stabilize the iterations.

This approach guarantees convergence as long as the parameters a^p , a^f do not change drastically between the iterations, which should be satisfied for smooth and correctly formulated models. The rate of convergence depends on material brittleness, dilating parameter β and finite element size. It is advantageous to further stabilize the algorithm by smoothing the parameter b during the iterative process:

$$b = (b^{(i)} + b^{(i-1)})/2 \quad (4.54)$$

where the superscript i denotes values from two subsequent iterations. This will eliminate problems due to the oscillation of the correction parameter b . Important condition for the convergence of the above Algorithm 2 is that the failure surfaces of

the two models are intersecting each other in all possible positions even during the hardening or softening.

Additional constraints are used in the iterative algorithm. If the stress state at the end of the first step violates the Rankine criterion, the order of the first two steps in Algorithm 2 is reversed. Also in reality concrete crushing in one direction has an effect on the cracking in other directions. It is assumed that after the plasticity yield criterion is violated, the tensile strength in all material directions is set to zero.

On the structural level secant matrix is used in order to achieve a robust convergence during the strain localization process.

The proposed algorithm for the combination of plastic and fracture models is graphically shown in Fig. 4.6. When both surfaces are activated, the behavior is quite similar to the multi-surface plasticity (SIMO et al. 1988). Contrary to the multi-surface plasticity algorithm the proposed method is more general in the sense that it covers all loading regimes including physical changes such as for instance crack closure. Currently, it is developed only for two interacting models, and its extension to multiple models is not straightforward.

There are additional interactions between the two models that need to be considered in order to properly describe the behavior of a concrete material:

- a) After concrete crushing the tensile strength should be decrease as well
- b) According to the research work of Collins (VECHIO and COLLINS (1986)) and coworkers it was established the also compressive strength should decrease when cracking occurs in the perpendicular direction. This theory is called compression field theory and it is used to explain the shear failure of concrete beams and walls.

The interaction (a) is resolved by adding the equivalent plastic strain to the maximal fracturing strain in the fracture model to automatically increase the tensile damage based on the compressive damage such that fracturing strains satisfies the following condition:

$$\hat{\varepsilon}_{kk}^f \geq \frac{f'_t}{f'_c} \varepsilon_{eq}^p \quad (4.55)$$

The compressive strength reduction (b) is based on the following formula based proposed by Collins:

$$\sigma_c = r_c f'_c \quad (4.56)$$

$$r_c = \frac{1}{0.8+170\varepsilon_1}, r_c^{lim} \leq r_c \leq 1.0 \quad (4.57)$$

Where ε_1 is the tensile strain in the crack. In ATENA the largest maximal fracturing strain is used for ε_1 and the compressive strength reduction is limited by r_c^{lim} . If r_c^{lim} is not specified then no compression reduction is considered.

4.6.2 Tension stiffening effect

In heavily reinforced concrete structures the cracks cannot be fully developed and concrete contributes to the steel stiffness. This effect is called tension stiffening and in CC3DNonLinCementitious2 material it can be simulated by specifying a tension stiffening factor c_{ts} . This factor represents the relative limiting value of tensile strength in the tension softening diagram. The tensile stress cannot drop below the value given by the product of $c_{ts}f_t$ (see Fig. 4.7). The recommended default value for c_{ts} is 0.4 as recommended by CEB-FIP Model Code 1990.

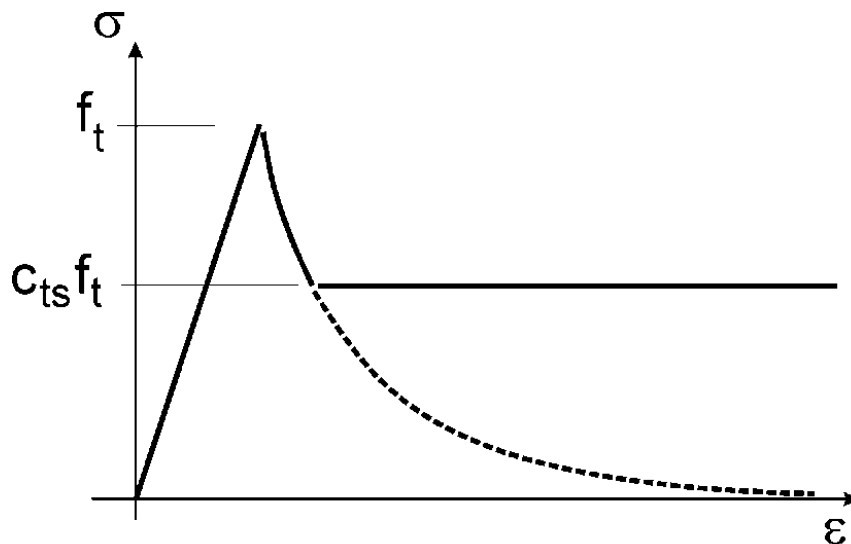


Fig. 4.7 Tension stiffening effect

4.6.3 Localization Limiters

So-called localization limiter controls localization of deformations in the failure state. It is a region (band) of material, which represents a discrete failure plane in the finite element analysis. In tension it is a crack, in compression it is a plane of crushing. In reality these failure regions have some dimension. However, since according to the experiments, the dimensions of the failure regions are independent on the structural size, they are assumed as fictitious planes. In case of tensile cracks, this approach is known as the "crack band theory", BAZANT, OH (1983). Here is the same concept used also for the compression failure. The purpose of the failure band is to eliminate two deficiencies, which occur in connection with the application of the finite element model: element size effect and element orientation effect.

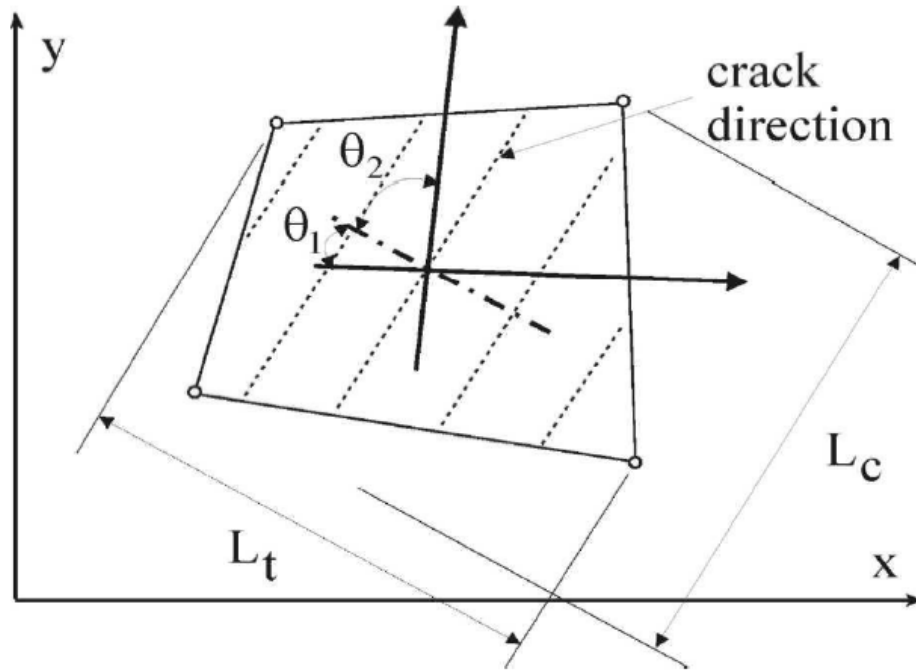


Fig. 4.8 Definition of localization bands – four-noded element

4.6.3.1 Element size effect.

The direction of the failure planes is assumed to be normal to the principal stresses in tension and compression, respectively. The failure bands (for tension L_t and for compression L_d) are defined as projections of the finite element dimensions on the failure planes as shown in Fig. 4.8.

4.6.3.2 Element orientation effect.

The element orientation effect is reduced, by further increasing of the failure band for skew meshes, by the following formula (proposed by CERVENKA et al. 1995).

$$L'_t = \gamma L_t, L'_d = \gamma L_d$$

$$\gamma = 1 + (\gamma^{max} - 1) \frac{\theta}{45}, \quad \theta \in (0; 45) \quad (4.58)$$

An angle θ is the minimal angle ($\min(\theta_1, \theta_2)$) between the direction of the normal to the failure plane and element sides. In case of a general quadrilateral element the element sides directions are calculated as average side directions for the two opposite edges. The above formula is a linear interpolation between the factor $\gamma=1.0$ for the direction parallel with element sides, and $\gamma=\gamma^{max}$, for the direction inclined at 45° . The recommended (and default) value of $\gamma^{max} = 1.5$.

4.6.4 Crack spacing

In heavily reinforced concrete structures, or structures with large finite elements, when many reinforcement bars are crossing each finite element, the crack band approach

described in Section 3.1.3 will provide too conservative results, and the calculated crack widths may be overestimated. This is the consequence of the fact that the crack band approach assumes that the crack spacing is larger than a finite element size. In heavily reinforced structures, or if large finite elements are used, it may occur that the crack spacing will be smaller than finite element size. This is especially true if shell/plate elements are used. In this case, typically large finite elements can be used, and they usually contain significant reinforcement. In these cases, it is useful to provide the crack spacing manually, since otherwise the program will overestimate the cracking and due to that also larger deflections may be calculated.

4.6.5 Two Models of Smeared Cracks

The smeared crack approach for modeling of the cracks. Within the smeared concept, two options are available for crack models: the fixed crack model and the rotated crack model. In both models the crack is formed when the principal stress exceeds the tensile strength. It is assumed that the cracks are uniformly distributed within the material volume. This is reflected in the constitutive model by an introduction of orthotropy.

4.6.5.1 Fixed Crack Model 45

In the fixed crack model (CERVENKA 1985, DARWIN 1974) the crack direction is given by the principal stress direction at the moment of the crack initiation. During further loading, this direction is fixed and represents the material axis of the orthotropy.

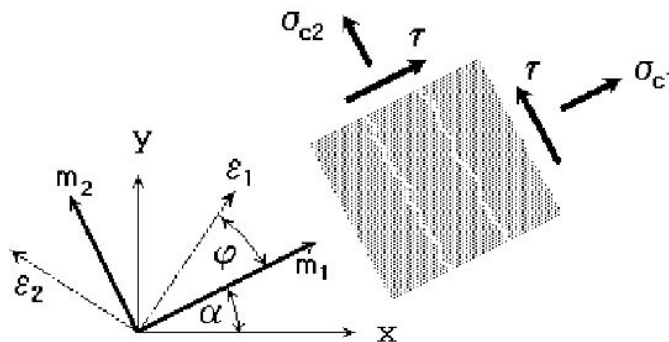


Fig. 4.9 Fixed-crack model, Stress and strain state

The principal stress and strain directions coincide in the uncracked concrete, because of the assumption of isotropy in the concrete component. After cracking, the orthotropy is introduced. The weak material axis m_1 is normal to the crack direction, the strong axis m_2 is parallel with the cracks.

In a general case the principal strain axes ε_1 and ε_2 rotate and need not to coincide with the axes of the orthotropy m_1 and m_2 . This produces a shear stress on the crack face as shown in Fig. 4.9. The stress components σ_{i1} and denote, respectively, the stresses normal and parallel to the crack plane and, due to shear stress, they are not the principal stresses.

2.6.5.2 Rotated Crack Model

In the rotated crack model (VECCHIO 1986, CRISFIELD 1989), the direction of the principal stress coincides with the direction of the principal strain. Thus, no shear strain occurs on the crack plane and only two normal stress components must be defined, as shown in Fig. 4.10.

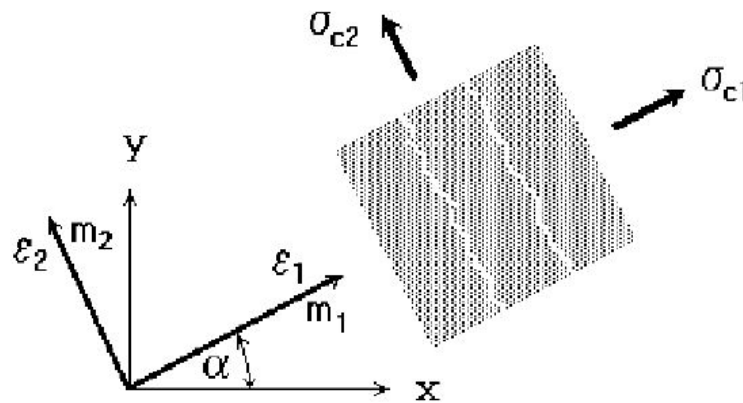


Fig. 4.10 Rotated crack model – Stress and strain state

If the principal strain axes rotate during the loading the direction of the cracks rotate, too. In order to ensure the co-axiality of the principal strain axes with the material axes the tangent shear modulus G_t is calculated according to CRISFIELD 1989 as

$$G_t = \frac{\sigma_{\varepsilon_1} - \sigma_{\varepsilon_2}}{2(\varepsilon_1 - \varepsilon_2)} \quad (4.59)$$

4.7 Reinforcement Stress-Strain Laws

4.7.1 Introduction

Reinforcement can be modeled in two distinct forms: discrete and smeared. Discrete reinforcement is in form of reinforcing bars and is modeled by truss elements. The smeared reinforcement is a component of composite material and can be considered either as a single (only one-constituent) material in the element under consideration or as one of the more such constituents. The former case can be a special mesh element (layer), while the later can be an element with concrete containing one or more reinforcements. In both cases the state of uniaxial stress is

assumed and the same formulation of stress-strain law is used in all types of reinforcement.

4.7.2 Multi-line Law

The multi-linear law consists of four lines as shown in Fig. 4.11. This law allows modeling all four stages of steel behavior: elastic state, yield plateau, hardening and fracture. The multi-line is defined by four points, which can be specified by input.

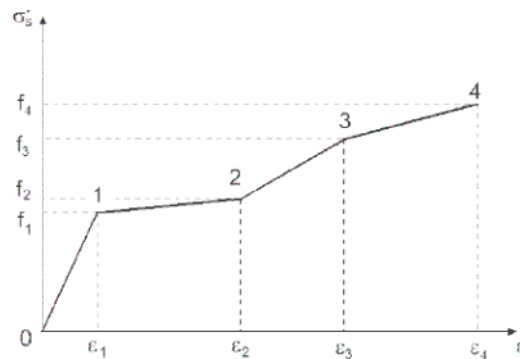


Fig. 4.11 The multi-linear stress-strain law for reinforcement

The above described stress-strain laws can be used for the discrete as well as the smeared reinforcement.

References

- [1] Vladimir Cervenka, Libor Jendele and Jan Cervenka, 2009, "Atena Theory"
- [2] Fariborz Barzegar, Srinivas Maddipudi, "Generating Reinforcement in FE Modeling of Concrete Structures", Journal of Structural Engineering, Vol. 120, No. 5, May, 1994, ISSN 0733-9445/94/0005-1656, Technical note No.5592.
- [3] Alaa E. Elwi, Terry M. Hurdey "Finite Element Model for Curved Embedded Reinforcement", Journal of Engineering Mechanics, Vol.115, No. 4, April 1989, ISSN 0733-9399/89/0004-0740, Paper No. 23331.
- [4] Libor Jendele, Jan Cervenka, "Geometrically Nonlinear Flexibility-Based Frame Finite Element", Computer and structures, 87(2009) 970-980.
- [5] Ansgar Neuerhofer, Filip C. Filippou "On the solution of multi-point constraints – Application to FE analysis of reinforced concrete structures", Journal of Structural Engineering, June 1998,704-711.
- [6] Ansgar Neuerhofer, Filip C. Filippou "Evaluation of Nonlinear Frame Finite-Element Models", Journal of Structural Engineering, June 1997,958-966.

[7] Enricho Spacone, Vincenzo Ciapi and Filip C. Filippou "A Beam Element for Seismic Damage Analysis", Report No. UCB/EERC-92/07, Earthquake Engineering Research Center, College of Engineering, University of California, Berkeley, August 1992.

[8] Giorgio Monti, Enricho Spacone and Filip C. Filippou "A Beam Element for Seismic Damage Analysis", Report No. UCB/EERC-93/08, Earthquake Engineering Research Center, College of Engineering, University of California, Berkeley, December 1993. B.4.

5. Fragility analysis and Risk assessment

5.1 Introduction

Over the last decades the risk management of structural systems have gained the attention of various economic and technical subjects in modern society. The optimal allocation of the public resources for a sustainable economy entails the need of rational tools for estimating the consequences of natural hazardous events on the built environment. The risk management addresses this claim indicating the way for optimal choices. Thus, the main purpose of the risk management process is to choose among different options relying on technical and economic considerations. Risk assessment and decision analysis are the main steps of the risk management concept. It is therefore essential to establish a reliable procedure for assessing the seismic risk of the structural systems. Seismic fragility analysis, which provides a measure of the safety margin of the structural system above specified hazard levels, is considered as the core of the risk assessment.

A number of methodologies for performing fragility analysis have been proposed in the past which have been used for assessing the behaviour of structural systems. Kennedy et al. [1] presented a methodology for determining the probability of earthquake induced radioactive releases as a result of core melt. Kircher et al. [2] described building damage functions that were developed for the FEMA/NIBS earthquake loss estimation methodology [3]. Shinozuka et al. [4] presented a statistical analysis procedure of structural fragility curves. The significance of inherent randomness and modelling uncertainty in forecasting the building performance was examined by Ellingwood [5] through fragility assessment of a steel frame. The importance of fragility analysis in various stages of risk assessment, loss estimation, and decision making in consequence based engineering to achieve the desirable long-term objective in reduction of loss and consequence with the most efficient intervention measures was indicated in [6]. A procedure to account for the uncertainty in the characteristics of future ground motions during seismic response assessment was presented in the work by Aslani and Mirand [7]. Fragility functions were developed in [8] to identify the method of repair required for older reinforced concrete beam-column joints damaged due to earthquake loading. A methodology for the risk assessment of reinforced concrete and unreinforced masonry structures was presented in [9]. Jeong and Elnashai [10] presented an approach where a set of fragility relationships with known reliability is derived based on the fundamental response quantities of stiffness, strength and ductility. A set of procedures for creating fragility functions from various kinds of data was introduced in [11]. In the work by

Shinozuka et al. [12] bridge fragility curves are developed in order to determine the effect earthquakes have on the performance of transportation network systems.

The majority of the reinforced concrete (RC) buildings are constructed with masonry infill walls. However, the combination of the masonry infills with the framed structure is most often neglected during the design procedure, assuming that the contribution on the structural performance is always positive. Such an assumption may lead to substantial inaccuracy in predicting the lateral stiffness, strength and ductility of the structure. In a number of works [13, 14] has been studied the effect of weak ground storeys on the seismic performance of RC frames. On the other hand short columns at the ground storey of the structures are prone to brittle shear failure which may result in severe damages or even collapse because of the poor ductility during earthquakes [15, 16].

All modern seismic design procedures are based on the principal that a structure will avoid collapse if it is designed to absorb and dissipate the kinetic energy that is imparted in it during the seismic excitation. Most of the modern seismic codes express the ability of the structure to absorb energy through inelastic deformation using the behaviour factor. The capacity of a structure to resist seismic actions in the nonlinear range generally permits their design for seismic loads smaller than those corresponding to a linear elastic response. The seismic loads are reduced using the behaviour factor. The numerical confirmation of the behavior factor became a subject of research work during the past decade [17,18] in order to check the validity of design theory assumptions and to make structural performance more predictable from engineering point of view.

The main objective of this study is to determine the effect of Finite Element simulation on fragility analysis of Reinforced Concrete structures. Therefore, two types of FE simulation are used (three-dimensional solid FE with embedded reinforcement and beam FE) on two types of structures, in order to be compared with reference to the limit-state fragilities developed in four drift based limit states. Finally mid annual frequency of exceedence was calculated for each fragility curve.

5.2 Risk Definition

The exact meaning of the word risk is often difficult and tricky to explain in a simple way. In broad sense, risk is related to an unwanted event that can be seen as a dangerous one. According to this general definition, any event or activity may or may not be risky. However, this simple definition cannot be applied to actual situations because a dangerous event cannot be excluded altogether. There is always a margin of uncertainty and then the definition of risk must be formulated in

probabilistic terms. In the last decades some definitions of risk have been given by several researchers. Together with the risk definition, one must provide the definition of other terms usually involved in risk analysis. Namely: the vulnerability, the natural hazard, the exposure. Following the definitions of UNESCO / UNDRO (1982) (Alexander, 2003) it can be said that:

- *Natural hazard (H)* is the probability of occurrence within a specified period of time and within a given area of a potentially damaging phenomenon;
- *Vulnerability (V)* is the degree of loss to a given element or a group of elements at risk resulting from the occurrence of a hazardous phenomenon of a given magnitude. It is expressed on a scale from 0 (no damage) to 1 (total loss);
- *Specific Risk (R_s)* is the expected degree of loss due to a hazardous phenomenon. It may be expressed by the convolution of *Natural Hazard* times *Vulnerability* ;
- *Elements at risk (E)* (Exposure or Exposition) is the population, properties, economic activities, including public services, etc., at risk in a given area;
- *Total risk (R_t)* is the expected number of lives lost and persons injured, and amount of damage to property, or disruption of the economic activity caused by a particular hazardous phenomenon. In other words is the convolution of specific risk (R_s) and elements at risk (E).

Other broad definitions of risk have been proposed, such as the definition quoted by Rackwitz et al. (2005): "The risk is the chance of an adverse outcome to human health, the quality of life, or the quality of the environment". The definitions reported above can be specified and modified in order to fit them to a specific field, such as Civil Engineering. In this field the risk is usually associated with physical damage of structures or facilities. Following this concept, the risk could be defined as the "absolute probability of a negative consequence (e.g. damage or collapse) due to a potentially dangerous event" (Augusti et al., 2001). This probability is the "convolution integral" of three terms, namely vulnerability, exposure and site hazard. The reliability R is defined as the complement of risk ($R = 1 - \text{risk}$). The *site hazard* is usually identified through an intensity measure. A probability of occurrence in a given time span is associated with each intensity measure. This relation is known as the hazard curve and depends on the site under investigation or simply on the place where the structure has been built. In a specific site there will be different hazard curves, one (or more than one) for each natural event (e.g. earthquake, wind storm, flood, fire, etc.). The *exposure* is defined as the probability of the presence of

vulnerable facilities in the site. Typically, the increase of population and economic activities in some areas usually causes an increase of exposition. The *vulnerability* is the probability of attaining or exceeding a damage level conditioned to an event of given intensity measure. Consequences of damage (e.g. losses) are usually measured either in economic term (direct or indirect) or in term of casualties that is losses of human life and injuries. Then the risk can be seen as a probabilistic measure of economic and/or human life losses and injured. This aspect of risk estimation, namely its economic interpretation, is usually used in connection to both decision making theory and insurance.

5.3 Risk assessment

From the point of view of the reliability theory and structural engineering (Melchers, 1987), the risk is defined as the probability of "structural failure" (the unwanted event) both from violation of predefined limit states (e.g. collapse, damage or serviceability) and from other causes. At this point a question arises: "How the probability of structural failure may be assessed?" Generally, the process of probabilistic assessment of structural failure involves many random variables, such as resistance, action, material behaviour, structural response, dimensions of structural elements, etc. These variables are required for characterizing the behaviour of a structure, while they are called as "basic" variables or random variables. The basic variables are usually defined by the mean of their probability distribution and are assumed to be known or given by experimental test or observations. If \mathbf{x} is the vector of the random variables of the problem, $g(\mathbf{x})$ represents the limit state equation and $f_x(\mathbf{x})$ is the joint probability density function of the random variables, the probability of exceeding a specified limit state can be evaluated by using the convolution integral of $f_x(\mathbf{x})$ over the failure domain represented by the condition $g(\mathbf{x}) < 0$ (Melchers, 1987):

$$P_f = P[G(\mathbf{x}) \geq 0] = \int \dots \int_{G(\mathbf{x}) \geq 0} f_x(\mathbf{x}) d\mathbf{x} \quad (5.1)$$

In general, the random variables \mathbf{x} are not independent. Conversely, if they are independent the joint probability density function can be expressed as the product of each probability density function for the random variable x_i $i=1,2,\dots,m$, where m is the number of random variables (Elishakoff, 1999). Besides the numerical difficulty in carrying out the convolution integral, some other problems arise when one wants to derive the probability of structural failure. In particular, the aspects related to human factor, negligence, poor workmanship, neglected load, lack of knowledge about the structural behaviour etc. should be taken into account during the risk assessment process. Furthermore, some causes of failure cannot be foreseen as being "unimaginable" (for instance an event of big magnitude never recorded before); this

increases the level of uncertainty in estimating the risk. As far as the computational aspects are concerned, it can be said that many techniques for evaluating the integral of Eq. (5.1) have been proposed (Melchers, 1987). These techniques are usually based on simplification either for the statistical distributions of each random variable or for the expression of the limit state equation. A typical simplification is to assume that the probability distribution of each random variable is represented by its mean and standard deviation. This corresponds to assume a normal distribution for each random variable involved in the convolution integral. The second simplification is to assume that the limit state function can be approximated by a linear half-space. These are the ingredients for the so-called first-order reliability-method, while second-order reliability-method represents an improvement to FORM, in which the hypothesis of variables normally distributed still holds, but the limit state function is approximated by a hyper-paraboloid in the random variables space. So far the probability of failure of a structure has been tackled disregarding both type of action and structural typology. Considering the seismic action only, it may be said that recently a great deal of effort has been devoted in order to provide a tool of structural design based on the reliability theory. PBEE (Cornell and Krawinkler, 1999) represents one of these tools.

This modern approach to seismic design is also adopted by some design codes such as Vision 2000, FEMA 237, FEMA 356, ATC-32, ATC-40 and is based on the accomplishment, in probabilistic terms, of a generic performance (e.g. no collapse, life safety, operational, fully operational) at various levels of the seismic action. A review of the performance definitions can be found in ATC-58-2 (2003). In other words, the foundation of PBEE consists of assessing the adequacy of a structure or its design by evaluating, in probabilistic way, a decision variable (DV) (in general a vector of variables) (Cornell and Krawinkler, 2000). The decision variable can assume different meanings, such as the earthquake loss, the exceeding of one or more limit states (e.g. collapse, serviceability). Following the PBEE method, in order to assess the probability of exceeding of DV ($\lambda(DV)$) some intermediate variables must be introduced; namely EDP and IM. The methodology of PBEE is illustrated in Figure 5.1, where D represents the location and design features of the structure. In Figure 5.1 $p(x|y)$ refers to the probability density of x conditioned to y, and $g(x)$ refers to the occurrence rate of x (that is the negative first derivative of the frequency with which x is exceeded).

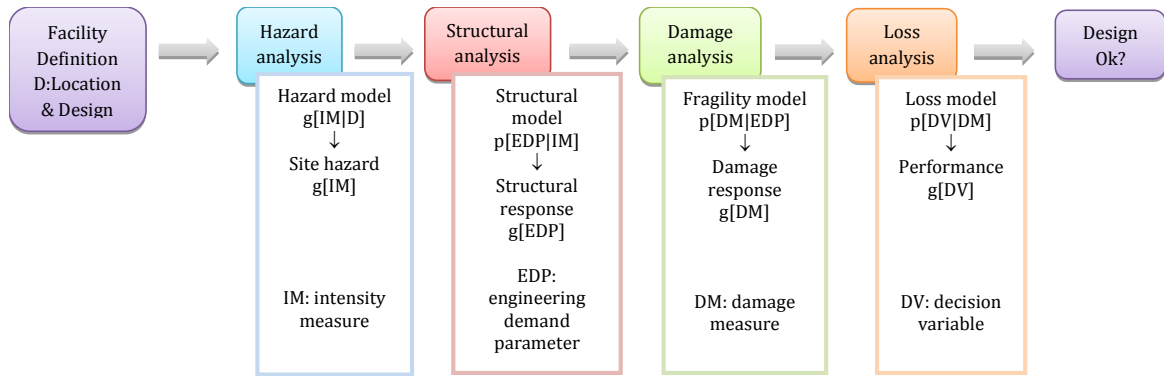


Fig. 5.1 PEER analysis framework, adapted from Porter (2003)

The mathematical meaning of Fig. 5.1 is reported in the following expression that stems from the application of the total probability theorem (Porter, 2003).

$$v(DV | D) = \int \int \int p[DV | DM, D] \cdot p[DV | EDP, D] \cdot p[EDP | IM, D] \cdot g[IM | D] \cdot dDM \cdot dEDP \cdot dIM \quad (5.2)$$

As can be seen in Fig. 5.1, the assessment of $\lambda(DV | D)$ can be accomplished through four analysis steps:

- *Hazard analysis.* It is performed considering the seismic site (nearby faults, their magnitude-frequency recurrence rates, mechanism, site distance, site conditions etc.) and evaluating the seismic hazard at the facility location taking into account all structural features (denoted by the design D). This analysis yields a hazard curve which gives the annual frequency with which the seismic action, described by the IM is exceeded. Various IMs have been studied (Giovenale, 2003) with the aim of selecting one of them (or more than one) as more representative of the site hazard. Summarizing, the Hazard analysis provides an answer to the following question: How likely is an event of intensity IM to happen, for this location?
- *Structural Analysis.* Structural analysis is needed for estimating the uncertain structural response, measured as a vector of EDP conditioned on a seismic IM and design (D), $p[EDP | IM, D]$. A review of the most important EDP, for both structural framing system and non-structural components, can be found in ATC-58-2 (task 2.2) (2004) and ATC-58-2 (task 2.3) (2004). EDP can contain indices related to hysteretic response of structural elements, local or global deformations, maximum floor accelerations and so on. Therefore the structural analysis is usually a nonlinear time-history analysis carried out by using either deterministic finite element models or finite element models with uncertain properties. In short, the question which summarizes the structural analysis step is: What will be the

engineering demands (force, deformation, etc.) to which this facility will be subjected?

- *Damage Analysis*. It is also known as fragility analysis. In this step the results of structural analysis (EDP) are used as input for computing the probability of different levels of physical damage conditioned on structural response and design, $p[DM | EDP, D]$. Thus fragility functions give the probability of various levels of damage for individual beams, columns, non-structural components as functions of various EDP. In other words, what will be the physical damage this facility will experience?
- *Loss Analysis*. It is the last step and consists of determining the performance, represented by the decision variable DV , conditioned on damage and design terms $p[DV | DM, D]$. Decision variables measure the seismic performance of the facility in terms of the main interest of stakeholders. This latter can be both a private owner and a public administrator, so the performance can be measured in terms of money, death, down time, etc. The final step provides an answer to the following question: What will be the loss (economic, casualty, etc.) this facility will experience?

5.4 Calculation of fragility curves

5.4.1 Hazus software

5.4.1.1 Scope and Background

The FEMA/NIBS earthquake loss estimation methodology, commonly known as *HAZUS*, is a complex collection of components that work together to estimate casualties, loss of function and economic impacts on a region due to a scenario earthquake. The methodology is documented in the *HAZUS-MH Technical Manual*. One of the main components of the methodology estimates the probability of various states of structural and nonstructural damage to buildings. Damage state probabilities are used by other components of the methodology to estimate various types of building-related loss. Typically, buildings are grouped by model building type and evaluated on a census tract basis.

Currently, *HAZUS* includes building damage functions for 36 model building types (and for various combinations of seismic design level and performance). Each model building type represents a "generic" group of buildings that share a common type of construction and a common seismic design level.

Damage and loss functions for generic building types are considered to be reliable predictors of earthquake effects for large groups of buildings that include both above median and below median cases. They may not, however, be very good predictors for a specific building or a particular type of building that is known to have a weakness or earthquake vulnerability. Although the theory is applicable to an individual building, buildingspecific damage and loss functions are not provided and would need to be developed by the user. The complexity of the methods and underlying seismological and engineering phenomena makes development of building-specific functions challenging unless the user is an engineer experienced in nonlinear seismic analysis (and seldom necessary for regional loss estimation studies). For mitigation purposes, it is desirable that users be able to create building-specific damage and loss functions that could be used to assess losses for an individual building (or group of similar buildings), both in their existing condition and after some amount of seismic rehabilitation.

FEMA/NIBS projects in the area of earthquake hazard mitigation also include the Building Seismic Safety Council's (BSSC's) development of the *NEHRP Guidelines for Seismic Rehabilitation of Buildings* [FEMA, 1997], referred to simply as the *NEHRP Guidelines*. Like *HAZUS*, the *NEHRP Guidelines* represent a major, multi-year effort. Also like *HAZUS*, the *NEHRP Guidelines* use similar earth science theory and engineering techniques. For the first time, earthquake loss estimation and building seismic analysis are based on common concepts. For example, both the FEMA/NIBS methodology and the *NEHRP Guidelines* (1) use the same characterization of ground shaking (i.e., response spectra, as defined by the USGS maps/theory) and (2) use the same nonlinear (pushover) characterization of building response. The similarity of these fundamental concepts permits interfacing the methods of the *NEHRP Guidelines* with those of *HAZUS* for development of building-specific damage and loss models.

5.4.1.2 Purpose and Approach

The primary purpose of the AEBM is to support mitigation efforts by providing building-specific loss estimation tools for use by experienced seismic/structural engineers. To produce accurate results, the engineer must be capable of carrying out a relatively sophisticated pushover analysis as described below. While the expertise and required inputs may seem challenging, buildingspecific methods are intended for use by those experts who have the requisite skills and desire to go beyond the default methods and data of the more user-friendly "Level 1" or "Level 2" procedures of *HAZUS*.

The underlying approach of AEBM procedures is a combination of the nonlinear static

(pushover) analysis methods of the *NEHRP Guidelines* (and other sources, namely the *ATC-40* document: *Seismic Evaluation and Retrofit of Concrete Buildings*, CSSC, 1996) with HAZUS loss estimation methods. Seismic/structural engineers having performed a detailed pushover analysis of a specific building are expected to have a much better understanding of the building's potential failure modes, overall response characteristics, structural and nonstructural system performance, and the cost and time required to repair damaged components. The *NEHRP Guidelines* provide a logical and appropriate starting point for seismic evaluation of existing buildings and provide state-of-the-art techniques, such as pushover analysis. The *NEHRP Guidelines* also provide limit state criteria for elements and components of buildings that are useful to engineers for determining building-specific damage states. Detailed investigation of a specific building should also provide other important loss-related information. For example, building owners would be expected to provide much more reliable estimates of total replacement cost (value) of the building, the extent and value of contents or inventory, and number of building occupants during different times of the day. All these are critical data required for reliable estimates of earthquake losses.

5.4.2 Calculation method of fragility curves

5.4.2.1 Introduction

Various methods on calculation of fragility curves have been internationally proposed, either experimental or analytical. Variations of the analytical methods concern:

- The analysis method (non linear static and non linear dynamic)
- The seismic parameter in regard of which the fragility curves are calculated (ground acceleration, PGA, spectral displacement S_d or acceleration S_a)
- The means of determining the cumulative distribution function that describes the fragility curves for each damage state

The following methodology is similar with the one of HAZUS software.

Fragility analysis steps

- Simulation of the structure
- Non-linear static pushover
- Capacity curves
- Formation of Acceleration Displacement Response Spectrum (ADRS)
- Capacity spectrum method / Estimation of performance point

- Calculation of log-normal cumulative probability density equation
- Formation of fragility curves for four damage limit states

Based on the described methodology, the Fragility curve is a probabilistic distribution, given by the following log-normal cumulative probability density equation:

$$F(D \geq DI_i | S) = \Phi\left[\frac{1}{\beta_{ds}} \cdot \ln\left(\frac{S}{S_{mi}}\right)\right] \quad (5.3)$$

Where Φ is the standard log-normal cumulative distribution

S is the spectral acceleration amplitude (for a period of $T = 1$ sec)

S_{mi} is the median (or expected value) spectral acceleration necessary to cause the i^{th} damage state to occur

β_{ds} is the normalized standard deviation which incorporates aspects of uncertainty and randomness for both capacity and demand

Only S_{mi} and β_{ds} parameters are needed to define a fragility curve.

5.4.2.2 Damage limit states

The choice of damage scale and measure is fundamental to the fragility curve development. In the case of empirical curves it is essential that the damage scale used is clearly defined in terms of the damage expected in the structural and the non-structural elements of buildings with different lateral load resisting systems. Also, in order to use the fragility curves in a performance-based framework, it is desirable that they provide predictions for at least three damage limit states, corresponding to serviceability, damage control and collapse prevention. In order to define a limit state, different types of parameters are used; most of them, though, with lack of reliability. It has been also proved that limit states have been defined more effectively in terms of deformation exceedance rather than load exceedance.

Performance states defined by economic criteria (e.g. Algermissen et al 1978, Miyakoshi et al. 1997) can preclude the curve application to locations other than those considered. There is no simple relationship that can be drawn between damage and monetary loss, and the latter definition of performance may introduce a time dependency if the limit state values used are linked to the financial situation at the location and the time of the curve derivation (Rossetto & Elnasai, 2003).

FEMA/NIBS earthquake loss estimation methodology, commonly known as HAZUS, suggests that damage states are defined separately for structural and nonstructural systems of a building. Damage is described by one of four discrete damage states:

Slight, Moderate, Extensive or Complete, and Collapse as subset of Complete structural damage. Of course, actual building damage varies as a continuous function of earthquake demand. Ranges of damage are used to describe building damage, since it is not practical to have a continuous scale, and damage states provide the user with an understanding of the building's physical condition. Loss functions relate the physical condition of the building to various loss parameters (i.e., direct economic loss, casualties, and loss of function). For example, direct economic loss due to Moderate damage is assumed to correspond to 10% replacement value of structural and nonstructural components, on the average. The four damage states of the FEMA/NIBS methodology are similar to the damage states defined in *Expected Seismic Performance of Buildings* [EERI, 1994], except that damage descriptions vary for each model building type based on the type of structural system and material. Following Table provides structural damage states for W1 buildings (light frame wood) typical of the conventional construction used for single-family homes.





Damage State		Description
	Slight	Small plaster cracks at corners of door and window openings and wall-ceiling intersections; small cracks in masonry chimneys and masonry veneers. Small cracks are assumed to be visible with a maximum width of less than 1/8 inch (cracks wider than 1/8 inch are referred to as "large" cracks).
	Moderate	Large plaster or gypsum-board cracks at corners of door and window openings; small diagonal cracks across shear wall panels exhibited by small cracks in stucco and gypsum wall panels; large cracks in brick chimneys; toppling of tall masonry chimneys.
	Extensive	Large diagonal cracks across shear wall panels or large cracks at plywood joints; permanent lateral movement of floors and roof; toppling of most brick chimneys; cracks in foundations; splitting of wood sill plates and/or slippage of structure over foundations.
	Complete	Structure may have large permanent lateral displacement or be in imminent danger of collapse due to cripple wall failure or failure of the lateral load resisting system; some structures may slip and fall off the foundation; large foundation cracks. Three percent of the total area of buildings with Complete damage is expected to be collapsed, on average.

Table 5.1 Example damage state – Light-frame wood buildings

The maximum interstory drift ratio was found to provide the optimum parameter for describing the global damage observed in reinforced concrete buildings in reviews of existing local and global energy, force and deformation-based structural response parameters. This is due to its ability to detect both soft-storey and ductile modes of failure, and due to its simplicity of evaluation from experimental tests. It is a fact that the roof drift is a useful measure of the overall structural deformation, but it does not reflect the distribution of damage along the height of the structure, and it does not identify weak elements or soft stories. Instead, interstory drift can be directly correlated with damage at a given story level. For existing non-ductile structures and

poorly designed frames such as those with soft story, the maximum interstory drift of the soft story may indicate collapse while the roof drift may still correspond to a lower damage level.

According to HAZUS structures are categorized by their material and height in order to determine the average inter-story drift ratio Δ_{ds} of structural Damage States the maximum interstory drift ratio that corresponds to one of the damage states (Tables 5.2, 5.3).

No.	Label	Description	Height			
			Range		Typical	
			Name	Stories	Stories	Feet
1	W1	Wood, Light Frame ($\leq 5,000$ sq. ft.)		All	1	14
2	W2	Wood, Greater than 5,000 sq. ft.		All	2	24
3	S1L	Steel Moment Frame	Low-Rise	1-3	2	24
4	S1M		Mid-Rise	4-7	5	60
5	S1H		High-Rise	8+	13	156
6	S2L	Steel Braced Frame	Low-Rise	1-3	2	24
7	S2M		Mid-Rise	4-7	5	60
8	S2H		High-Rise	8+	13	156
9	S3	Steel Light Frame		All	1	15
10	S4L	Steel Frame with Cast-in-Place Concrete Shear Walls	Low-Rise	1-3	2	24
11	S4M		Mid-Rise	4-7	5	60
12	S4H		High-Rise	8+	13	156
13	S5L	Steel Frame with Unreinforced Masonry Infill Walls	Low-Rise	1-3	2	24
14	S5M		Mid-Rise	4-7	5	60
15	S5H		High-Rise	8+	13	156
16	C1L	Concrete Moment Frame	Low-Rise	1-3	2	20
17	C1M		Mid-Rise	4-7	5	50
18	C1H		High-Rise	8+	12	120
19	C2L	Concrete Shear Walls	Low-Rise	1-3	2	20
20	C2M		Mid-Rise	4-7	5	50
21	C2H		High-Rise	8+	12	120
22	C3L	Concrete Frame with Unreinforced Masonry Infill Walls	Low-Rise	1-3	2	20
23	C3M		Mid-Rise	4-7	5	50
24	C3H		High-Rise	8+	12	120
25	PC1	Precast Concrete Tilt-Up Walls		All	1	15
26	PC2L	Precast Concrete Frames with Concrete Shear Walls	Low-Rise	1-3	2	20
27	PC2M		Mid-Rise	4-7	5	50
28	PC2H		High-Rise	8+	12	120
29	RM1L	Reinforced Masonry Bearing Walls with Wood or Metal Deck Diaphragms	Low-Rise	1-3	2	20
30	RM1M		Mid-Rise	4+	5	50
31	RM2L	Reinforced Masonry Bearing Walls with Precast Concrete Diaphragms	Low-Rise	1-3	2	20
32	RM2M		Mid-Rise	4-7	5	50
33	RM2H		High-Rise	8+	12	120
34	URML	Unreinforced Masonry Bearing Walls	Low-Rise	1-2	1	15
35	URM M		Mid-Rise	3+	3	39
36	MH	Mobile Homes		All	1	12

Table 5.2 Model building types of HAZUS

Model Building Type		Structural Damage States			
		Slight	Moderate	Extensive	Complete
Low-Rise Buildings – High-Code Design Level					
W1, W2		0.004	0.012	0.040	0.100
S1		0.006	0.012	0.030	0.080
C1, S2		0.005	0.010	0.030	0.080
C2		0.004	0.010	0.030	0.080
S3, S4, PC1, PC2, RM1, RM2		0.004	0.008	0.024	0.070
Low-Rise Buildings – Moderate-Code Design Level					
W1, W2		0.004	0.010	0.031	0.075
S1		0.006	0.010	0.024	0.060
C1, S2		0.005	0.009	0.023	0.060
C2		0.004	0.008	0.023	0.060
S3, S4, PC1, PC2, RM1, RM2		0.004	0.007	0.019	0.053
Low-Rise (LR) Buildings – Low-Code Design Level					
W1, W2		0.004	0.010	0.031	0.075
S1		0.006	0.010	0.020	0.050
C1, S2		0.005	0.008	0.020	0.050
C2		0.004	0.008	0.020	0.050
S3, S4, PC1, PC2, RM1, RM2		0.004	0.006	0.016	0.044
S5, C3, URM		0.003	0.006	0.015	0.035
Low-Rise (LR) Buildings – Pre-Code Design Level					
W1, W2		0.003	0.008	0.025	0.060
S1		0.005	0.008	0.016	0.040
C1, S2		0.004	0.006	0.016	0.040
C2		0.003	0.006	0.016	0.040
S3, S4, PC1, PC2, RM1, RM2		0.003	0.005	0.013	0.035
S5, C3, URM		0.002	0.005	0.012	0.028
Mid-Rise Buildings ¹					
All	Mid-Rise Building Types	2/3 * LR	2/3 * LR	2/3 * LR	2/3 * LR
High-Rise Buildings ¹					
All	High-Rise Building Types	1/2 * LR	1/2 * LR	1/2 * LR	1/2 * LR

1. Mid-rise and high-rise buildings have damage-state drift values based on low-rise (LR) drift criteria reduced by factors of 2/3 and 1/2, respectively, to account for higher-mode effects and differences between average inter-story drift and individual inter-story drift.

Table 5.3 HAZUS average inter-story drift ration Δ_d s of structural Damage States

5.4.2.3 Lognormal standard deviation β (beta)

Lognormal standard deviation beta values describe the total variability of fragility-curve damage states. Three primary sources contribute to the total variability of any given state, namely, the variability associated with the capacity curve, β_c , the variability associated with the demand spectrum, β_d , and the variability associated with the discrete threshold of each damage state, $\beta_{T,ds}$.

Lognormal standard deviation beta has been calibrated by Pekcan (1998), Dutta and Mander (1998) and Dutta (1999) from a theoretical perspective, and validated by Basöz and Mander (1999) against experimental fragility curves obtained from data

gathered from the 1994 Northridge and 1989 Loma Prieta earthquakes by Basöz and Kiremidjian (1998).

The slope of the fragility curve is controlled by the lognormal standard deviation value (Beta). The smaller the value of Beta, the less variable the damage state, and the steeper the fragility curve. The larger the value of Beta, the more variable the damage state, and the flatter the fragility curve. Fig. 5.2 illustrates this trend for fragility curves that share a common median (i.e., spectral displacement of 5 inches), but have Beta values ranging from 0.4 to 1.2. This range of Beta values approximately covers the range of Beta values that could be used for buildingspecific fragility curves.

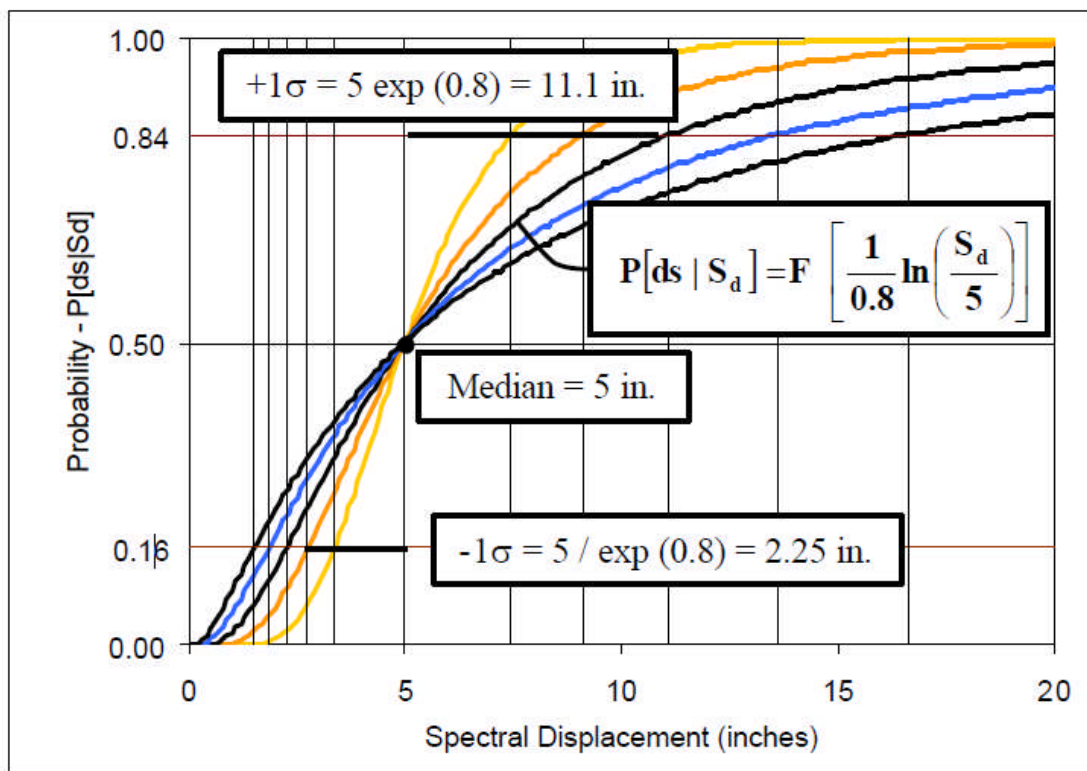


Fig. 5.2 Example Lognormal Fragility Curves (Beta = 0.4, 0.6, 0.8, 1.0, 1.2) and calculation of ± 1σ Spectral Displacement

The following equation describes the calculation of beta (HAZUS 2003):

$$\beta_{ds} = \sqrt{(CONV[\beta_c, \beta_D])^2 + (\beta_{T,ds})^2} \tag{5.4}$$

Where β_{ds} is the lognormal standard deviation parameter that describes the total variability of damage state, d_s ,

β_c is the lognormal standard deviation parameter that describes the variability of the capacity curve

b_D is the lognormal standard deviation parameter that describes the variability of the demand spectrum (values of $b_D = 0.45$ at short periods and $b_D = 0.50$ at long periods were used to develop Tables 5.5 – 5.7)

$b_{T,ds}$ is the lognormal standard deviation parameter that describes the variability of the threshold of damage state, d_s

Since the demand spectrum is dependent on building capacity, a convolution process is required to combine their respective contributions to total variability. This is referred to as "CONV" in Eq. (5.2). The third contributor to total variability, $b_{T,ds}$, is assumed mutually independent of the first two variables and is combined with the results of the CONV process using the squareroot-sum-of-the squares (SRSS) method.

Additional background on the calculation of Damage-State Beta's is provided in the *HAZUS-MH Technical Manual* and the *Earthquake Spectra* paper "Development of Building Damage Functions for Earthquake loss Estimation" [Kircher et al., 1997a]. The variability of the demand spectrum (i.e., variability of ground shaking) is a key parameter in the calculation of damage-state variability. The values of demand variability, $b_D = 0.45$ at short periods and $b_D = 0.50$ at long periods, are the same as those used to calculate the default fragility curves of the *HAZUS-MH Technical Manual*. These values are consistent with the variability (e.g., dispersion factor) of ground shaking attenuation functions used by *HAZUS* to predict response spectra for large-magnitude events in the Western United States (WUS). It may be noted that if there were no variability of demand (response spectrum is known exactly), then Eq. (5.4) would become:

$$\beta_{ds} = \sqrt{\beta_c^2 + \beta_{T,ds}^2} \quad (5.5)$$

This equation provides a lower-bound on the damage-state variability appropriate for use in probabilistic calculations of damage and loss that are based on the integration of the fragility with hazard functions that have already incorporated ground shaking variability in the hazard calculations. Similarly, Eq. (5.5) also provides a lower-bound on damage-state variability for calculation of damage and loss using a response spectrum that is reasonably well known (i.e., response spectrum of recorded ground shaking). Arguably, there would always be some amount variability (uncertainty) in ground shaking demand, b_D , but such can be ignored in the calculation of total damage-state variability, b_{ds} , when substantially less than both capacity curve variability, b_c , and damage-state threshold variability, $b_{T,ds}$.

The convolution process involves a complex numerical calculation that would be very difficult for most users to perform. To avoid this difficulty, sets of pre-calculated values of Damage-State Beta's have been compiled in Tables 5.5 through 5.7 from which users may select appropriate values of variability for the structural system, nonstructural drift-sensitive components and nonstructural acceleration-sensitive components. The Beta values of these tables are a function of the following building characteristics and criteria:

- Building Height Group - Low-Rise Buildings (Table 5.5), Mid-Rise Buildings (Table 5.6) and High-Rise Buildings (Table 5.7)
- Post-Yield Degradation of the Structural System – Minor, Major and Extreme Degradation
- Damage-State Threshold Variability – Small, Moderate or Large Variability
Capacity Curve Variability – Very Small, Small, Moderate or Large Variability

The Beta values of the tables are applicable to all model building types. For example, a low-rise concrete-frame building (C1L) would have the same set of Beta's as a low-rise braced steel frame building (S2L), provided the two buildings have the same amount of capacity curve and damage-state threshold variability, and the same amount of post-yield degradation of the structural system.

Post-yield degradation of the structural system is defined by a Kappa factor, which is an direct measure of the effects of seismic design level and construction quality on the variability of response. Buildings that are seismically designed and/or have superior construction are less likely to degrade during post-yield earthquake shaking, and therefore have more predictable response, than buildings that are not seismically designed and/or have inferior construction.

To select a set of building-specific Damage-State Beta's (i.e., a structural Beta, a nonstructural drift-sensitive Beta and a nonstructural acceleration-sensitive Beta), it must first be determined the building height group that best represents the specific building of interest. The height groups are defined by the same criteria as those used by HAZUS to define generic building types. For example, a 5-story, reinforced concrete building would be classified as a mid-rise building as per the height criteria of Table 5.2.

Tables 5.5 through 5.7 (referred to as the Beta tables) provide recommended sets of Damage-State Beta's for each of the three building height groups, respectively. In

each of these tables, the Beta's are based on 36 possible combinations of capacity curve variability, damage threshold variability and the amount of post-yield degradation expected for the structural system.

Estimation of structural system degradation (minimum or maximum) is made on the basis of Kappa factors suggested by Table 5.4 (HAZUS Section 5.3.3) and the degree of post-yield response expected for the damage state of interest. Kappa factors decrease with increase in response level (and damage). Slight damage corresponds to response between $\frac{1}{2}$ yield and full yield; Moderate damage to response at or just beyond yield; and Extensive and Complete damage correspond to post-yield response for the duration of scenario earthquake shaking. Beta values are given in Tables 5.5 through 5.7 for $k \geq 0.9$ (minor degradation), $k = 0.5$ (major degradation) and $k \leq 0.1$ (extreme degradation) of the structural system; and linear interpolation may be used to establish Beta's for other values of the Kappa factor.

Estimation of the variability of the capacity curve (b_C) and the variability of the threshold of the damage state ($b_{T,ds}$) must be made by users on a judgmental basis (with some guidance provided herein). To assist the user, the Beta tables express capacity curve and damage threshold variability qualitatively (e.g., Small Variability) and in terms of the numerical value used to develop the Beta's in the CONV process. Numerical values of variability (b_C and $b_{T,ds}$) are lognormal standard deviation parameters and may be used, to construct the distribution of capacity or damage threshold that they represent.

The variability of capacity curves and the damage-state thresholds are influenced by:

- Uncertainty in capacity curve properties and the thresholds of damage states
- Building population (i.e., individual building or group of buildings)

Relatively low variability of damage states would be expected for an individual building with well known properties (e.g., complete set of as-built drawings, material test data, etc.) and whose performance and failure modes are known with confidence. The taller the building the greater the variability in damage state due to uncertainty in the prediction of response and damage using pushover analysis. Relatively high variability of damage states would be expected for a group of buildings whose properties are not well known and for which the user has low confidence in the results (of pushover analysis) that represent performance and failure modes of all buildings of the group. The latter case essentially describes the

original development of damage-state fragility curves for generic model building that were based on capacity variability, $b_c = 0.3$, and damagestate threshold variability, $b_{T,ds} = 0.3$ (Structure), $b_{T,ds} = 0.5$ (NSD) and $b_{T,ds} = 0.6$ (NSA). The generic model building types represent large populations of buildings for which properties are not well known.

Design Level and Construction Quality					Degradation (Kappa) Factor					
	Seismic Design Level ¹					At ½ Yield	At Yield	Post-Yield Shaking Duration		
	SHC	HC	MC	LC	PC			Short	Moderate	Long
QC ²	S	S				1.0	1.0	1.0	0.9	0.7
		O	S			1.0	1.0	0.9	0.7	0.5
		I	O	S		1.0	0.9	0.7	0.5	0.3
			I	O	S	1.0	0.7	0.5	0.3	0.1
				I	O	1.0	0.5	0.3	0.1	0.0

1. Seismic Design Level Designation – Special High-Code (SHC), High-Code (HC), Moderate-Code (MC), Low-Code (LC) and Pre-Code (PC)
2. Construction Quality (QC) Designation – Superior (S), Ordinary (O) and Inferior (I)

Table 5.4 Suggested values of the degradation (Kappa) Factor

Building System ²	Post-Yield Degradation of Structural System ³								
	Minor Degradation ($\kappa \geq 0.9$)			Major Degradation ($\kappa = 0.5$)			Extreme Degradation ($\kappa \leq 0.1$)		
	Damage Variability ⁴ ($\beta_{T,ds}$)			Damage Variability ⁴ ($\beta_{T,ds}$)			Damage Variability ⁴ ($\beta_{T,ds}$)		
	Small (0.2)	Mod. (0.4)	Large (0.6)	Small (0.2)	Mod. (0.4)	Large (0.6)	Small (0.2)	Mod. (0.4)	Large (0.6)
Structural Systems with Very Small Capacity Curve Variability ⁵ ($\beta_C = 0.1$)									
Structure	0.70	0.80	0.90	0.85	0.90	1.00	0.95	1.00	1.10
NSD	0.65	0.75	0.90	0.85	0.90	1.00	0.95	1.00	1.10
NSA	0.35	0.50	0.65	0.35	0.50	0.65	0.35	0.50	0.65
Structural Systems with Small Capacity Curve Variability ⁵ ($\beta_C = 0.2$)									
Structure	0.70	0.80	0.90	0.85	0.90	1.00	0.95	1.05	1.15
NSD	0.70	0.75	0.90	0.85	0.90	1.00	0.95	1.00	1.10
NSA	0.35	0.50	0.65	0.35	0.50	0.65	0.35	0.50	0.65
Structural Systems with Moderate Capacity Curve Variability ⁵ ($\beta_C = 0.3$)									
Structure	0.75	0.80	0.95	0.85	0.95	1.05	1.00	1.05	1.15
NSD	0.70	0.80	0.90	0.85	0.95	1.05	1.00	1.05	1.15
NSA	0.35	0.50	0.65	0.35	0.50	0.65	0.35	0.50	0.65
Structural Systems with Large Capacity Curve Variability ⁵ ($\beta_C = 0.4$)									
Structure	0.80	0.85	0.95	0.90	1.00	1.10	1.05	1.10	1.20
NSD	0.75	0.85	0.95	0.90	1.00	1.05	1.00	1.05	1.15
NSA	0.35	0.50	0.65	0.35	0.50	0.65	0.35	0.50	0.65

Table 5.5 Low-rise building fragility Beta's

Building System ²	Post-Yield Degradation of Structural System ³								
	Minor Degradation ($\kappa \geq 0.9$)			Major Degradation ($\kappa = 0.5$)			Extreme Degradation ($\kappa \leq 0.1$)		
	Damage Variability ⁴ ($\beta_{T,ds}$)			Damage Variability ⁴ ($\beta_{T,ds}$)			Damage Variability ⁴ ($\beta_{T,ds}$)		
	Small (0.2)	Mod. (0.4)	Large (0.6)	Small (0.2)	Mod. (0.4)	Large (0.6)	Small (0.2)	Mod. (0.4)	Large (0.6)
Structural Systems with Very Small Capacity Curve Variability ⁵ ($\beta_C = 0.1$)									
Structure	0.60	0.70	0.80	0.70	0.80	0.90	0.85	0.95	1.05
NSD	0.60	0.70	0.80	0.80	0.85	0.95	0.90	1.00	1.10
NSA	0.35	0.50	0.65	0.35	0.50	0.65	0.35	0.50	0.65
Structural Systems with Small Capacity Curve Variability ⁵ ($\beta_C = 0.2$)									
Structure	0.65	0.75	0.85	0.75	0.85	0.95	0.95	1.00	1.10
NSD	0.65	0.70	0.85	0.80	0.85	1.00	0.95	1.00	1.10
NSA	0.35	0.50	0.65	0.35	0.50	0.65	0.35	0.50	0.65
Structural Systems with Moderate Capacity Curve Variability ⁵ ($\beta_C = 0.3$)									
Structure	0.65	0.75	0.85	0.80	0.85	0.95	0.95	1.00	1.10
NSD	0.65	0.75	0.85	0.80	0.90	1.00	0.95	1.05	1.15
NSA	0.35	0.50	0.65	0.35	0.50	0.65	0.35	0.50	0.65
Structural Systems with Large Capacity Curve Variability ⁵ ($\beta_C = 0.4$)									
Structure	0.70	0.75	0.90	0.80	0.90	1.00	1.00	1.05	1.15
NSD	0.70	0.75	0.90	0.85	0.90	1.00	1.00	1.05	1.15
NSA	0.35	0.50	0.65	0.35	0.50	0.65	0.35	0.50	0.65

Table 5.6 Mid-rise building fragility Beta's

Building System ²	Post-Yield Degradation of Structural System ³								
	Minor Degradation ($\kappa \geq 0.9$)			Major Degradation ($\kappa = 0.5$)			Extreme Degradation ($\kappa \leq 0.1$)		
	Damage Variability ⁴ ($\beta_{T,ds}$)			Damage Variability ⁴ ($\beta_{T,ds}$)			Damage Variability ⁴ ($\beta_{T,ds}$)		
	Small (0.2)	Mod. (0.4)	Large (0.6)	Small (0.2)	Mod. (0.4)	Large (0.6)	Small (0.2)	Mod. (0.4)	Large (0.6)
Structural Systems with Very Small Capacity Curve Variability ⁵ ($\beta_C = 0.1$)									
Structure	0.55	0.65	0.80	0.65	0.75	0.85	0.80	0.90	1.00
NSD	0.55	0.65	0.80	0.75	0.80	0.95	0.90	0.95	1.05
NSA	0.35	0.50	0.65	0.35	0.50	0.65	0.35	0.50	0.65
Structural Systems with Small Capacity Curve Variability ⁵ ($\beta_C = 0.2$)									
Structure	0.60	0.65	0.80	0.70	0.80	0.90	0.90	0.95	1.05
NSD	0.60	0.70	0.80	0.75	0.85	0.95	0.95	1.00	1.10
NSA	0.35	0.50	0.65	0.35	0.50	0.65	0.35	0.50	0.65
Structural Systems with Moderate Capacity Curve Variability ⁵ ($\beta_C = 0.3$)									
Structure	0.60	0.70	0.80	0.70	0.80	0.90	0.95	1.00	1.10
NSD	0.60	0.70	0.85	0.80	0.85	0.95	0.95	1.05	1.15
NSA	0.35	0.50	0.65	0.35	0.50	0.65	0.35	0.50	0.65
Structural Systems with Large Capacity Curve Variability ⁵ ($\beta_C = 0.4$)									
Structure	0.60	0.70	0.85	0.75	0.80	0.95	0.95	1.00	1.10
NSD	0.60	0.70	0.85	0.80	0.90	1.00	1.00	1.05	1.15
NSA	0.35	0.50	0.65	0.35	0.50	0.65	0.35	0.50	0.65

Table 5.7 High-rise building fragility Beta's

5.4.3 Calculation of Damage-State Probability

The fragility curves distribute damage among different damage states (for example slight, moderate, extensive and complete recommendation of HAZUS, 2003). For any given value of the response, discrete damage-state probabilities are calculated as the difference of the cumulative probabilities of reaching, or exceeding, successive damage states. The probabilities of a building reaching or exceeding the various damage levels at a given response level sum to 100%.

Fragility curves define boundaries between damage limit states. Therefore, the median value of the limit state of interest defines the threshold of damage, and this state of damage is assumed to exist up to next state of damage. This description is illustrated in Fig. 5.2, which includes an example of the fragility curves for slight, moderate, extensive and complete structural damage. In this illustration, a region between the green and the yellow curves illustrates the probability-response space associated with slight damage. The boundary on the left of this region is defined by

the fragility curve for slight (or greater) structural damage, and the boundary on the right is defined by the fragility curve for moderate (or greater) damage. The probability of slight damage at a given level of demand is calculated as the difference of the probability of slight (or greater) damage less the probability of moderate (or greater) damage – a probability of 0.50 at 3.0 m/sec² of peak ground acceleration in the example shown in Fig. 5.2.

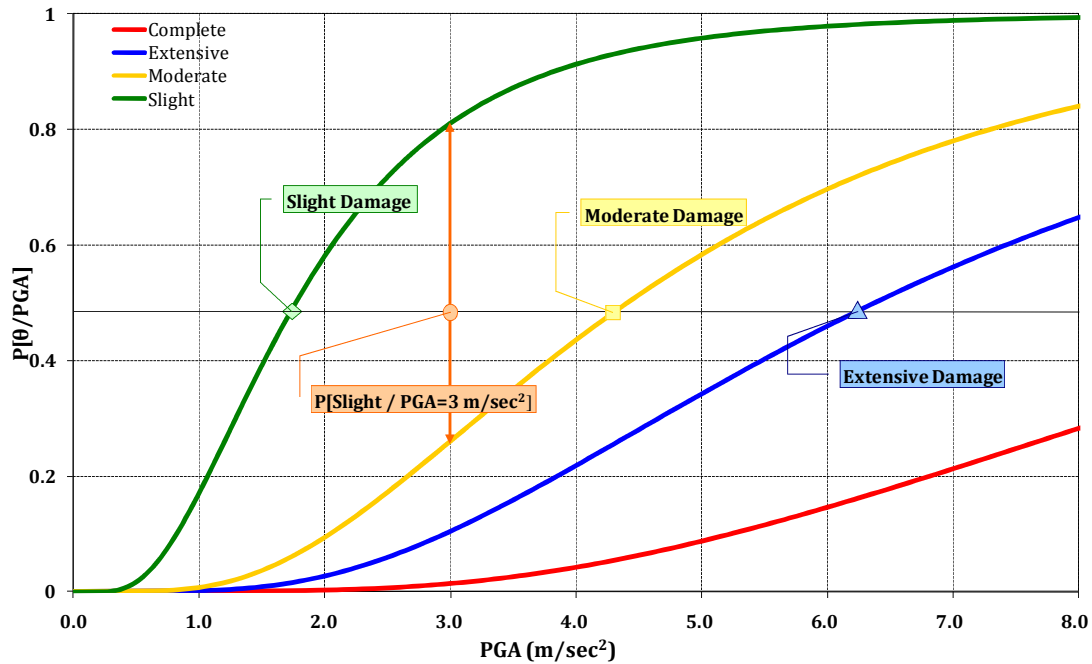


Fig. 5.2 Example of fragility curves - Calculation of damage-state probability

Seismic design procedures

The majority of the seismic design codes belong to the category of the prescriptive building design codes, which include: site selection and development of conceptual, preliminary and final design stages. According to a prescriptive design code the strength of the structure is evaluated at one limit state between life-safety and near collapse using a response spectrum corresponding to one design earthquake [19,20]. In addition, serviceability limit state is checked in order to ensure that the structure will not deflect or vibrate excessively during its functioning. The main principle of new provisions, EAK 2000 [19] and Eurocode 8 [20] included, is to design structural systems based on energy dissipation and on ductility in order to control the inelastic seismic response. Designing a multistory RC building for energy dissipation comprises the following features: (i) fulfillment of the strong column/weak beam rule, (ii) member verification in terms of forces and resistances for the ultimate strength limit state under the design earthquake (with return period of 475 years, probability of exceedance 10% in 50 years), with the elastic spectrum reduced by the behaviour factor, (iii)

damage limitation for the serviceability limit state and (iv) capacity design of beams and columns against shear failure.

According to the Greek national design codes and Eurocodes a number of checks must be considered in order to ensure that the structure will meet the design requirements. All EKOS 2000 [21] or Eurocode 2 [22] checks must be satisfied for the gravity loads using the following load combination

$$S_d = 1.35 \sum_j G_{kj} + 1.50 \sum_i Q_{ki} \quad (3)$$

where "+" implies "to be combined with", the summation symbol " Σ " implies "the combined effect of", G_{kj} denotes the characteristic value "k" of the permanent action j and Q_{ki} refers to the characteristic value "k" of the variable action i . If the above constraints are satisfied, multi-modal response spectrum analysis is performed, according to EAK 2000 [19] and Eurocode 8 [20], and earthquake loading is considered using the following load combination

$$S_d = \sum_j G_{kj} + E_d + \sum_i \psi_{2i} Q_{ki} \quad (4)$$

where E_d is the design value of the seismic action for the two components (longitudinal and transverse) respectively and ψ_{2i} is the combination coefficient for the quasi-permanent action i , here taken equal to 0.30.

References

- [1] Kennedy, R.P., Cornell, C.A., Campbell, R.D., Kaplan, S., Perla, H.F. (1980), "Probabilistic seismic safety study of an existing nuclear power plant," *Nuclear Engineering and Design*; 59(2):315-338.
- [2] Kircher, C.A., Nassar, A.A., Kustu, O., Holmes, W.T. (1997), "Development of building damage functions for earthquake loss estimation," *Earthquake Spectra*; 13(4):663-682.
- [3] FEMA-National Institute of Building Sciences. HAZUS-MH MR1, Multi-hazard Loss Estimation Methodology Earthquake Model, Washington, DC, 2003.
- [4] Shinozuka, M., Feng, M.Q., Lee, J., Naganuma, T. (2000), "Statistical analysis of fragility curves," *Journal of Engineering Mechanics*; 126(12):1224-1231.
- [5] Ellingwood, B.R. (2001), "Earthquake risk assessment of building structures," *Reliability Engineering and System Safety*; 74(3):251-262.
- [6] Wen, Y.K., Ellingwood, B.R. (2005), "The role of fragility assessment in consequence-based engineering," *Earthquake Spectra*; 21(3):861-877.

- [7] Aslani, H., Miranda, E. (2005), "Probability-based seismic response analysis," *Engineering Structures*; 27(8):1151-1163.
- [8] Pagni, C.A., Lowes, L.N. (2006), "Fragility functions for older reinforced concrete beam-column joints," *Earthquake Spectra*; 22(1):215-238.
- [9] Kappos, A.J., Panagopoulos, G., Panagiotopoulos, C., Penelis, G. (2006), "A hybrid method for the vulnerability assessment of R/C and URM buildings," *Bulletin of Earthquake Engineering*; 4(4):391-413.
- [10] Jeong, S.-H., Elnashai, A.S. (2007), "Probabilistic fragility analysis parameterized by fundamental response quantities," *Engineering Structures*; 29(6):1238-1251.
- [11] Porter, K., Kennedy, R., Bachman, R. (2007), "Creating fragility functions for performance-based earthquake engineering," *Earthquake Spectra*; 23(2):471-489.
- [12] Shinozuka, M., Murachi, Y., Dong, X., Zhou, Y., Orlikowski, M.J., (2003), "Effect of seismic retrofit of bridges on transportation networks," *Earthquake Engineering and Engineering Vibration*; 2(2):169-179.
- [13] Lee, H.-S., Woo, S.-W. (2002), "Effect of masonry infills on seismic performance of a 3-storey R/C frame with non-seismic detailing," *Earthquake Engineering and Structural Dynamics*, 31(2): 353-378.
- [14] Negro, P., Verzeletti, G. (1996), "Effect of infills on the global behaviour of R/C frames: Energy considerations from pseudodynamic tests," *Earthquake Engineering and Structural Dynamics*; 25(8): 753-773.
- [15] Li, Z.-X. (2005), "Theory and technology of split reinforced concrete columns," *Engineering Mechanics*, 22: 127-141.
- [16] Guevara, L.T., García, L.E. (2005), "The captive- and short-column effects," *Earthquake Spectra*; 21(1): 141-160.
- [17] Fajfar, P. (1998), "Towards nonlinear methods for the future seismic codes," in Booth, editor, *Seismic Design Practice into the Next Century*, Balkema.
- [18] Mazzolani, F.M., Piluso, V. (1996), *The Theory and Design of Seismic Resistant Steel Frames*, E & FN Spon.
- [19] EAK 2000, National seismic code of Hellas, 2000.
- [20] EN 1998-1:2003. Eurocode 8: Design of Structures for Earthquake Resistance. Part 1: General rules, seismic actions and rules for buildings. Commission of the European Communities, European Committee for Standardization, October 2003.
- [21] EKOS 2000, National code for concrete building structures of Hellas, 2000.
- [22] EN 1992-1-1:2002. Eurocode 2: Design of Concrete Structures. Part 1: General rules and rules for buildings. Commission of the European Communities, European Committee for Standardization, November 2002.
- [23] Dolšek, M., Fajfar, P. (2001), "Soft storey effects in uniformly infilled reinforced concrete frames," *Journal of Earthquake Engineering*; 5(1): 1-12.
- [24] Ghobarah, A., Saatcioglu, M., Nistor, I. (2006), "The impact of the 26 December 2004 earthquake and tsunami on structures and infrastructure," *Engineering Structures*; 28(2): 312-326.

- [25] Chao, H.H., Yungting, A.T., Ruo, Y.H., (2006), "Nonlinear pushover analysis of infilled concrete frames," *Earthquake Engineering and Engineering Vibration*, 5(2):245-255.
- [26] Mitchell, D., DeVall, R.H., Kobayashi, K., Tinawi, R., Tso, W.K. (1996), "Damage to concrete structures due to the January 17, 1995, Hyogo-ken Nanbu (Kobe) earthquake," *Canadian Journal of Civil Engineering*; 23(3): 757-770.
- [27] Somerville, P., Collins, N. (2002), "Ground motion time histories for the Humboldt bay bridge," Pasadena, CA, URS Corporation.
- [28] Papazachos, B.C., Papaioannou, Ch.A., Theodulidis N.P. (1993), "Regionalization of seismic hazard in Greece based on seismic sources," *Natural Hazards*; 8(1): 1-18.
- [29] Chintanapakdee, C., Chopra, A.K. (2003), "Evaluation of modal pushover analysis using generic frames," *Earthquake Engineering and Structural Dynamics*; 32(3): 417-442.
- [30] McKenna, F., Fenves, G.L. (2001), *The OpenSees Command Language Manual - Version 1.2*, Pacific Earthquake Engineering Research Centre, University of California, Berkeley.
- [31] Lagaros, N.D. (2007), "Life-cycle cost analysis of design practices for RC framed structures," *Bulletin of Earthquake Engineering*; 5(3):425-442.
- [32] Perera, R., Gomez, S., Alarcon E. (2004), "Experimental and analytical study of masonry infill reinforced concrete frames retrofitted with steel braces," *Journal of Structural Engineering*; 130(12): 2032-2039.
- [33] Ghobarah, A., (2004), "On drift limits associated with different damage levels," International Workshop on Performance-Based Seismic Design, June 28-July 1.
- [34] Lagaros, N.D., Fotis, A.D., Krikos, S.A. (2006), "Assessment of seismic design procedures based on the total cost," *Earthquake Engineering and Structural Dynamics*; 35(11):1381-1401.
- [35] Lagaros, N.D., Probabilistic Fragility Analysis: A tool for assessing design rules or RC buildings

6. Numerical investigation

6.1 Introduction

This chapter describes the non-linear static and fragility analysis of two types of structures:

- Two-dimensional two-story frame structure (Fig. 6.1)
- Three-dimensional two-story frame structure (Fig. 6.2)

The analyses were conducted using two different types of Finite Element simulation

- Beam-Column FE simulation method (OpenSees software)
- 3D solid FE simulation with embedded reinforcement (ATENA 3D software)

Analyses results were intended to perform fragility analysis in order to decide the effect of different FE simulation methods on the fragility curves figure.

6.2 Methodology

6.2.1 Definition of the structure

Fig. 6.1 and Fig. 6.2 demonstrate the form of the two frame structures.

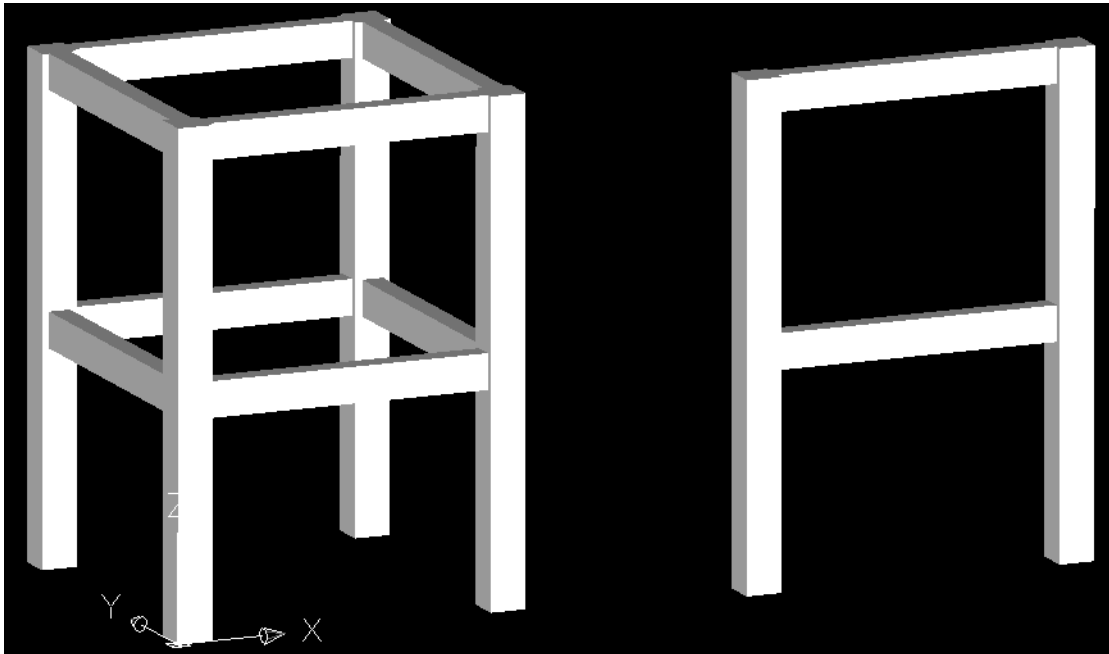


Fig. 6.1, Fig 6.2 3-Dimensional, 2-Dimensional frame structures

6.2.2 Simulation

Beam-Column FE simulation

This beam-column FE simulation was conducted using OpenSees software. Frame structure input values referred in the longitudinal axis of symmetry of each entity (beams and columns). Area dimensions were afterwards assigned to the linear elements. Rigid offsets were used to simulate the beam-column unity. Finally, the loading was applied including dead forces, external vertical loads (in correspondence with codes of practice as well as prescribed deformation in order for the displacement control Pushover analysis to be performed.

3D solid FE simulation with embedded reinforcement

Concrete material properties were assigned to macro-elements with the given dimensions as well as steel material properties to reinforcement bars lying in advised positions. External loading was applied on top o the columns in both stories.

Modal analyses performed for both types of structures.

6.2.3 Pushover analysis

Displacement control pushover analysis were performed using prescribed deformation on top corners of the frame structures along x axis for 2-dimensional frames and along x and y axes for 3-dimensional frames following the x+0.3y and 0.3x+y pattern. Thus, six analyses occurred, two for 2-dimensional frames with two simulations, two for 3-dimensional frames with two simulations concerning x+0.3y prescribed deformation and two for 3-dimensional frames with two simulations concerning 0.3x+y prescribed deformation.

Analyses results include total base force and interstory drift percentage

$$\Delta = \frac{\delta_i - \delta_j}{H_{ij}} (\%)$$

Were i, j the number of story, δ_i , δ_j the relative displacement of two sequential stories and H_{ij} the distance between the stories.

6.2.4 Fragility curves

The methodology describe in the current paragraph was followed after each one of the six analyses using the results that occurred.

N2 method was used for the calculation of displacements. The method demanded the transformation of the capacity curve (force-deformation) in ADRS spectrum of equivalent single-degree of freedom (SDOF) structure, in terms of S_a , S_d .

$$S_{\alpha} = \frac{V}{\alpha \cdot m_{tot}}, \quad S_d = \frac{\Delta}{\Gamma \cdot \phi_{top}}$$

Where, m_{tot} total mass of the 2 story structure, V total base force, Δ deformation of the top, α total mass of the structure percentage participating in the dynamic response and Γ participation coefficient.

$$\alpha = \frac{[\sum m_i \cdot \phi_i]^2}{m_{tot} \cdot \sum m_i \cdot \phi_i^2} = \frac{\Gamma \cdot \sum m_i \cdot \phi_i}{m_{tot}}$$

$$\Gamma = \frac{\sum m_i \cdot \phi_i}{\sum m_i \cdot \phi_i^2} \quad m^* = \sum m_i \cdot \phi_i$$

m^* is the mass of the equivalent system

ϕ_i mode for i -story

The stiffness of the equivalent SDOF structure and the original structure remains the same as long as both forces and displacements follow the same transformation law. Equivalent SDOF structure depends on the distribution of the load through the height of the structure that is taken into account during the calculation of the capacity curve. Triangular distribution was used.

The same transformation equations were used to transform the elastic response spectrum in S_a - S_d values. The new spectrum was scaled in order to define several intersection points with the bilinear ADRS spectrum of the structure. PGA values were noted in so to be used in the fragility curve equation.

$$F(D \geq DI_i | S) = \Phi\left[\frac{1}{\beta_{ds}} \cdot \ln\left(\frac{S}{S_{m_i}}\right)\right]$$

As described in 5.4.2.2 and according to HAZUS tables, interstory limit **damage state drift percentages** for low rise buildings and moderate code-design (Table 5.3) are 0.5%, 0.9%, 2.3%, 6.0% for slight, moderate, extensive and complete damage states respectively. Intersection points were used with linear interpolation, in defining the **PGA** value that corresponds with the limit state drift percentages referred above.

Lognormal standard deviation β was calculated according to paragraph 5.4.2.3 using the HAZUS table (Table 5.5) for low-rise buildings. β_{ds} estimated as 0.76 for both types of structures.

With the gathered results (V base, D roof, Drift percentages of each story, $S_{mi} = \text{PGA}$, β_{ds}) fragility analysis was elaborated taking into account the values that indicated disfavor in the behavior of the structure (comparing structures of the same type).

6.2.5 Risk assessment

The calculated fragility curves (all referring to the range between first and second story beams) were combined with Hazard curves of a region through the following equation:

$$v_{\theta > y} = \int P(\theta_{\max} \geq y / IM = x) |d\lambda_{IM}(x)|$$

Where v is the mean annual frequency of exceedence of the limit state into which the structure is subjected

$IM = \text{PGA}$

The Hazard curve taken into account is of the following diagram:

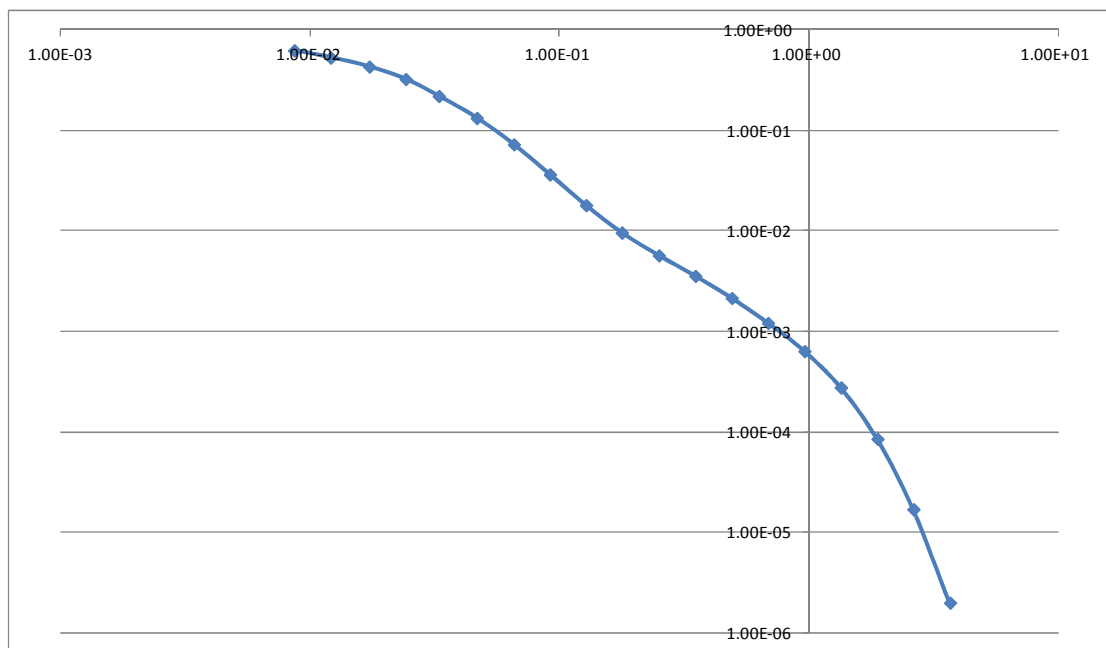


Fig. 7.1 Hazard curve used

The integral calculation was performed using Matlab software, the results of which are presented in the tables in 6.3.3.

6.3 Fragility analysis results

6.3.1 Two-dimensional frame structures

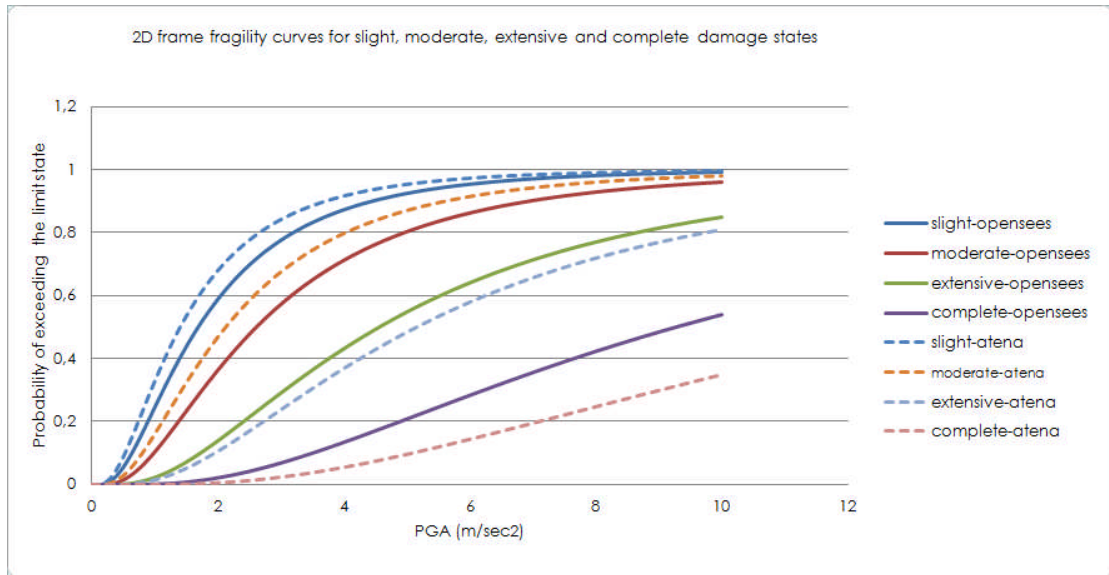


Fig. 7.2 fragility curves of 2-dimansional frame structure for Beam-Column and 3D solid FE simulation methods for slight, moderate, extensive and complete damage states

Beam-Column FE simulation (opensees), 3D solid FE simulation (atena).

6.3.2 Three-dimensional frame structures

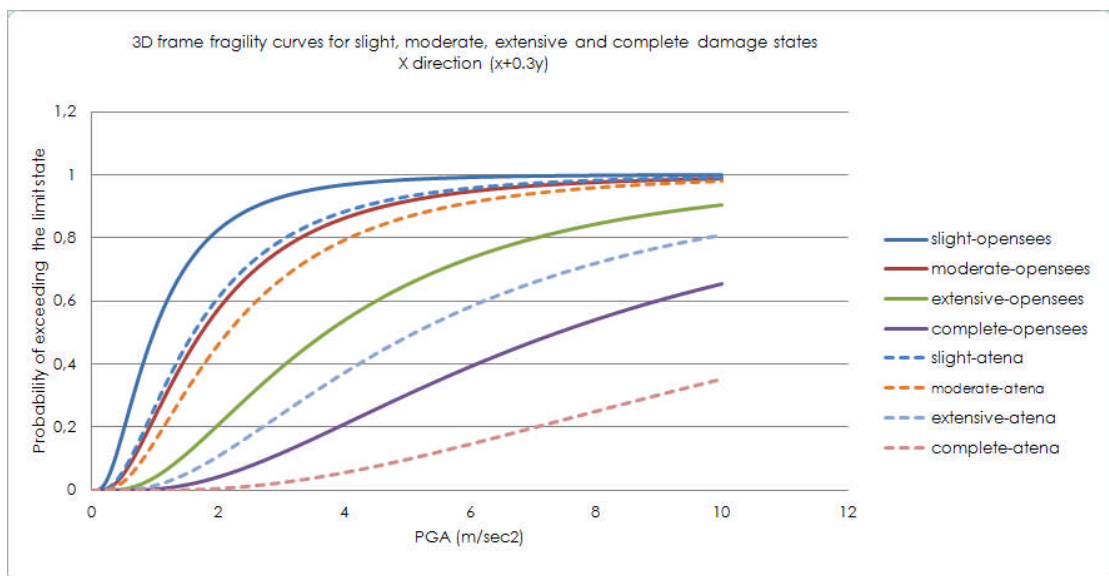


Fig. 7.3 fragility curves of 3-dimansional frame structure for Beam-Column and 3D solid FE simulation methods for slight, moderate, extensive and complete damage states (X direction)

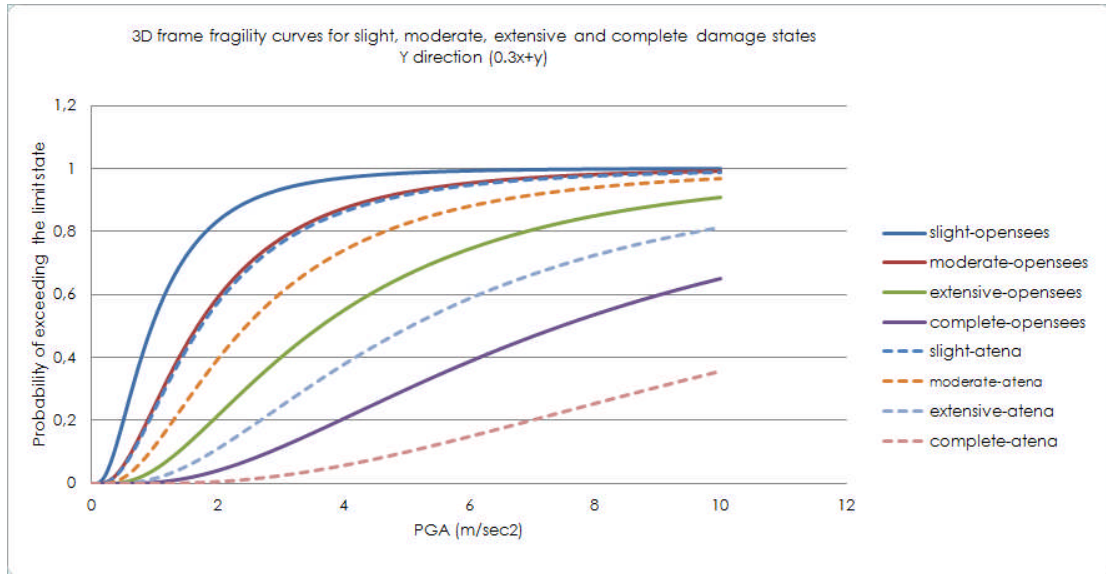


Fig. 7.4 fragility curves of 3-dimensional frame structure for Beam-Column and 3D solid FE simulation methods for slight, moderate, extensive and complete damage states (Y diection)

Beam-Column FE simulation (opensees), 3D solid FE simulation (atena).

6.3.3 Risk analysis results

2-Dimensional Structure		
drift %	OpenSees	ATENA 3D
0,5	7,02E-03	7,27E-03
0,9	1,98E-03	3,05E-03
2,3	2,46E-04	3,30E-04
6,0	3,14E-05	1,32E-05

3-Dimensional Structure OpenSees		
drift %	X dir.	Y dir.
0,5	1,44E-02	1,51E-02
0,9	4,71E-03	5,01E-03
2,3	8,03E-04	8,51E-04
6,0	1,11E-04	1,07E-04

3-Dimensional Structure X dir.		
drift %	OpenSees	ATENA 3D
0,5	1,44E-02	5,46E-03
0,9	4,71E-03	2,95E-03
2,3	8,03E-04	3,39E-04
6,0	1,11E-04	1,37E-05

3-Dimensional Structure ATENA 3D		
drift %	X dir.	Y dir.
0,5	5,46E-03	4,72E-03
0,9	2,95E-03	2,21E-03
2,3	3,39E-04	3,48E-04
6,0	1,37E-05	1,42E-05

3-Dimensional Structure Y dir.		
drift %	OpenSees	ATENA 3D
0,5	1,51E-02	4,72E-03
0,9	5,01E-03	2,21E-03
2,3	8,51E-04	3,48E-04
6,0	1,07E-04	1,42E-05

X, Y directions refer to x direction for the X+0.3Y loading and y direction for the 0.3X+Y loading respectively.

7. Conclusions

Fragility curves are sensitive to several parameters concerning their shape. These parameters can be the damage models and their thresholds are considered (both as random and multidimensional), the analysis methods, FE simulation, input ground motion, structural modelling and the structural parameters (damping ratio, stiffness etc.), (Cimellaro et al., 2006). These parameters have been seen to cause significant discrepancies in the derivation of empirical fragility curves by different authorities for the same location, even in cases where the same structure and seismicity are considered, (Priestley, 1998).

The development of the fragility curves for a class of buildings or for an individual building is always related to the choice of the structural model, and the structural parameters involved in the modelling of the structure which are inherently uncertain. The uncertainty is both in the mechanical properties, such as yield strength and stiffness, and geometric properties, such the modelling of the beam-column connections, FE simulation and others. Damage models influence the form of a fragility curve, according to the structural model and the seismic response system. The structural model is related to the height of a building that can change considerably the shape of a fragility curve. The difference in curve shape for building to building can be explained by the fact that structures of different heights tend to be built according to different building regulations and hence exhibit markedly different seismic resistance. The different building regulations established by the seismic codes become an additional influential factor affecting the shape of the fragility curves. In buildings which are designed according to the pre-seismic codes (HAZUS, 2003), the shape of the fragility curves is affected by the absence of capacity design in structures, which results in their failure via predominantly soft story modes under earthquake excitation. Failures of this type are associated with a rapid transition between low-levels of damage and the collapse limit state that is reflected in the vulnerability plot by a closer proximity of the curves.

The fragility curves are also affected by the lognormal standard deviation value (β) referring to its slope. The smaller the value of β is, the less variable the damage state, and the steeper the fragility curve. The larger the value of beta (β) is, the more variable the damage state, and the better the fragility curve. Beta values usually ranging from 0.4 to 1.2 (Rossetto & Elnasai, 2003).

FE simulation is possible to cause diversion in the shape of fragility analysis due to variable acceptances of softwares concerning total base force, mass calculation, results recording methods, beam-column connections.